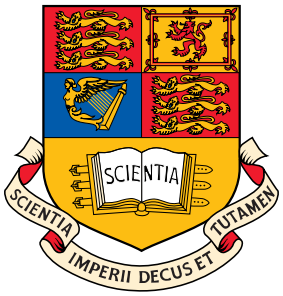
A Computational Study of Blood Flow and Vascular Nitric Oxide Transport

by

Ana M. Plata García



Department of Aeronautics

Imperial College of Science, Technology and Medicine

Prince Consort Road

London SW7 2BY

This thesis is submitted for the degree of Doctor of Philosophy of Imperial College London

2010

Declaration

I hereby declare that this submission is my own work and that it contains no material previously published or written by another person, nor material which to a substantial extent has been accepted for the award of any other degree or diploma of the university or other institute of higher learning, except where due acknowledgment has been made in the text.

Ana M. Plata García

Abstract

Atherosclerosis occurs in a spatially heterogeneous fashion within the arterial system. The patchy nature of the disease is thought to reflect spatial variation in haemodynamic factors such as wall shear stress (WSS) and in the concentration of vascular species. This thesis numerically investigates blood flow and vascular transport of the atheroprotective agent nitric oxide (NO) using a spectral/hp element method.

Firstly, NO distribution is analysed within a parallel-plate flow chamber coated with endothelial cells. Contrary to the accepted hypothesis that NO concentration increases with WSS (as does NO production), it is observed that NO concentration depends on WSS in a non-monotonic fashion. Furthermore, these results emphasise the effect of convection on *in vitro* NO transport, which has been overlooked or misinterpreted in most previous computational studies.

Secondly, blood flow and NO transport are investigated within a detailed representation of the rabbit thoracic aorta and its branches, which was reconstructed using high resolution computed tomography (CT) scan data of a vascular corrosion cast. The computed WSS distribution exhibits significant spatial heterogeneity, reflecting the complexity of the blood flow. In particular it is observed that two Dean-type vortices (associated with a skewed velocity profile) form in the aortic arch and propagate along the descending aorta. This results in streaks of WSS similar in nature to the fatty streaks of early stage atherosclerosis observed in mature rabbits. This finding provides further support for the hypothesis that blood flow mediates atherogenesis.

The vascular distribution of NO is found to depend significantly on the relationship between NO production and WSS. Furthermore, it is concluded that mechanisms preventing NO consumption by haemoglobin (such as diffusional barriers) must exist in order for NO to exert its atheroprotective action. This study represents the first effort to model NO transport in a realistic representation of the major arteries.

Acknowledgements

First and foremost, I would like to thank Prof. Spencer Sherwin and Prof. Rob Krams for their excellent supervision and constant support. I also would like to thank Prof. Peter Weinberg, Prof. Kim Parker, Dr. Joaquim Peiró, Dr. Paul Evans, Dr. Jordi Alastruey, Dr. Joerg Stiller, Dr. Leopold Gringberg and Mr. Anthony Hunt for insightful discussions and guidance.

I would especially like to thank Prof. Antonio Huerta for hosting my visit to the Departments of Applied Maths at the Polytechnical University of Barcelona. Thanks to the HPC-Europa Transnational Access Programme for making this visit possible.

I also would like to express my sincere gratitude to Dr. Alberto Figueroa for giving me the opportunity of visiting the Cardiovascular Biomechanics Research Laboratory at Stanford University and for his warm hospitality.

I am very grateful to the Imperial College High Performance Computing Department and the Barcelona Supercomputing Center for their computational resources and technical assistance. Thanks also to Dr. Stig Walsh and Dr. Richie Abel (Natural History Museum) for imaging assistance.

I would like to acknowledge the generous financial support from Fundación Caja Madrid, Imperial College London and the British Heart Foundation, which made this research possible. Thanks also to the Royal Academy of Engineering, the Institution of Mechanical Engineers, the Imperial College Trust and the Old Centralians Trust for awarding me various travel grants.

I would like to thank my colleagues in the Department of Aeronautics and Bioengineering for their friendship and support. Special thanks to my officemates in E357 Cristian, Erkan and Pedro for all the encouragement (and patience). A heartfelt thanks to Donal Taylor for making me feel home in rainy London.

I am most grateful to my friends. Special thanks to Sira and Lorena for all the fun and to Sofia for being there when it matters. I can't express with words how grateful I am to Pete for his love and limitless technical and personal support.

Finally, I owe my deepest gratitude to my family for their boundless love and support. I would especially like to thank my father (mi papi) for his unwavering interest, encouragement and enthusiasm.

Contents

Declaration **i**

Abstract **ii**

Acknowledgements **iv**

Table of Contents **vi**

List of Figures **xiv**

List of Tables **xviii**

Nomenclature **xix**

1 Introduction **1**

1.1 Atherosclerosis 2

1.1.1 Atherogenesis 3

1.1.2 Mechanisms of atherogenesis 4

1.2 Blood flow and atherosclerosis 5

1.2.0.1 Mechanical forces 6

1.2.0.2 Mass transport 7

1.3 Nitric oxide and atherosclerosis 8

1.3.1 Vascular biology of nitric oxide 8

1.3.1.1 From nitric oxide synthesis to vasodilation 8

1.3.1.2 Vascular effects of nitric oxide 11

1.3.1.3 Dual role of nitric oxide in the development of atherosclerosis plaques 11

1.4 Modelling mass transport within flow chambers 12

1.5 Modelling blood flow and mass transport within the arterial system . 13

1.5.1 Blood flow modelling 13

1.5.2 Mass transport modelling 16

1.5.2.1 Previous computational studies modelling vascular NO transport 16

1.6 Numerical methods 17

1.7 Objectives of the thesis 17

1.8 Structure of the thesis 18

2 Numerical Methods **20**

2.1 The spectral/hp element method 20

2.1.1 Basic concepts 22

2.1.1.1 Strong and weak formulations of a differential equation 22

2.1.1.2 Legendre inner product 23

2.1.1.3 Method of the weighted residuals 23

2.1.2 The Galerkin approximation 24

2.1.2.1 Example problem 24

2.1.2.2 Weak form: implementation of boundary conditions . 24

2.1.3 A spectral/hp element implementation of the Galerkin approximation 27

2.1.3.1 Elemental decomposition: the h-type extension . . . 27

2.1.3.2 Spectral expansion: the p-type extension 28

2.1.3.3 Matrix formulation 32

2.1.3.4 Local expansion bases 33

2.1.3.5 Extension to multiple dimensions 34

2.1.4 Navier-Stokes equations 39

2.1.5 Advection-Diffusion-Reaction equation 41

2.1.5.1 First-order reaction (*in vivo* nitric oxide transport) . 41

2.1.5.2 Second-order reaction (*in vitro* nitric oxide transport) 42

2.2 High-order mesh generation 43

2.2.1 High-order meshes in spectral/hp element methods 44

2.2.1.1 Elemental mappings for straight-sided elements . . . 44

2.2.1.2 Elemental mappings for curvilinear elements 45

2.2.2 High-order mesh generation using SPHERIGON patches . . . 47

2.2.2.1 The SPHERIGON patch 47

2.2.2.2 Vertex normal approximation 49

2.3 Summary 53

3 Nitric Oxide Transport in Flow Chambers 54

3.1 Introduction 54

3.1.1 Limitations of the model 56

3.2 Computational model for nitric oxide production and transport in flow chambers 57

3.2.1 Computational domain 58

3.2.2 Governing equation 58

3.2.3 Nitric oxide reaction with the culture medium 58

3.2.4 Nitric oxide production at endothelial cells 60

3.2.5 Boundary conditions 62

3.2.6 Velocity field 64

3.2.7 Parameters 64

3.2.8 Numerical method 65

3.3 Results 65

3.3.1 Nitric oxide production rate 65

3.3.2 Nitric oxide concentration field 66

3.3.3 Negative feedback mechanism 71

3.3.4 Dimensional results 72

3.4 Discussion 74

3.4.1 Nitric oxide concentration boundary layer 75

3.4.2 Nitric oxide concentration at the endothelium 76

3.4.3 Effect of convection on NO concentration 77

3.4.4 Negative feedback mechanism 78

3.4.5 Experimental studies 78

3.5 Summary 79

4 Blood Flow in the Rabbit Aorta **80**

4.1 Introduction 80

4.1.1 Limitations of the model 81

4.2 Methods 82

4.2.1 Reconstruction of the vascular geometry 82

4.2.1.1 Obtaining the vascular corrosion cast 82

4.2.1.2 Scanning the vascular corrosion cast 84

4.2.1.3 Obtaining a surface definition 84

4.2.2 Obtaining a volume mesh 86

4.2.3 Blood flow model 88

4.2.3.1 Governing equation 88

4.2.3.2 Boundary conditions 89

4.2.3.3 Parameters 90

4.2.4 Numerical method 91

4.3 Results 92

4.3.1 Blood flow in the aortic arch 93

4.3.2 Blood flow in proximal descending thoracic aorta 98

4.3.3 Blood flow in the vicinity of the intercostal arteries 105

4.4 Summary 107

5 Nitric Oxide Transport in the Rabbit Aorta 110

5.1 Introduction 110

5.2 Methods 112

5.2.1 Obtaining the computational geometry 112

5.2.2 Generating a computational mesh 112

5.2.3 Computational model of nitric oxide production and transport within the vasculature 113

5.2.3.1 Overview 113

5.2.3.2 Simplified model 114

5.2.3.3 Governing equation 116

5.2.3.4 NO reaction within the vessel lumen 116

5.2.3.5 Endothelial nitric oxide production 118

5.2.3.6 Boundary conditions 119

5.2.3.7 Parameters 120

5.2.4 Numerical methods 121

5.2.5 Suitability of the computational boundary layer mesh 121

5.3 Results 122

5.3.1 Effect of the endothelial response to WSS on vascular NO distribution 122

5.3.1.1 Effect of WSS-dependent *vs.* constant endothelial NO production rate on NO distribution 124

5.3.1.2 Effect of the specific form of the endothelial response to WSS 129

5.3.1.3 Influence of the basal NO production (γ) 131

5.3.1.4 Influence of NO reaction within the lumen (k_{Hb} and k_{pl}) and the thickness of the RBC-free layer δ 132

5.3.2 Effect of NO reaction within the vessel lumen 132

5.3.2.1 Effect of NO reaction with haemoglobin on vascular NO concentration when a RBC-free layer is not modelled ($\delta = 0$) 132

5.3.2.2 Effect of NO reaction with haemoglobin on vascular NO concentration when a RBC-free layer is modelled ($\delta \neq 0$) 134

5.4 Discussion 136

5.4.1 Effect of blood flow on vascular NO concentration 136

5.4.2 NO reaction within the lumen of the vessel 138

5.5 Summary 139

6 Conclusions and Future Work **141**

6.1 Summary of key results 141

6.2 Future work 143

6.2.1 Modelling nitric oxide transport within flow chambers 143

6.2.2 Modelling blood flow within the arterial system 144

6.2.3 Modelling nitric oxide transport within the arterial system . . 145

Bibliography **146**

A Vascular Nitric Oxide Synthesis **163**

A.1 Overview 163

A.2 Kinetic model of endothelial NO synthesis 164

A.2.1 Conclusions of the model 167

A.2.2 Transient NO production 168

A.2.3 Dependence on eNOS 168

A.2.4 Dependence on L-arginine 168

A.2.5 Dependence on oxygen 169

A.3 Simplified model of endothelial NO synthesis 169

B Convective Transport of Vascular Nitric Oxide **171**

B.1 NO convective transport 171

B.1.1 Overview 171

B.1.2 NO convective field 172

B.2 Vascular NO transport 174

B.3 Effect of convective transport on vascular NO concentration 175

B.3.1 NO convective transport when a constant NO production rate is considered 178

List of Figures

1.1 Outline of the signal transduction system of NO within the vascular system 10

2.1 Implementation of the spectral/hp element method 31

2.2 Standard regions $\mathcal{Q}_{st}$ for quadrangular-faced elements 35

2.3 Standard regions $\mathcal{T}_{st}$ for triangular-faced elements 36

2.4 4^{th}-order bidimensional basis $\phi_{pq}(\xi_1, \xi_2)$ defined in the standard element $\mathcal{T}_{st}^{2D}$. 38

2.5 Invalid elements in a curvilinear computational mesh 44

2.6 Construction of a mapping $\chi(\xi_1, \xi_2)$ between a curved quadrangular element and the standard space 47

2.7 The construction process of the SPHERIGON patch 48

2.8 Detail of the construction process of the SPHERIGON patch 49

2.9 Computational meshes of the third pair of intercostal arteries in the rabbit aorta 50

2.10 Vertex normals approximation in straight-sided meshes 51

2.11 Curvilinear approximation of the third pair of intercostal arteries of the rabbit aorta when the vertex normals are approximated from a coarse (a) and a fine (b) straight-sided mesh 52

3.1 Diagram illustrating nitric oxide production and transport within a flow chamber 58

3.2 Plots of R^*_{NO} against Pe for several values of the parameter W^*_{o} with fixed $\gamma = 10$ and $\beta^* = 0$ 66

3.3 Plots of C^* distribution within the flow chamber for a given value of the parameter space 67

3.4 Plot of C^*_L and R^*_{NO} against Pe for given endothelial response 68

3.5 Plots of C^*_L against Pe for different values of W^*_{o} with fixed $\gamma = 10$ and $\beta^* = 0$. 70

3.6 Plot of $C^*(x^*, 0)$ for cases where $\beta^* = 0$ and $\beta^* = 1$ 71

3.7 Plots of C^*_L against Pe for different values of W^*_{o} with fixed with fixed $\gamma = 10$ and $\beta^* = 1$. 72

3.8 Plots of C_L against WSS for different values of W^*_{o} with fixed with fixed $\gamma = 10$ and $\beta^* = 0$. 73

4.1 Images showing the vascular corrosion cast 83

4.2 Images showing the final surface definition 85

4.3 Images showing the computational mesh 87

4.4 Blood flow streamlines and vortical structures in the aortic arch . . . 94

4.5 Blood flow streamlines viewed posterior-anterior 95

4.6 Colour maps of WSS at the aortic arch viewed ventral-dorsal 97

4.7 Colour maps of WSS at the aortic arch viewed posterior-anterior . . . 98

4.8 Colour maps of the blood vorticity at the descending aorta viewed ventral-dorsal 99

4.9 Colour maps of the blood flow velocity at the descending aorta viewed ventral-dorsal 100

4.10 Streamlines of blood flow in the descending aorta viewed posterior-anterior 100

4.11 Colour maps of WSS at the descending aorta viewed dorsal-ventral . 102

4.12 Colour maps of WSS in the descending aorta viewed *en face* 103

4.13 *En face* disease maps in the descending aorta of mature cholesterol-fed rabbits 105

4.14 Colour maps of WSS at the vicinity of the intercostal branches 107

5.1 Images of the high-order curved boundary layer mesh 113

5.2 Diagram illustrating how vascular NO transport is modelled within the rabbit aorta 119

5.3 Colour maps of NO distribution viewed at a cross-section within the descending thoracic aorta 122

5.4 Plots of R^*_{NO} against WSS for several values of the parameter W_{o} . . 123

5.5 Colour maps of WSS and NO concentration in the aortic arch viewed ventral-dorsal 126

5.6 Colour maps of WSS at the descending aorta viewed dorsal-ventral . 127

5.7 Colour maps of WSS and NO concentration in the vicinity of the intercostal branches 128

5.8 Colour maps of WSS and NO concentration in the aortic arch viewed ventral-dorsal 130

5.9 Colour maps of WSS and NO concentration in the vicinity of the third pair of intercostal arteries viewed dorsal-ventral 131

5.10 Plots of the average endothelial NO concentration $\bar{C}_{NO_{ec}}$ against NO reaction rate with haemoglobin k_{Hb} with fixed $\delta = 0$ 133

5.11 Plots of NO concentration at an arbitrary point within the thoracic descending aorta against the coordinate in the direction normal to the arterial wall η 134

5.12 Plots of the average endothelial NO concentration $\bar{C}_{NO_{ec}}$ against NO reaction rate with haemoglobin k_{Hb} for different values of δ with fixed $k_{pl} = 0$. 135

5.13 Plots of NO concentration at an arbitrary point within the thoracic descending aorta against the coordinate in the direction normal to the arterial wall η 136

B.1 Diagram illustrating how the NO convective field is modelled within the NO concentration boundary layer 173

B.2 Colour maps of shear rates in the aortic arch and the third pair of intercostal arteries 177

List of Tables

3.1 Description of the constant parameters of the model of nitric oxide production and transport in flow chambers. 59

3.2 Description of the non-dimensional parameter ranges for the simulation of nitric oxide transport in flow chambers. 64

4.1 Description of the constant parameters used in the blood flow simulations within the rabbit aorta 91

4.2 Description of the inflow aortic velocities used in the blood flow simulations within the rabbit aorta 91

5.1 Description of the parameters ranges used for the simulation of vascular NO production and transport within the rabbit aorta 120

A.1 Kinetic constants that regulate endothelial nitric oxide synthesis . . 167

A.2 Michealis constants K_m involved in endothelial nitric oxide synthesis 170

Nomenclature

List of Acronyms

WHO	World Health Organisation
NO	Nitric Oxide
WSS	Wall Shear Stress
LDL	Low Density Lipoproteins
HDL	High Density Lipoproteins
RBC	Red Blood Cell
Hb	Haemoglobin
SMC	Smooth Muscle Cell
ATP	Adonesine Triphosphate
ADP	Adonesine Diphosphate
EDRF	Endothelium Derived Relaxing Factor
iNOS	Inducible Nitric Oxide Synthase
cNOS	Constitutive Nitric Oxide Synthase
eNOS	Endothelial Nitric Oxide Synthase
nNOS	Neuronal Nitric Oxide Synthase
CT	Computed Tomography
MR	Magnetic Resonance
CBL	Concentration Boundary Layer

List of symbols

x, y, z	Cartersian Coordinates
u, v, w	Cartersian velocity components
$\mathbf{v}$	Velocity vector
p	Pressure
t	Time
h	Height flow chamber
L	Length flow chamber
b	Width flow chamber
μ_w	Dynamic viscosity of water
d	Entrance length flow chamber
C_{NO}	Nitric oxide concentration
D_{NO}	Nitric oxide diffusion coefficient
V_{NO}	Nitric oxide consumption rate
k_{Hb}	Nitric oxide reaction rate with haemoglobin
k_{pl}	Nitric oxide reaction rate within the plasma layer
k_{O_2}	Nitric oxide reaction rate with oxygen
k	Pseudo-second nitric oxide reaction rate with the culture media
R_{NO}	Nitric oxide production rate
$R_{\mathrm{NO}_{\mathrm{MAX}}}$	Maximum nitric oxide production rate
γ, W_{o}, β	Parameters characterising the endothelial response to wall shear stress.
V_{o}	Average flow velocity within the flow chamber.
C_L	Endothelial nitric oxide concentration at the exit of the flow chamber.
μ	Dynamic viscosity of blood
ρ	Density of blood
U_0	Average inflow velocity at the aortic root
D_0	Hydraulic diameter of the aortic root inflow plane
δ	Thickness of the RBC-free layer
η	Coordinate in the direction normal to the arterial wall
$\bar{C}_{NO_{ec}}$	Average wall nitric oxide concentration within the rabbit aorta

List of Dimensionless Numbers

Pe	Peclet Number
Re	Reynolds Number
De	Dean Number
Da	Damköhler Number

Chapter 1

Introduction

Atherosclerosis is an extremely common form of cardiovascular disease characterised by the formation of lipid rich plaques within the arterial wall. Such plaques can lead to the stenosis of large arteries and eventually rupture causing a heart attack or stroke. According to the World Health Organisation (WHO) atherosclerosis is currently the leading cause of death globally, accounting for approximately 40% of deaths in developed countries [1]. Furthermore, atherosclerotic-induced diseases impose an increasingly significant economic burden on governmental health systems [102].

During the past 40 years extensive research has been conducted to elucidate the mechanisms underlying atherosclerosis. Such research work ranges from experimental *in vivo*, *ex vivo* and *in vitro* studies, to mathematical and computational models. While experimental investigation is essential to understand the biological processes that regulate atherosclerosis, computational models have also proved to be an invaluable research tool. The main advantages of computational models are their capacity to predict unmeasurable quantities, and their ability to investigate the behaviour of the system modelled over a range of parameters at a relatively low cost.

Also, computational models provide a theoretical framework that aids planning and

interpretation of experimental studies. On the other hand, the level of biological detail described by a computational model is limited, given the great complexity of the system studied. However, such simplified formulations are particularly valuable for gaining understanding of the process modelled.

This thesis presents a computational study of blood flow and nitric oxide (NO) transport. NO transport is investigated in both *in vitro* and *in vivo* scenarios. First, NO distribution is analysed within a parallel-plate flow chamber. The relationship between NO concentration and wall shear stress (WSS) is investigated in detail. This study provides a theoretical framework to aid accurate interpretation of related experimental studies. Second, NO transport and blood flow are investigated in a realistic representation of the rabbit thoracic aorta. Different flow metrics, such as WSS, and NO distribution are analysed, along with their possible relevance to the onset of atherosclerosis.

This chapter offers a brief overview of atherosclerosis and the mechanisms that act to regulate it. Particular attention is paid to the potential effect of haemodynamic forces and NO transport on the onset of the disease. Furthermore, previous computational studies investigating blood flow and mass transfer within the arterial system are reviewed. Finally the main objectives of the thesis are stated, and an overview of the thesis structure is given.

1.1 Atherosclerosis

Atherosclerosis is an inflammatory disease that affects large vessels within the vasculature. This disease is characterised by the accumulation of lipoproteins, calcium and other substances within the arterial wall. The growth of these plaques may eventually lead to a significant narrowing of the vessel lumen (stenosis), and therefore a reduction in blood flow and hence oxygen supply (ischemia). The consequences may be even more severe if the plaques become unstable and rupture. If this is the case, a sudden release of thrombogenic material into the lumen occurs, and a

blood clot is formed. This clot may act to partially or totally occlude the artery, dramatically reducing blood flow and leading to the death of the tissues fed by the artery (infarction) [113, 80, 137].

Atherosclerosis is a slowly progressing disease. It can begin in childhood and progress over decades. However, it only becomes symptomatic in advanced stages, once atherosclerotic lesions are fully developed [3, 118]. Understanding the mechanisms that regulate atherosclerosis may elucidate improved diagnosis and treatment techniques and therefore alleviate the health and economic burden of atherosclerosis in our society.

1.1.1 Atherogenesis

Atherogenesis is the initiation process of atherosclerosis. It is by this process that advanced plaques –called atheromas– develop within the intima of the arterial wall.

Early atherosclerotic lesions are characterised by the accumulation of oxidised cholesterol and monocyte-derived macrophages in the intima. The mechanisms that lead to the formation of these subendothelial deposits remain a point of contention. However, it is widely accepted that the cholesterol carried through the bloodstream by low density lipoproteins (LDL) traverse the endothelium and become oxidised [125, 101]. At this point, this process can be reversed by the action of high density lipoproteins (HDL), which can remove accumulated cholesterol from tissue [6, 12].

LDL uptake and oxidation result in an inflammatory response [100]. Circulating monocytes are recruited from the bloodstream and move to the location of the accumulated LDL. There, monocytes differentiate into macrophages, which ingest oxidised LDL and generate large foam cells with a high lipid content [14, 124].

In more advanced stages, other chemical substances (cytokines) secreted by the damaged endothelium promote the proliferation of Smooth Muscle Cells (SMC) and their migration from the tunica media to the intima of the arterial wall [111]. This

mechanism is postulated to cause the formation of a fibrous capsule covering the subendothelial fatty deposits [79]. The encapsulated deposits, now called atheromas, activate an enzymatic mechanism that causes the vessel to enlarge over time [79]. Stenosis of the vessel occurs when this enlargement is not sufficient to compensate for the extra thickness of the arterial wall produced by the atheroma.

1.1.2 Mechanisms of atherogenesis

Historic perspective

Since Jean Lobstein introduced the term *atherosclerosis* in 1829 [85], many hypotheses have been proposed to explain the initiation of the disease. Links between inflammation and atherosclerosis were suggested by Rokitansky as early as 1855 [117], although this finding was described in terms of the prevailing humoral theory. In 1871, Virchow introduced the concept of cellular pathology, and suggested that inflammatory changes at a cellular level played a major role in the development of atherosclerotic plaques [146]. Virchow strongly criticised the outdated humoral conceptions and laid the foundations of cellular research [1].

Research at the beginning of the 20th century focused on the study of pathological factors rather than inflammatory-inmmunologic processes. In 1913, Anitschkow demonstrated that rabbits fed with a cholesterol-rich diet spontaneously developed atherosclerotic lesions [5]. Later in the century, other factors such as smoking, obesity, high blood pressure and "*high emotional stress*" [66] were found to be associated with an increase risk of disease development.

In 1973, Ross and Glomset formulated the famous *"response to injury"* hypothesis [120], by which inflammation and subsequent plaque formation were a response to a locally "injured" or damaged endothelium. This theory was shortly discarded after

[1] Virchow first suggested the active role of the endothelium: "It is not enough that, as has for a long time been the case, the muscles should be singled out as being the only active elements; within the great remainder, which is generally regarded as an inert mass, there is in addition an enormous number of active parts to be met with".

in vivo studies showed that endothelial cells at disease sites are morphologically normal [159].

Current consensus

In the late 90s the idea of a damaged endothelium was replaced by the concept of "*endothelial dysfunction*" [16, 33, 131]. This theory –still widely accepted– proposes that atherosclerosis lesions develop as a result of an impairment of endothelial functions (specially vascular tone regulation).

However, the cause of endothelial dysfunction remains unclear. The current understanding identifies haemodynamic factors as determinants of vascular endothelial health [63, 89]. Atherosclerosis is known to occur in a spatially non-uniform fashion within the arterial system, with plaques preferentially developing in areas of high curvature and arterial branching [19]. Since blood flow is intrinsically non-uniform due to the complex geometry of the vasculature, it has been postulated that atherogenesis may be driven by flow-dependent mechanisms. In particular, the patchy nature of the disease is thought to reflect spatial variation in the stresses exerted on the arterial wall by the flow of blood [126].

The relationship between atherosclerosis and blood flow is analysed in detail in the following section. However, before describing the flow-dependent mechanisms that may regulate atherogenesis, it is important to highlight that haemodynamic factors do not induce development of the disease, but provide predisposition for endothelial dysfunction.

1.2 Blood flow and atherosclerosis

A relationship between atherosclerosis and the surrounding haemodynamic environment was firstly proposed by Rindfleish in 1872 [116]. In this study Rindfleish suggested that atherosclerotic lesions "*are found particulary at such places at which the current of blood breaks with the greatest force*".

Over the next century, several mechanisms explaining correlations between blood flow and disease patterns were proposed based on Rindfleish's observations [122]. Most of these mechanisms considered that the mechanical forces exerted by the blood flow acted to physically damage the endothelium, and hence enhanced wall lipid deposition [47]. These models became more elaborated in the 1960's, and eventually led to the consensus that vascular regions of high WSS were susceptible to suffer from the disease.

Two groundbreaking papers by Caro *et al.* in 1969 [19] and 1971 [20] called such a prevailing theory into question. These studies suggested that atherosclerotic lesions occur in areas of low WSS, and proposed a sophisticated mechanism by which LDL was transported into the wall in a shear-dependent fashion. Caro's work sparked intense debate in the research community that lasted nearly two decades. Nowadays cumulative experimental evidence supports Caro's hypothesis (although the specific proposed mechanism has been discarded), and the general consensus is that atherosclerotic plaques develop in vascular regions with low or oscillatory WSS.

Presently, the hypothesis that atherogenesis is exclusively driven by WSS is regarded as too simplistic, and a great number of flow-dependent mechanisms that may regulate the onset of the disease have been proposed. Such flow dependent mechanisms have been traditionally classified into two categories: (a) mechanism whereby the mechanical forces exerted by the blood flow directly affect the properties of the arterial wall, and (b) flow-dependent transport mechanisms of vascular species towards, from and into the arterial wall. However, such a classification criteria may be considered too rigid, as mechanisms from both categories often overlap. In the following section each group of mechanisms is briefly overviewed.

1.2.0.1 Mechanical forces

The endothelium is in direct contact with the flowing blood and thereby constantly exposed to the mechanical forces that blood flow exerts. Endothelial cells have been shown to sense and discriminate between such mechanical stimuli, and more

importantly, respond to them [45]. For instance, shear-exposed endothelial cells have been shown to elongate and align themselves with the direction of the flow [114]. Therefore, vascular cell morphology –in particular cell orientation– has been suggested to be a natural marker of blood flow features and can potentially help identify pathogenic blood flow profiles.

Numerous experimental studies suggest that not only the endothelial morphology, but its function strongly depends on the surrounding haemodynamic environment [119]. For example, the vascular wall physiology is postulated to depend on the WSS level the endothelium is exposed to. In particular, wall permeability is thought to be enhanced in areas of low WSS, leading to an increase in LDL uptake rate and hence the development of atherosclerotic plaques [57]. Endothelial function is also thought to be regulated by blood flow via more sophisticated mechanisms, such as shear-dependent gene-regulation [62] and biochemical changes driven by complex signalling pathways [60]. In this study the dependence of endothelial production of NO –a fundamental atheroprotective agent– on WSS will be investigated in detail. A review of other flow-dependent endothelial responses can be found in [18], [142] and [31].

1.2.0.2 Mass transport

Vascular species such as LDL, ATP (adenosine triphosphate), ADP (adenosine diphosphate), oxygen and NO have been postulated to play a key role in development of atherosclerotic lesions [128, 105, 99]. Blood flow regulates the convective transport of such species towards, from and into the wall. Therefore, under conditions of complex blood flow, production and transport of vascular species may be impaired, leading to abnormal species concentrations that may potentially promote atherogenesis.

Traditionally, studies have focused on investigating the effect of blood flow on the arterial wall physiology. However, over the last decade considerable attention has been directed towards the study of vascular species transport and its implications for

atherogenesis. This thesis investigates vascular NO transport in conjunction with blood flow, along with their possible relevance to the spatially heterogeneous onset of atherosclerosis.

1.3 Nitric oxide and atherosclerosis

In 1980 Furchgott and Zawadski reported the existence of a substance released by the endothelium that caused vasodilation in rabbits [49]. This undefined substance was initially called endothelium-derived relaxation factor (EDRF). The short half-life of EDRF hindered its full biochemical characterisation for almost one decade. In 1986 several research groups independently proposed that EDRF was NO or an NO-containing substance [59, 48]. Finally in 1987 Palmer *et al.* experimentally demonstrated that EDRF was indeed NO [103].

Since then, much research has been devoted to characterise the vascular biology of NO and to determine its effect on the vascular system. Strong evidence suggests that NO plays a key role in the pathogenesis of several diseases, including hypertension and atherosclerosis [75, 99]. In this section, the biochemistry and vascular biology of NO is reviewed, and in particular its role as an antiatherogenic molecule is analysed.

1.3.1 Vascular biology of nitric oxide

1.3.1.1 From nitric oxide synthesis to vasodilation

Nitric oxide synthesis

NO is produced in the human body by the oxidation of L-arginine to L-citrulline. The enzyme nitric oxide synthase (NOS) catalyses this reaction, which also requires the presence of tetrahydrobiopterin (BH_4) and reduced nicotinamide adenine dinucleotide phosphate (NADPH) [44]. (For a complete description of endothelial NO synthesis chemistry please refer to Appendix A).

The enzyme NOS can be classified based on its functional class, differentiating between constitutive and inducible NOS. Constitutive NOS can be isolated from neurones (nNOS) and endothelial cells (eNOS), and it is thought to be responsible for the continued and sustained production of NO within the human body. On the other hand, the action of inducible NOS (iNOS) is mainly triggered by bacterial endotoxins and cytokines during inflammation processes [37] .

Under physiological conditions, endothelial nitric oxide synthase (eNOS) is postulated to catalyse the intracellular reactions that lead to vasodilation [93]. Despite the constitutive nature of eNOS, it has been shown that its expression can be induced by a number of agonist and WSS-gated mechanisms. Such mechanisms can be classified as Ca^{2+} dependent and Ca^{2+} independent mechanisms.

Ca^{2+}-dependent eNOS regulation relies on numerous and complex signalling pathways. In simplified terms, eNOS resides within endothelial caveolae (invaginations of the plasma membrane) where the protein caveolin-1 inhibits its action. Increased cytosolic levels of Ca^{2+} activates a calmodulin-dependent pathway that leads to the disassociation of eNOS and caveolin-1, and therefore to eNOS activation. Intracellular Ca^{2+} levels may be raised through both WSS and agonist-gated pathways (Fig. 1.1). A detailed description of Ca^{2+} dependent eNOS upregulation can be found in [37].

Ca^{2+}-independent eNOS regulation is experimentally well established. However, the specific mechanisms that lead to eNOS activation remain uncharacterised. The current consensus is that WSS directly stimulates eNOS phosphorylation (and activation) at different locations by Akt-dependent and independent mechanisms [15] (Fig. 1.1). Recent studies also suggest that reversible WSS-gated S-Nitrosylation may also contribute to eNOS upregulation. A detailed review of eNOS phosphorylation and S-Nitrosylation processes is given in [37].

The relative contribution of Ca^{2+} dependent and independent mechanisms to eNOS regulation remains unclear. The current understanding suggests that WSS-dependent mechanisms are mostly responsible for eNOS activation under physiological condi-

tions. Since reduced bioavailability of NO is postulated to promote atherogenesis, this WSS-dependent upregulation of eNOS (and hence NO production) may provide a partial explanation for the flow-mediated onset of the disease.

Vasodilation

NO produced in the endothelium rapidly diffuses into both the lumen and the subjacent smooth muscle cells (SMC). In the lumen, NO avidly reacts with haemoglobin contained in red blood cells, while in the SMC NO induces the enzymatic action of soluble guanylate ciclase, which promotes the conversion of guanosine triphosphate (GTP) to cyclic guanosine monophosphate (cGMP). Increasing intracellular levels of cGMP induce the activation of cGMP-dependent protein kinases, which lead to SMC relaxation, and therefore vasodilation [22]. An outline of the signal transduction system of NO within the vascular system is shown in Figure 1.1.

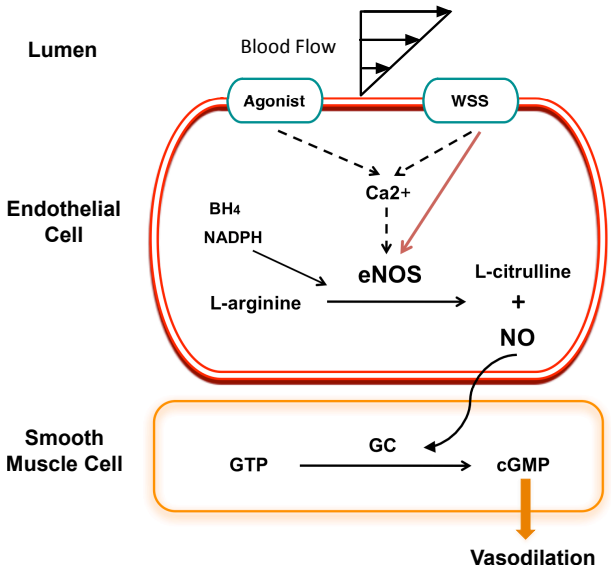


Figure 1.1: Outline of the signal transduction system of NO within the vascular system. NO is mostly produced by endothelial cells under physiological conditions. Such a production is regulated by number of mechanisms, as illustrated in this figure. NO produced at the endothelium subsequently diffuses into the arterial wall, where it actives a complex signally pathway that leads to vasodilation.

1.3.1.2 Vascular effects of nitric oxide

Vascular effects of NO include [92, 143]:

- Direct **vasodilation** (flow dependent and receptor mediated).
- Indirect **vasodilation** (by inhibiting vasoconstrictor influences).
- Inhibition of platelet adhesion to the vascular endothelium. **(Anti-thrombotic effect)**.
- Inhibition of leukocyte adhesion to vascular endothelium. **(Anti-inflammatory effect)**.
- Inhibition of smooth muscle hyperplasia. **(Antiproliferative effect)**.
- Inhibition of LDL oxidation. **(Antioxidant effect)**.

Reduced NO bioavailability due to impaired production and/or transport may therefore cause a number of pathological conditions, such as vasoconstriction, thrombosis, inflammation and vascular hypertrophy [143]. A careful review of NO vascular effects (and vascular disorders associated with a deficit of NO) is given by Cooke *et al.* [27].

1.3.1.3 Dual role of nitric oxide in the development of atherosclerosis plaques

Vascular NO is thought to play a dual role in the development of atherosclerosis. A number of experimental studies have corroborated the atheroprotective role of NO under physiological environments. For example, Cohen *et al.* reported that abnormal endothelial-mediated relaxation preceded lesion formation in atherosclerotic-free

pigs fed with a high-cholesterol diet [26]. Furthermore, the administration of antioxidants [69], L-arginine [36, 30] and other NO promoters [36], have been shown to enhance vascular relaxation and decelerate the progression of atheromas in humans (unfortunately, clinical trials on the oral use of L-arginine in atherosclerosis treatments in humans have yielded conflicting or inconclusive results).

Despite such atheroprotective action, NO has been postulated to contribute to the development of the lesions in later stages of the disease. In particular, it has been suggested that the inflammatory conditions associated with atherosclerosis may trigger the action of iNOS. In such pathological environments, the production of NO by iNOS may be 1000-fold greater than that generated by eNOS. Such excessive NO release may act to further contribute to endothelial dysfunction [35]. Note that in this study vascular NO production and transport are investigated under physiological conditions, before lesions have formed.

1.4 Modelling mass transport within flow chambers

In order to elucidate the mechanisms that mediate atherogenesis, numerous experimental studies have investigated the endothelial response to mechanical stimuli *in vitro*. In particular, the dependence of endothelial NO production on WSS has been extensively investigated using parallel-plate flow chambers [46, 65]. However, despite these efforts, the relationship between WSS and NO production remains uncharacterised, and estimations of NO production rates in the literature vary over several orders of magnitude [22].

Some authors [150] have suggested that discrepancies between experimental studies may be partially explained by an insufficient characterisation of the flow regimes within the flow chambers. Therefore, a careful review of fluid-dynamic aspects of the experiments may potentially reconcile previous apparently conflicting results.

This thesis investigates NO production and transport within a parallel-plate flow chamber coated with endothelial cells. A mathematical model for endothelial endothelial NO production is proposed in Chapter 3. Such a model is subsequently used to investigate NO distribution within the flow chamber. The relationship between endothelial NO concentration and WSS is investigated in detail. The results are discussed within the context of previous experimental and theoretical studies. The present study aims to develop an enhanced understanding of *in vitro* NO transport and hence to provide a theoretical framework for the accurate interpretation of experimental data. Further, the model of endothelial NO production developed in Chapter 3 is used to investigate vascular NO distribution in Chapter 5.

To the author's knowledge, only two previous computational studies [65, 40] have modelled NO dynamics in *in vitro* scenarios. Such previous studies, along with their limitations, are analysed in detail in Chapter 3.

1.5 Modelling blood flow and mass transport within the arterial system

This thesis presents a computational study of blood flow and NO transport in a realistic representation of the rabbit vasculature. This section overviews previous computational and mathematical studies investigating blood flow and mass transport within the arterial system, and discusses the contribution made by the work presented in this thesis.

1.5.1 Blood flow modelling

Since haemodynamic forces were postulated to regulate atherogenesis, a great number of computational and mathematical studies have attempted to correlate areas of disease prevalence in arteries with flow metrics such as WSS.

Early studies focused on the analysis of flow features in simplified arterial geometries. In 1986 Perktold *el at.* modelled blood flow in an idealised 2D carotid bifurcation, and identified stagnation points and flow reversal as potential atherogenic flow patterns [106]. Subsequent studies investigated WSS distribution in a range of idealised vascular regions, primarily bends [77], bifurcations [107] and stenoses [139].

Blood flow simulations in such simplified geometries have been proved to be a useful tool to gain understanding of blood flow physics. However vascular WSS distribution has been shown to depend strongly on subject-specific geometrical features [95, 64]. Therefore, generating a detailed and faithful computational definition of the vascular geometry is necessary in order to accurately model blood flow within the arterial system.

Only a few computational studies have investigated blood flow in physiologically significant representations of the arterial tree. The first haemodynamics analysis of a large vascular area was presented by Huo *et al.* [58]. This study investigated pulsatile blood flow within the entire length of the mouse aorta and its primary branches. The computational geometry was obtained from morphometric measurements of a vascular corrosion cast, leading to a computational domain lacking detail and accuracy. Flow metrics such as WSS, spatial gradients of WSS and oscillatory shear index were calculated, and a correlation between areas of low or "*complex*" WSS and regions of disease prevalence was suggested.

A more physiologically realistic (although shorter in extent) representation of the mouse aorta was given in [138] and [42], where the computational geometries were obtained from high resolution CT-scans of vascular corrosion casts. Both studies explored possible similarities between WSS distribution in humans and mice. Both research groups reported large differences in WSS magnitude between the two species, and suggested that endothelial cells may respond to changes in WSS rather than to WSS magnitude. However, these studies largely differed in terms of the computed WSS distribution. Suo *et al.* suggested that low WSS areas in mice correlate with human disease patterns, while Ethier *et al.* proposed that WSS dis-

tribution is spatially more uniform in mice than in men.

Recent work by Liu *et al.* [83] and Shahcheragui *et al.* [127] modelled blood flow in the human aorta and the aortic arch branches. In both studies the aortic centerline and cross-sectional areas were obtained from MR scan data of healthy volunteers. However, the aortic cross-sections were later simplified as circles. In [83] the effects of arterial branching, torsion and tapering on blood flow were analysed, highlighting the relevance of geometrical features on WSS distribution. In particular it was found that aortic torsion plays a key role in vascular haemodynamics and largely determines WSS distribution in the descending aorta. Results by Shahcheragui *et al.* are not in agreement with [83], and they suggested that early atherosclerotic lesions preferentially develop in areas of *"extrema (either maxima or minima) WSS and pressure"*.

The above discussion illustrates the conflicting nature of the results of previous computational studies, and raises the need for further computational work. Discrepancies between previous studies may be partly explained by numerical deficiencies, and the use of idealised arterial geometries and simplified boundary conditions. Further discussion on the subject is offered in Chapter 4.

To the author's knowledge, no previous studies have modelled blood flow in a realistic representation of the rabbit aorta. In this study the arterial geometry was obtained from high resolution CT scan data of a vascular corrosion cast of a male New Zealand White rabbit. The computational domain comprises the ascending aorta, aortic arch and proximal descending thoracic aorta. In terms of combined detail and extent, the computational geometry in this study represents a significant advance from previous studies. A complete description of the methodology for the computational reconstruction of the rabbit aorta is given in Chapter 4.

1.5.2 Mass transport modelling

In the last decade special attention has been paid to the transport of vascular species and its possible links with atherogenesis. Numerous computational studies have investigated mass transfer phenomena in physiological [64, 82] and in vitro scenarios [65, 40].

Early work focused on the analysis of oxygen and LDL transport within idealised geometries [39, 88, 112] (primarily bends and bifurcations, following contemporary blood flow studies). Generally, these studies reported abnormal transport patterns in areas of low WSS and flow recirculation.

In 2001 Ethier *et al.* modelled oxygen transport in a realistic representation of the right coronary artery [64]. This study concluded that the effect of local geometric features on mass transfer patterns was even greater than on WSS distribution. Despite this finding, only one research group has undertaken the analysis of vascular species transport in a physiologically relevant representation of the wide region of the arterial system. Liu *et al.* analysed LDL and oxygen transport in a realistic representation of the human aorta and its branches (although the aortic cross-sections were simplified as circles) [82]. It was found that aortic torsion facilitates oxygen delivery to the arterial wall. Such a result further emphasises the sensitivity of mass transfer to geometric variations and therefore the need to generate accurate computational geometries.

1.5.2.1 Previous computational studies modelling vascular NO transport

While a wide body of research has been directed towards the experimental characterisation of NO role in atherogenesis, computational studies addressing NO biotransport are rather limited.

Due to its high diffusivity and its short half-life, computational modelling of vascular

NO transport is a challenging task. Most existing computational studies are limited to the analysis of NO distribution within 2D geometries, primarily straight vessels in the microvasculature [17, 96, 144] . A complete review of such studies is offered in Chapter 5.

To the author's knowledge, no previous studies have investigated NO transport in an either a realistic or idealised 3D representation of the vasculature. Here a computational study of NO production and transport within the rabbit aorta is presented. Endothelial NO distribution is analysed along with its possible relevance to the onset of atherosclerosis. Although the model presents several limitations (as discussed in Chapter 5), it aims to provide insight into vascular NO transport and motivation for further computation work.

1.6 Numerical methods

Most previous computational have used finite element or finite volume methods to solve the equations that govern blood flow and vascular mass transfer. Here a spectral/hp element method approach is adopted instead.

Spectral/hp methods exhibit geometric flexibility and excellent convergence properties. Chapter 2 overviews the basic principles of the numerical method employed, along with numerical issues regarding the generation of high-order computational meshes. Further, a previously existing mesh generation algorithm [54, 147] is described, and a new technique to improve such an algorithm is proposed.

1.7 Objectives of the thesis

This thesis investigates blood flow and NO transport numerically using a spectral/hp element method.

First, NO production and transport is investigated within a parallel-plate flow chamber. The objective of this study is to develop a more detailed understanding of NO distribution within flow chambers. In particular, it aims to identify key parameters that regulate NO production and transport under *in vitro* conditions in order to aid accurate interpretation of experimental data.

Second, blood flow and NO transport are modelled within a realistic representation of the rabbit aorta and its branches. This research aims to contribute towards an enhanced understanding of blood flow dynamics and vascular NO transport, and their relationship with atherosclerosis. Specifically, this study aims to establish correlations between blood flow, NO and disease patterns, and therefore contribute to the elucidation of the flow-dependent mechanisms that mediate atherogenesis.

Finally, this study aims to show the possibility of using spectral/hp element methods to solve fluid dynamics problems in the field of bioengineering, where finite element and volume methods have traditionally been used.

1.8 Structure of the thesis

The thesis is structured as follows:

Chapter 2 overviews the numerical methods used in this study. Firstly the basic principles of the spectral/hp element method are described and fundamental concepts in high-order mesh generation are reviewed. Finally, an algorithm to generate curvilinear meshes is proposed.

Chapter 3 introduces a model for endothelial NO production, and discusses NO distribution in *in vitro* experiments using parallel-plate flow chambers.

Chapter 4 and 5 analyse blood flow and NO transport respectively within the rabbit aorta, along with their potential relevance to atherogenesis. Further, Chapter 4 details the methodology for the computational reconstruction of the rabbit aorta

and its branches.

Finally the conclusions of this thesis are presented in Chapter 6, together with suggestions for further work.

Chapter 2

Numerical Methods

This chapter describes the numerical methods used to perform the blood flow and mass transfer simulations presented in this thesis. The chapter is organised in two sections. The first section formulates the basic principles of the spectral/hp element method used in this study, and applies such a formulation to the Navier-Stokes and to the Advection-Diffusion-Reaction equation. The second section reviews fundamental concepts in high-order mesh generation, and proposes an algorithm to curve straight-sided meshes using so called SPHERIGON [147] patches.

2.1 The spectral/hp element method

Numerical methods are widely used to find approximate solutions to differential equations that do not admit analytic solutions. Traditionally, numerical methods have been classified into four major groups [43]: finite difference methods, finite volume methods, finite element methods and spectral methods. Spectral/hp element methods lie somewhere between the latter two, since they can be thought of either as *a multi-domain spectral method*, or as *a high-order finite element method* [129].

Finite element methods subdivide the computational domain into smaller separate

regions called *elements*. This process is often referred to as spatial or *h-type discretisation*, where h represent the characteristic size of the elements. The approximate solution is then represented as a low-order polynomial expansion (often a linear expansion) within each element. Algebraic convergence is achieved by reducing the size of the elements (*h-type refinement*). Finite element methods exhibit great geometrical flexibility, as the size of the elements can vary within the computational domain. For instance, smaller elements can be position in areas where the solution is expected to develop complex features such as steep gradients.

In spectral methods, the solution is approximated by a global p-order expansion within the whole computational domain (spectral or *p-type discretisation*). Exponential convergence is achieved by increasing the number of modes in the expansion (*p-type refinement*). Spectral methods exhibit superior convergence properties and higher accuracy than traditional finite element methods. However, constructing a continuous global expansion across the computational domain is not always possible, and hence spectral methods are often limited to geometrically simple domains.

Spectral/hp element methods aim to combine the geometrical flexibility of finite element methods with the superior accuracy and convergence properties of spectral approaches. The computational domain is discretised in space and the solution is then approximated by a high-order expansion within each element (*hp-type discretisation*). Therefore, converge can be achieved through either h or p-type refinements, or both.

An in-house implementation of the spectral/hp element method (the code $N\epsilon\kappa\tau\alpha r$ [129]) was used to perform the blood flow and mass transfer simulations presented in subsequent chapters. This section reviews elementary numerical concepts and describes a basic formulation of the spectral/hp element method. Further, the implementation of such method to solve the Navier-Stokes and the Advection-Diffusion-Reaction equations is discussed. Finally, the time-discretisation schemes used to solve the aforementioned equations are presented.

2.1.1 Basic concepts

2.1.1.1 Strong and weak formulations of a differential equation

Example problem

Consider the differential problem given by the one dimensional Poisson equation:

$$\frac{d^2u}{dx^2} + f = 0, \tag{2.1}$$

where the solution $u(x)$ is continuously differentiable, and $f = f(x)$ is an arbitrary forcing function.

Strong formulation

Consider the solution $u(x)$ in the domain $\Omega = \{x \,|\, x_0 \leq x \leq x_N\}$. Further, consider the following boundary conditions:

$$u(x_0) = g_D, \qquad \frac{du}{dx}(x_N) = g_N, \tag{2.2}$$

where g_D and g_N are known constants. In this example the boundary condition specified at x_0 imposes a condition on the solution (Dirichlet-type boundary condition), while the boundary condition specified at x_N imposes a condition on the derivative of the solution (Neumann-type boundary condition). The problem as defined by Eq. 2.1 and Eq. 2.2 is said to be in the *strong form*. Solutions to the strong formulation (called *strong solutions*) of differential problems of order s are s-times differentiable.

Weak formulation

The differential equations that govern a great range of physical phenomena often do not have sufficiently smooth solutions, and therefore do no admit a strong formulation. In these cases, non-differentiable functions that nonetheless satisfy the differential equation can be found by means of a *weak formulation*.

To formulate the example problem in a weak form, Eq. 2.1 is multiplied by an

arbitrary *test* function $v(x)$, and integrated over the domain Ω:

$$\int_{x_0}^{x_N} v\Big(\frac{d^2u}{dx^2} + f\Big)\,\mathrm{d}x = 0. \tag{2.3}$$

The problem posed by Eq. 2.3 is said to be in the *weak form*. The solution to the weak formulation (called *weak solution*) is required to be continuous, but not differentiable.

2.1.1.2 Legendre inner product

Let $f(x)$ and $g(x)$ be two polynomial functions defined in Ω. The Legendre inner product $\langle f, g\rangle$ over the domain Ω is given by

$$\langle f, g\rangle = \int_{x_0}^{x_N} f(x)g(x)\,\mathrm{d}x. \tag{2.4}$$

2.1.1.3 Method of the weighted residuals

Consider the strong form of a generic differential problem $\mathbb{L}(u)$ denoted by

$$\mathbb{L}(u) = 0, \tag{2.5}$$

and the pertinent initial and boundary conditions. An approximated solution $u^\delta = u^\delta(\vec{x}, t)$ can be constructed as a series expansion of the form:

$$u^\delta(\vec{x}, t) = u_0(\vec{x}, t) + \sum_{i=1}^{N_{dof}} \widehat{u}_i(t)\Phi_i(\vec{x}), \tag{2.6}$$

where $\widehat{u}_i(t)$ are the N_{dof} unknown coefficients, Φ_i are the basis (or *trial*) functions of the expansion, and $u_0(\vec{x}, t)$ is a known function that satisfies the initial and boundary conditions.

The approximate solution u^δ does not exactly satisfy the differential Eq. 2.5. The error or residual R between the approximate and the exact solution is given by:

$$R(u^\delta) = \mathbb{L}(u^\delta).$$

The weighted residuals method places a restriction on the residual R in order to calculate the unknown coefficients $\widehat{u}_i(t)$ of the expansion. In particular, the inner product of the residual R and a *weight* (or test) function v_j is required to be zero. Thus,

$$\langle v_j, R \rangle = 0 \qquad\qquad j = 1, ..., N_{dof}. \tag{2.7}$$

The nature of the test functions v_j determines the type of numerical method. A review of the most commonly used test functions and their associated computational methods is given in [129]. Note that Eq. 2.7 is equivalent to the weak formulation of the problem posed by Eq. 2.5.

2.1.2 The Galerkin approximation

The Galerkin approximation is equivalent to the weighted residuals method when the test functions are chosen to be identical to the trial functions (i.e. $v_i = \Phi_i$). In this section a brief overview of the Galerkin approximation is given. For a complete mathematical analysis and a more detailed formulation refer to [129].

2.1.2.1 Example problem

Consider the strong formulation of the one dimensional Helmholtz equation given by

$$\frac{d^2u}{dx^2} - \lambda u + f = 0, \tag{2.8}$$

$$u(x_0) = g_D, \qquad \frac{du}{dx}(x_N) = g_N. \tag{2.9}$$

2.1.2.2 Weak form: implementation of boundary conditions

Implementation of Neumann boundary conditions

The weak formulation of Eq. 2.8 can be expressed as:

$$\int_{x_0}^{x_N} v\Big(\frac{d^2u}{dx^2} - \lambda u + f\Big)\,\mathrm{d}x = 0. \tag{2.10}$$

where the test function $v(x)$ is defined to be zero at all the Dirichlet boundaries (i.e $v(0) = 0$). In the Galerkin approximation Eq. 2.10 is integrated by parts to yield the following expression:

$$\int_{x_0}^{x_N} \frac{dv}{dx}\frac{du}{dx}\,\mathrm{d}x + \lambda \int_{x_0}^{x_N} vu\,\mathrm{d}x = \int_{x_0}^{x_N} vf\,\mathrm{d}x + \Big[v\frac{du}{dx}\Big]_{x_0}^{x_N}.$$

Using Eq. 2.9 and considering that by definition $v(0) = 0$, the previous equation can be expressed as

$$\int_{x_0}^{x_N} \frac{dv}{dx}\frac{du}{dx}\,\mathrm{d}x + \lambda \int_{x_0}^{x_N} vu\,\mathrm{d}x = \int_{x_0}^{x_N} vf\,\mathrm{d}x + v(x_N)g_N. \tag{2.11}$$

Note that the Neumann boundary condition imposed at x_N is naturally included within this weak formulation.

Implementation of Dirichlet boundary conditions

Both the exact solution $u(x)$ and the test function $v(x)$ can be approximated by finite series expansions denoted u^δ and v^δ respectively. Thus, Eq. 2.11 becomes

$$\int_{x_0}^{x_N} \frac{dv^\delta}{dx}\frac{du^\delta}{dx}\,\mathrm{d}x + \lambda \int_{x_0}^{x_N} v^\delta u^\delta\,\mathrm{d}x = \int_{x_0}^{x_N} v^\delta f\,\mathrm{d}x + v^\delta(x_N)g_N. \tag{2.12}$$

The approximate solution u^δ can be expressed as the sum of a known (lifted) solution u^D, and an unknown function u^H such that

$$u^\delta = u^D + u^H, \tag{2.13}$$

where u^D is chosen to satisfy the Dirichlet boundary conditions (i.e. $u^D(x_0) = g_D$); and u^H is a unknown function which value is zero at the Dirichlet boundaries (i.e $u^H(x_0) = 0$).

Substituting Eq. 2.13 into Eq. 2.17 leads to the following expression:

$$\int_{x_0}^{x_N} \frac{dv^\delta}{dx}\Big[\frac{du^D}{dx} + \frac{du^H}{dx}\Big]\,\mathrm{d}x + \lambda \int_{x_0}^{x_N} v^\delta(u^D + u^H)\,\mathrm{d}x = \int_{x_0}^{x_N} v^\delta f\,\mathrm{d}x + v^\delta(x_N)g_N.$$

Hence

$$\begin{aligned}\int_{x_0}^{x_N} \frac{dv^\delta}{dx}\frac{du^H}{dx}\,\mathrm{d}x + \lambda\int_{x_0}^{x_N} v^\delta u^H\,\mathrm{d}x = \\ = \int_{x_0}^{x_N} v^\delta f\,\mathrm{d}x + v^\delta(x_N)g_N - \int_{x_0}^{x_N} \frac{dv^\delta}{dx}\frac{du^D}{dx}\,\mathrm{d}x - \lambda\int_{x_0}^{x_N} v^\delta u^D\,\mathrm{d}x.\end{aligned} \tag{2.14}$$

Since u^D is known and the test functions v^δ are arbitrary, all the elements of the right-hand side of Eq. 2.14 are known. Furthermore, since v^δ and u^H contain a finite number of functions, Eq. 2.14 can be transformed into a system of algebraic equations that can be solved by traditional methods.

Lifting a known solution is a key step in the Galerkin formulation. Since by definition the unknown solution u^H is zero at the Dirichlet boundary conditions, the test function space (chosen to also be zero at the Dirichlet boundary conditions) can be used to span u^H. If a known solution was not lifted, the trial space would have more degrees of freedom than the test space, leading to a algebraic system not squared in nature.

Implementation of Robin boundary conditions

Consider the *mixed* or *Robin* boundary condition given by

$$\alpha\frac{du}{dx}(x_N) = g_R + \beta u(x_N), \tag{2.15}$$

where α, β and g_R are known. Such type of boundary condition often arises in mass transport problems, as shown in subsequent chapters.

Eq. 2.15 can be expressed as:

$$\frac{du}{dx}(x_N) = \frac{1}{\alpha}(g_R + \beta u(x_N)). \tag{2.16}$$

On substituting Eq. 2.16 in Eq. 2.15, one obtains:

$$\begin{aligned}\int_{x_0}^{x_N} \frac{dv^\delta}{dx}\frac{du^\delta}{dx}\,\mathrm{d}x + \lambda\int_{x_0}^{x_N} v^\delta u^\delta\,\mathrm{d}x + \frac{\alpha}{\beta}v^\delta(x_N)u^\delta(x_N) = \\ = \int_{x_0}^{x_N} v^\delta f\,\mathrm{d}x + v^\delta(x_N)g_N.\end{aligned} \tag{2.17}$$

The term $\frac{\alpha}{\beta}v^{\delta}(x_N)u^{\delta}(x_N)$ has been included in the left-hand side of the equation, as the value of $u^{\delta}(x_N)$ is unknown. Note that the inclusion of such term is the only necessary modification when implementing Robin boundary conditions.

Before proceeding with further numerical discussion, it is important to highlight that the Galerkin approximation can be used in a number of numerical methods, as it does not define the type of trial function or the spatial decomposition of the domain. The following section overviews a spectral/hp element implementation of the Galerkin approximation.

2.1.3 A spectral/hp element implementation of the Galerkin approximation

Spectral/hp implementations of the Galerkin approximation require two fundamental steps: 1)the spatial discretisation of the computational domain into elements (a *h-type discretisation*), and 2)the definition of a local series expansion within each element (a *p-type discretisation*).

The first step consists in partitioning the computational domain into smaller separate regions (*elements*). This process is often referred to as defining the computational mesh. Reducing the size of the elements (*h-type refinement*) leads to algebraic convergence for sufficiently smooth problems. The second step defines a local series expansion within each element. Such local expansions are combined to build a global series expansion that represents the approximate solution of the problem within the entire domain. Increasing the number of modes that form the expansion leads to exponential convergence.

2.1.3.1 Elemental decomposition: the h-type extension

Recall the example problem given by Eqs. 2.8 and 2.9. Consider the solution $u(x)$ in the domain $\Omega = \{x \,|\, x_0 \leq x \leq x_3\}$. Let x_1, x_2 be points defined within Ω such

that

$$x_0 \leq x_1 \leq x_2 \leq x_3.$$

Three non-overlapping elements Ω_i can be defined as:

$$\Omega_0 = \{x \,|\, x_0 \leq x \leq x_1\}, \qquad \Omega_1 = \{x \,|\, x_1 \leq x \leq x_2\}, \qquad \Omega_2 = \{x \,|\, x_2 \leq x \leq x_3\}.$$

such that

$$\Omega = \bigcup_{i=0}^{2} \Omega_i, \qquad \bigcap_{i=0}^{2} \Omega_i = \emptyset.$$

Thus defining a valid computational mesh.

2.1.3.2 Spectral expansion: the p-type extension

In the spectral/hp element method, the global expansion basis Φ_k within the domain is constructed from a combination of the local expansion modes ϕ_p defined within each element.

In order to facilitate the numerical implementation of the elemental expansions, a standard element Ω_{st} is defined as $\Omega_{st} = \{\xi \,|\, -1 \leq \xi \leq 1\}$. A transformation function $\chi_i(\xi)$ can be used to map the standard element Ω_{st} to the physical elements Ω_i. Such transformation $\chi_i(\xi)$ expresses the physical (or *global*) coordinate x as a function of the standard (or *local*) coordinate ξ:

$$x(\xi) = \chi_i(\xi) = \Big(\frac{1-\xi}{2}\Big)x_i + \Big(\frac{1+\xi}{2}\Big)x_{i+1}, \qquad \xi \in \Omega_{st}. \tag{2.18}$$

Similarly, a inverse mapping $(\chi^i(\xi))^{-1}$ expressing the local coordinate ξ in terms of the global coordinate x can be defined as

$$\xi(x) = (\chi_i^{-1}(x)) = 2\Big(\frac{x - x_i}{xi - x_{i+1}}\Big) - 1, \qquad x \in \Omega_i.$$

A great range of local expansion basis $\phi_p = \phi_p(\xi)$ can be defined within the standard element. The choice of the local basis will be briefly discussed in a later section (sec. 2.1.3.4). For illustrative purposes, consider now a 3^{th}-order polynomial modal expansion $\phi_p(\xi)$ defined as:

$$\phi_p(\xi) = \begin{cases} \frac{1-\xi}{2} & p = 0, \\ \left(\frac{1-\xi}{2}\right)\left(\frac{1+\xi}{2}\right) P_{p-1}^{1,1} & 0 < p < 2, \\ \frac{1+\xi}{2} & p = 2. \end{cases} \tag{2.19}$$

where $P_p^{1,1}$ denotes the Jacobi polynomials of order p. A C_0 global expansion basis $\Phi_k = \Phi_k(x)$ can be constructed by combining the local expansion modes $\phi_p = \phi_p(\xi)$ and mapping them to the global coordinate system via the transformation χ_i^{-1}. For instance, in the example problem a global expansion $\Phi_k(x)$ can be defined as follows:

$$\Phi_0(x) = \begin{cases} \phi_0(\xi) = \phi_0(\chi_0^{-1}(x)) & x \in \Omega_0 \\ 0 & x \notin \Omega_0 \end{cases} \qquad \Phi_1(x) = \begin{cases} \phi_1(\xi) = \phi_1(\chi_0^{-1}(x)) & x \in \Omega_0 \\ 0 & x \notin \Omega_0 \end{cases}$$

$$\Phi_2(x) = \begin{cases} \phi_2(\xi) = \phi_2(\chi_0^{-1}(x)) & x \in \Omega_0 \\ \phi_0(\xi) = \phi_0(\chi_1^{-1}(x)) & x \in \Omega_1 \\ 0 & x \notin \Omega_0 \cup \Omega_1 \end{cases} \qquad \Phi_3(x) = \begin{cases} \phi_1(\xi) = \phi_1(\chi_1^{-1}(x)) & x \in \Omega_1 \\ 0 & x \notin \Omega_1 \end{cases}$$

$$\Phi_4(x) = \begin{cases} \phi_2(\xi) = \phi_2(\chi_1^{-1}(x)) & x \in \Omega_1 \\ \phi_0(\xi) = \phi_0(\chi_2^{-1}(x)) & x \in \Omega_2 \\ 0 & x \notin \Omega_1 \cup \Omega_2 \end{cases} \qquad \Phi_5(x) = \begin{cases} \phi_1(\xi) = \phi_1(\chi_2^{-1}(x)) & x \in \Omega_2 \\ 0 & x \notin \Omega_2 \end{cases}$$

$$\Phi_6(x) = \begin{cases} \phi_2(\xi) = \phi_2(\chi_2^{-1}(x)) & x \in \Omega_2 \\ 0 & x \notin \Omega_2 \end{cases}$$

Note that the number of local (or elemental) degrees of freedom N_{eof} is higher than the number of global degrees of freedom N_{dof}, as several restrictions apply to the global expansion. In particular, the global expansion basis Φ_k is required to be C_0 continuous. This condition is equivalent to imposing continuity at the boundaries of internal elements. For instance, in the previous example there are nine local degrees

of freedom (N_{eof}=3 elements x 3 local modes per element) but only seven global degrees of freedom ($N_{dof} = 7$), as C_0 continuity is enforced at x_1 and x_2.

Figure 2.1 summarises the concepts reviewed in this section, illustrating a basic implementation of the spectral/hp element method.

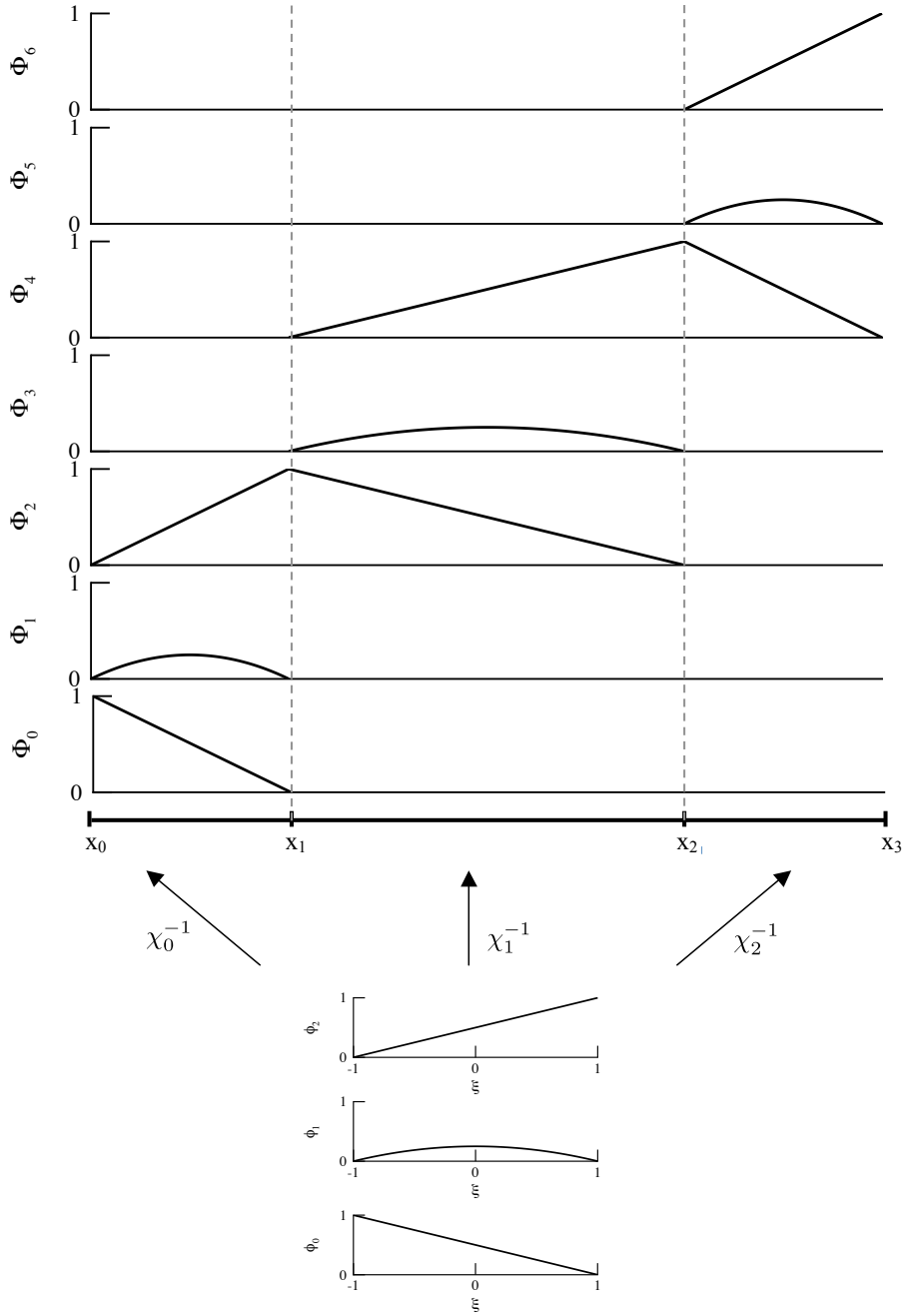


Figure 2.1: Implementation of the spectral/hp element method. The domain Ω is decomposed into three elements Ω_i with $i = 0, 1, 2$. A local expansion basis ϕ_p is defined within the standard element Ω_{st}. The global expansion modes $\Phi_k(x)$ are assembled by combining the local modes $\phi_p(\xi)$ and mapping them to the global space via the transformation χ_i^{-1}.

2.1.3.3 Matrix formulation

Recall the Galerkin formulation (Eq. 2.14) of the example problem. The lifted solution u^D, the unknown solution u^H and the approximate test function v^δ can be expressed in terms of the global expansion basis $\Phi_k(x)$ as:

$$u^D(x) = g_D \Phi_0(x), \tag{2.20}$$

$$u^H(x) = \sum_{k=1}^{N_{dof}-1} \widehat{u}_k \Phi_k(x), \tag{2.21}$$

$$v^\delta(x) = \sum_{l=1}^{N_{dof}-1} \widehat{v}_l \Phi_k(x), \tag{2.22}$$

where $\widehat{u}_k$ are the N_{dof}-1 unknown coefficients to be determined and $\widehat{v}_l$ are arbitrary coefficients since the test function v^δ is arbitrary. Note that the lifted solution is expressed in terms of the global basis. Further, note that the global modes forming the trial space (and hence the test space) are zero at the Dirichlet boundary conditions (see Fig. 2.1).

Substituting Eqs. 2.20, 2.21 and 2.22 into Eq. 2.14 leads to the following expression:

$$\begin{aligned}\sum_{k=1}^{N_{dof}-1}\sum_{l=1}^{N_{dof}-1} \widehat{u}_k\widehat{v}_l \int_{x_0}^{x_N} \frac{d\Phi_k}{dx}\frac{d\Phi_l}{dx}\,\mathrm{d}x + \lambda \sum_{k=1}^{N_{dof}-1}\sum_{l=1}^{N_{dof}-1} \widehat{u}_k\widehat{v}_l \int_{x_0}^{x_N} \Phi_k\Phi_l\,\mathrm{d}x = \\ = \sum_{l=1}^{N_{dof}-1} \widehat{v}_l \int_{x_0}^{x_N} \Phi_l f\,\mathrm{d}x + \widehat{v}_6 g_N - \sum_{l=1}^{N_{dof}-1} \widehat{v}_l g_D \int_{x_0}^{x_N} \frac{d\Phi_l}{dx}\frac{d\Phi_0}{dx}\,\mathrm{d}x - \\ -\lambda \sum_{l=1}^{N_{dof}-1} \widehat{v}_l g_D \int_{x_0}^{x_N} \Phi_l\Phi_0\,\mathrm{d}x.\end{aligned} \tag{2.23}$$

Equation 2.23 can be expressed in a matrix form. Let $\mathbf{L}$ and $\mathbf{M}$ be square matrices such that

$$\mathbf{M}[k][l] = \int_{x_0}^{x_N} \Phi_k\Phi_l\,\mathrm{d}x, \qquad \mathbf{L}[k][l] = \int_{x_0}^{x_N} \frac{d\Phi_k}{dx}\frac{d\Phi_l}{dx}\,\mathrm{d}x.$$

Further, let $\widehat{\mathbf{u}}$, $\widehat{\mathbf{v}}$, $\mathbf{f}$, $\mathbf{d}$ and $\mathbf{n}$ be vectors defined as

$$\widehat{\mathbf{u}}[k] = \widehat{u}_k, \qquad \widehat{\mathbf{v}}[l] = \widehat{v}_l,$$

$$\mathbf{f}[l] = \int_{x_0}^{x_N} \Phi_l f \, \mathrm{d}x, \qquad \mathbf{d}[l] = g_d \Big(\int_{x_0}^{x_N} \frac{d\Phi_l}{dx} \frac{d\Phi_0}{dx} \, \mathrm{d}x + \lambda \int_{x_0}^{x_N} \Phi_l \Phi_0 \, \mathrm{d}x \Big),$$

$$\mathbf{n}[l] = \begin{cases} 0 & l \neq N_{dof} - 1 \\ \widehat{v}_l g_N & l = N_{dof} - 1. \end{cases}$$

Equation 2.23 can now be expressed as:

$$\widehat{\mathbf{v}}^{\mathbf{T}} (\mathbf{L} + \lambda \mathbf{M}) \, \widehat{\mathbf{u}} = \widehat{\mathbf{v}}^{\mathbf{T}} (\mathbf{f} + \mathbf{n} - \mathbf{d}). \tag{2.24}$$

Since the test function v^δ is arbitrary, Eq. 2.24 needs to be satisfied for all $\widehat{v}_k$. Thus

$$(\mathbf{L} + \lambda \mathbf{M}) \, \widehat{\mathbf{u}} = (\mathbf{f} + \mathbf{n} - \mathbf{d}), \tag{2.25}$$

and hence

$$\widehat{\mathbf{u}} = (\mathbf{L} + \lambda \mathbf{M})^{-1} (\mathbf{f} + \mathbf{n} - \mathbf{d}). \tag{2.26}$$

The previous Eq. 2.26 can be used to calculate $\widehat{\mathbf{u}}$, and hence the approximate solution u^δ.

Numerical considerations

The matrices $\mathbf{M}$ and $\mathbf{L}$, generally referred to as the *global mass matrix* and the *global laplacian matrix* respectively, exhibit a degree of structure. Moreover, it can be shown that $\mathbf{M}$ and $\mathbf{L}$ can be assembled from elemental contributions. These two properties can be used to formulate very efficient implementations of the spectral/hp element method. Further discussion on this topic is beyond the scope of this thesis. A complete description of the spectral/hp element method and its numerical implementation can be found in [129].

2.1.3.4 Local expansion bases

Local expansions can be classified as *nodal* or *modal* expansions, according to the nature of their bases. Nodal expansions evaluate the approximate solution at a fixed

set of points (*nodes*), and therefore the unknown coefficients $\widehat{u}_i$ of the approximate solution u^δ have a physical meaning: the value of the solution at a given node. Nodal bases are not hiercharchical, in the sense that a higher order nodal basis cannot be constructed from lower order basis modes. Examples of nodal basis are the expansions formed with Lagrange polynomials. On the other hand, modal bases are hiercharchical in nature, and therefore low order modes are contained within higher order expansions. The basis given by Eq. 2.19 is an example of modal basis.

The choice of the local expansion basis strongly affects the numerical implementation and hence the efficiency of spectral/hp element methods. Factors such as the orthogonality and the linear independence of the basis modes have a great influence in the conditioning of the laplacian and mass matrices. For a complete discussion on the choice of local expansions refer to [129].

2.1.3.5 Extension to multiple dimensions

The one-dimensional concepts previously reviewed can be extended into multiple dimensions. While extending the formulation of the Galerkin approximation into higher dimensions is straightforward, the construction of local basis within 2D and 3D standard regions presents greater difficulty. This section briefly discusses suitable standard regions and possible local expansions for a number of two and three dimensional elemental geometries.

Quadrilateral and Hexahedral Elements

A structured partition of the computational mesh results in the generation of quadrilateral (2D) or hexahedral (3D) elements. For this type of elements, the extension to multiple dimensions is relatively simple, as reviewed in subsequent text.

Consider the standard domains $\mathcal{Q}_{st}^{2D}$ and $\mathcal{Q}_{st}^{3D}$ defined as

$$\mathcal{Q}_{st}^{2D} = \{(\xi_1, \xi_2) \,|\, -1 \leq \xi_1, \xi_2 \leq 1\},$$

and

$$\mathcal{Q}_{st}^{3D} = \{(\xi_1, \xi_2, \xi_3) \,|\, -1 \leq \xi_1, \xi_2, \xi_3 \leq -1\},$$

where ξ_1, ξ_2 and ξ_3 form a Cartesian coordinate system as shown in Fig. 2.2 [1].

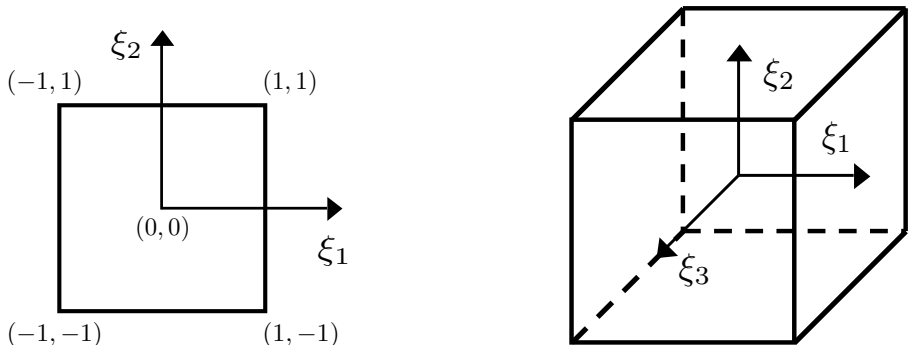


Figure 2.2: Standard regions $\mathcal{Q}_{st}^{2D}$ and $\mathcal{Q}_{st}^{3D}$ for (a)quadrilateral and (b)hexahedral elements respectively.

A one-dimensional basis $\psi_p(\xi_i)$ can be defined along each standard coordinate ξ_i. A multiple dimensional local basis (ϕ_{pq}, ϕ_{pqr}) can now be constructed by taking the tensor product of such one-dimensional bases, that is:

$$\phi_{pq}(\xi_1,\xi_2) = \psi_p(\xi_1)\psi_q(\xi_2) \qquad 0 \le p,q,\ p \le P_1,\ q \le P_2,$$

$$\phi_{pqr}(\xi_1,\xi_2) = \psi_p(\xi_1)\psi_q(\xi_2)\psi_r(\xi_3) \qquad 0 \le p,q,\ p \le P_1,\ q \le P_2, r \le P_3.$$

The one-dimensional bases $\psi_p(\xi_i)$ are often referred to as *principal functions*. Note that the order of the local expansion in each of the standard directions may vary, as the order P_i of the principal functions $\psi_p(\xi_i)$ may differ.

Triangular and Tetrahedral Elements

Simplex (triangular-faced) elements are generally the result of an unstructured partition of the computational mesh. In this section, the construction of a local basis for triangular (2D) and tetrahedral (3D) elements is reviewed. A definition of local bases within prismatic and pyramidical elements is given in [129].

[1] A transformation function $\chi = \chi(\xi_1,\xi_2,\xi_3)$ to map the standard elements to the global coordinates can be defined in a similar way to the one-dimensional case (Eq. 2.18). A review of multidimensional mappings between the standard and physical regions is given in a later section.

Triangular elements

Consider the standard domains $\mathcal{T}_{st}^{2D}$ defined as

$$\mathcal{T}_{st}^{2D} = \{(\xi_1, \xi_2) \,|\, -1 \leq \xi_1, \xi_2,\, \xi_2 + \xi_1 \leq 0, \}$$

where ξ_1, ξ_2 form a Cartesian coordinate system as shown in Fig. 2.3(a).

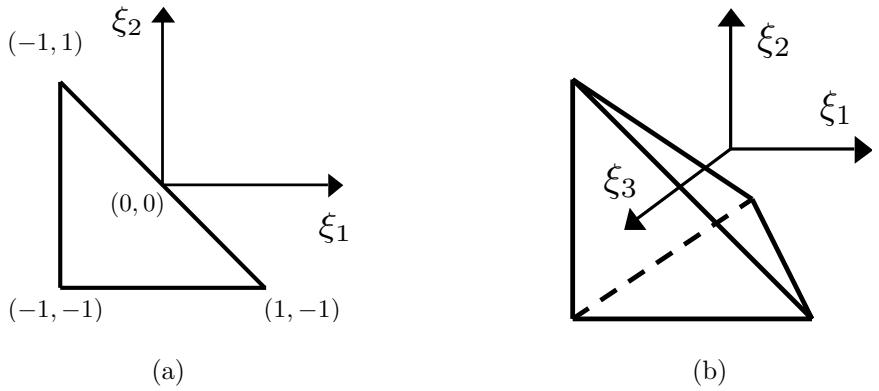


Figure 2.3: Standard regions $\mathcal{T}_{st}^{2D}$ and $\mathcal{T}_{st}^{3D}$ for (a)triangular and (b)tetrahedral elements respectively.

It can be noted that the upper bound of such a coordinate system is not fixed, but depends on the standard coordinates themselves. A new local coordinate system with fixed bounds can be defined using the following transformation:

$$\eta_1 = 2\left(\frac{1+\xi_1}{1-\xi_2}\right) - 1, \qquad \eta_2 = \xi_2. \tag{2.27}$$

The standard region $\mathcal{T}_{st}^{2D}$ can now be expressed in terms of η_1 and η_2 as:

$$\mathcal{T}_{st}^{2D} = \{(\eta_1, \eta_2) \,|\, -1 \leq \eta_1, \eta_2 \leq 1\}.$$

Note that the transformation given by Eq. 2.27 is equivalent to mapping the standard triangular region to the standard quadrilateral region. For this reason, the coordinate system (η_1,η_2) is often referred to as the *collapsed coordinate system.*

When using a collapsed coordinate system, it is not possible to directly construct the local multidimensional modes $\phi_{pq}(\xi_1, \xi_2)$ from the tensor product of principal functions $\psi_p(\xi_i)$. However, it can be shown that $\phi_{pq}(\xi_1, \xi_2)$ can be defined as the

product of a one-dimensional tensor $\psi_p(\eta_1(\xi_1, \xi_2))$ and a two-dimensional tensor $\psi_{pq}(\eta_2(\xi_2))$ such that

$$\phi_{pq}(\xi_1, \xi_2) = \psi_p(\eta_1)\psi_{pq}(\eta_2) \qquad 0 \leq p, q,\ p \leq P_1,\ q \leq P_2.$$

where $\psi_p(\eta_1)$ and $\psi_{pq}(\eta_2)$ are defined as :

$$\psi_p(z) = \begin{cases} \frac{1-z}{2} & p = 0 \\ \left(\frac{1-z}{2}\right)\left(\frac{1+z}{2}\right)P_{p-1}^{1,1} & 1 \leq p < P \\ \frac{1+z}{2} & p = P, \end{cases} \tag{2.28}$$

$$\psi_{pq}(z) = \begin{cases} \psi_p(z) & p = 0,\ 0 \leq q \leq Q \\ \left(\frac{1-z}{2}\right)^{i+1} & 1 \leq p < P,\ q = 0 \\ \left(\frac{1-z}{2}\right)^{i+1}\left(\frac{1+z}{2}\right)P_{q-1}^{2p+1,1} & 1 \leq p < P,\ 1 \leq q < Q \\ \psi_p(z) & p = P,\ 0 \leq q \leq Q. \end{cases} \tag{2.29}$$

The expansions $\psi_p(\eta_1)$ and $\psi_{pq}(\eta_2)$ are known as *modified* principal functions. Note that, unlike quadrilateral expansions, such functions are not independent, as $\psi_{pq}(\eta_2)$ takes a different form for each mode of $\psi_p(\eta_1)$. Figure 2.4 shows the bidimensional basis $\phi_{pq}(\xi_1, \xi_2)$ defined in the standard element $\mathcal{T}_{st}^{2D}$.

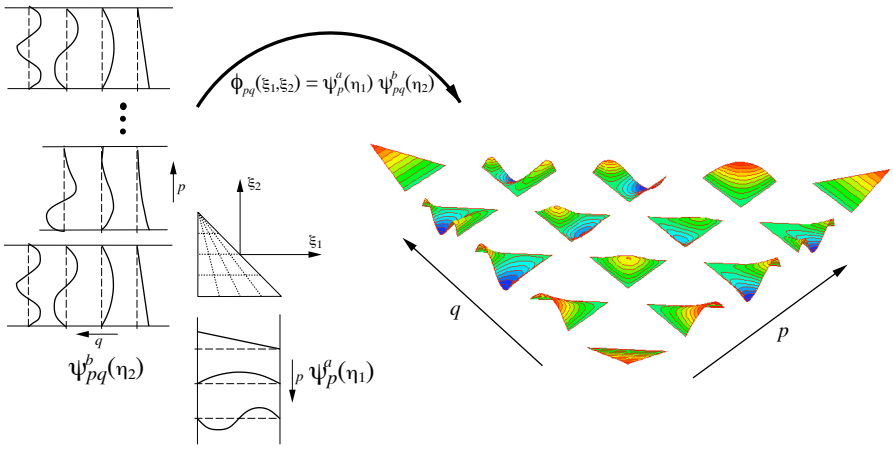


Figure 2.4: 4^{th}-order bidimensional basis $\phi_{pq}(\xi_1, \xi_2)$ defined in the standard element $\mathcal{T}^{2D}_{st}$. The basis $\phi_{pq}(\xi_1, \xi_2)$ is constructed by multiplying the one-dimensional tensor $\psi_p(\eta_1(\xi_1, \xi_2))$ by the two-dimensional tensor $\psi_{pq}(\eta_2(\xi_2))$. Note that the modes within the expansion $\phi_{pq}(\xi_1, \xi_2)$ can be classified as *vertex modes* (modes that have unit value in one vertex and zero in the rest), *edge modes* (modes that have non-zero values along one edge and decay to zero in the remaining edges) and *interior modes* (modes that have non-zero values at the boundary) [129]

.

Tetrahedral elements

Consider the standard domain $\mathcal{T}^{3D}_{st}$ defined as

$$\mathcal{T}^{3D}_{st} = \{(\xi_1, \xi_2, \xi_3) \,|\, -1 \leq \xi_1, \xi_2, \xi_3,\ \xi_1 + \xi_2 + \xi_3 \leq -1\},$$

where ξ_1, ξ_2 and ξ_3 form a Cartesian coordinate system as shown in Fig. 2.3(b). A collapse coordinate system (η_1, η_2, η_3) such that

$$\mathcal{T}^{3D}_{st} = \{(\eta_1, \eta_2, \eta_3) \,|\, -1 \leq \eta_1, \eta_2, \eta_3 \leq 1\},$$

can be defined through the following transformation:

$$\eta_1 = 2\left(\frac{1+\xi_1}{-\xi_2-\xi_3}\right) - 1, \qquad \eta_2 = 2\left(\frac{1+\xi_2}{1-\xi_3}\right) - 1, \qquad \eta_3 = \xi_3. \tag{2.30}$$

It can be shown that the Eq. 2.30 is equivalent to repeatedly collapsing quadrangular faces within the hexahedral standard region. Therefore such a transformation can be though of as a mapping from an hexahedral to a tetrahedral element.

As for triangular local expansions, a local 3D expansion bases $\phi_{pqr}(\xi_1, \xi_2, \xi_3)$ can be defined in terms of the modified principal functions $\psi_p(\eta_1(\xi_1, \xi_2, \xi_3))$, $\psi_{pq}(\eta_2(\xi_2, \xi_3))$ and $\psi_{pqr}(\eta_3(\xi_3))$ as follows:

$$\phi_{pqr}(\xi_1, \xi_2, \xi_3) = \psi_p(\eta_1)\psi_{pq}(\eta_2)\psi_{pqr}(\eta_3) \qquad 0 \leq p, q,\ p \leq P_1,\ q \leq P_2;\ r \leq P_3.$$

A range of suitable modified principal functions $\psi_{pqr}(\eta_3)$ is given in [129], along with further discussion regarding the numerical implementation of the concepts reviewed in this section.

2.1.4 Navier-Stokes equations

This thesis investigates blood flow features within the rabbit aorta. This section gives an overview of the temporal discretisation of the equations that govern the rabbit haemodynamics. Note that the spatial discretisation of such equations is performed using the spectral/hp element method as previously described.

Blood flow is modelled using the steady-state incompressible Navier-Stokes equations for a Newtonian flow. Thus

$$\nabla \cdot \mathbf{u} = 0 \qquad \text{in } \Omega, \tag{2.31}$$

and

$$\frac{\partial \mathbf{u}}{\partial t} + \mathbf{u} \cdot \nabla \mathbf{u} = -\frac{1}{\rho}\nabla p + \nu \nabla^2 \mathbf{u} \qquad \text{in } \Omega, \tag{2.32}$$

where Ω is the computational domain, t is the time, $\mathbf{u}$ represents the velocity vector, p denotes the pressure field, ρ is the blood density and ν represents blood viscosity. By defining the operators $\mathbf{L}$ and $\mathbf{N}$ as

$$\mathbf{L} = \nabla^2 \mathbf{u},$$

and

$$\mathbf{N} = \mathbf{u} \cdot \nabla \mathbf{u},$$

Eq. 2.32 can be expressed as

$$\frac{\partial \mathbf{u}}{\partial t} = -\frac{1}{\rho}\nabla p + \nu \mathbf{L}(\mathbf{u}) + \mathbf{N}(\mathbf{u}). \tag{2.33}$$

The time discretisation follows a high-order splitting scheme ([67]) given by

$$\frac{\widehat{\mathbf{u}}-\mathbf{u}^n}{\Delta t}=\sum_{q=0}^{J_e-1}\beta_q\mathbf{N}(\mathbf{u}^{n-q}) \qquad \text{in } \Omega,$$

$$\frac{\widehat{\widehat{\mathbf{u}}}-\widehat{\mathbf{u}}}{\Delta t}=-\nabla\bar{p}^{n+1} \qquad \text{in } \Omega,$$

and

$$\frac{\mathbf{u}^{n+1}-\widehat{\widehat{\mathbf{u}}}}{\Delta t}=\nu\sum_{q=0}^{J_i-1}\gamma_q\mathbf{L}(\mathbf{u}^{n+1-q}) \qquad \text{in } \Omega; \tag{2.34}$$

where

$$\nabla\bar{p}^{n+1}=\frac{1}{\Delta t}\int_{t_n}^{t_n+1}\nabla p\,\mathrm{d}x,$$

$\mathbf{u}^n$ represents the velocity field at $t=t^n$ and $\Delta t=t^{n+1}-t^n$. The parameters β_q are the coefficients of an explicit J_e-order Adams-Bashforth scheme used to approximate the non-linear operator $\mathbf{N}$, while γ_q are the coefficients of an implicit J_i-order Adams-Moulton scheme used to approximate the linear operator $\mathbf{L}$.

It can be shown [67] that the pressure field can be separately calculated through the following elliptic system of equations:

$$\nabla^2\bar{p}^{n+1}=\nabla\cdot\left(\frac{\widehat{\mathbf{u}}}{\Delta t}\right) \qquad \text{in } \Omega,$$

$$\frac{\partial\bar{p}^{n+1}}{\partial n}=\frac{\vec{u_0}\cdot\mathbf{n}-\widehat{\mathbf{u}}\cdot\mathbf{n}}{\Delta t} \qquad \text{on } \partial\Omega;$$

where $\vec{u_0}$ is the Dirichlet boundary condition at $\partial\Omega$, (i.e. $\mathbf{u}=\vec{u_0}$ at $\partial\Omega$) and $\mathbf{n}$ is a unit vector normal to the boundary $\partial\Omega$.

Splitting errors can be minimised by imposing the following mixed implicit/explicit boundary condition for the pressure:

$$\frac{\partial\bar{p}^{n+1}}{\partial n}=\mathbf{n}\cdot\left[\sum_{q=0}^{J_c-1}\beta_q\mathbf{N}(\mathbf{u}^{n-q})+\nu\sum_{q=0}^{J_i-1}\gamma_q\mathbf{L}(\mathbf{u}^{n+1-q})\right] \qquad \text{on } \partial\Omega.$$

Once the pressure field is estimated, Eq. 2.34 becomes a Helmholtz equation for $\mathbf{u}^{n+1}$, and therefore it can be solved using the spectral/hp element method as reviewed in section 2.1.3. Note that since some of the terms in Eq. 2.34 are treated explicitly, Δt needs to satisfy a Courant–Friedrichs–Lewy (CFL) condition [29] to guarantee the stability of the aforementioned time scheme.

2.1.5 Advection-Diffusion-Reaction equation

This thesis investigates Nitric Oxide (NO) concentration (C_{NO}) in *in vitro* and *in vivo* environments. This section overviews the temporal discretisation of the equations that govern NO transfer. Note that the spatial discretisation of such equations is carried out using the spectral/hp element method.

Nitric oxide transport is governed by the Advection-Diffusion-Reaction equation, given by

$$\frac{\partial C_{NO}}{\partial t} = -\vec{v} \cdot \vec{\nabla} C_{NO} + D_{NO} \nabla^2 C_{NO} - V_{NO}, \tag{2.35}$$

where t is time, $\vec{v}$ is the convective velocity field, D_{NO} is NO diffusivity and V_{NO} is the rate at which NO is consumed by various chemical reactions. NO consumption (V_{NO}) can be modelled as

$$V_{NO} = k_i C_{NO}^m,$$

where k_i is the NO reaction rate with a given substance, and m is the order of such reaction.

2.1.5.1 First-order reaction (*in vivo* nitric oxide transport)

Vascular Nitric Oxide reacts with the haemoglobin (Hb) contained in red blood cells. The kinetics of such reaction are thought to be first order, thus

$$V_{NO} = k_{Hb} C_{NO},$$

and hence

$$\frac{\partial C_{NO}}{\partial t} = -\vec{v} \cdot \vec{\nabla} C_{NO} + D_{NO} \nabla^2 C_{NO} - k_{Hb} C_{NO}. \tag{2.36}$$

Eq. 2.36 can be discretised in time following a semi-implicit first-order scheme :

$$\frac{C_{NO}^{n+1} - C_{NO}^n}{\Delta t} = -\vec{v}^n \cdot \vec{\nabla} C_{NO}^n + D_{NO} \nabla^2 C_{NO}^{n+1} - k_{Hb} C_{NO}^{n+1}, \tag{2.37}$$

where C_{NO}^n represent NO concentration at $t = t^n$, $\vec{v}^n$ denotes the velocity field at $t = t^n$, and $\Delta t = t^{n+1} - t^n$. Since the convective term is treated explicitly, Δt is

chosen to satisfy a CFL condition that guarantees the stability of the time scheme. On reordering the terms in Eq .2.37 one obtains:

$$\nabla^2 C_{NO}^{n+1} - \frac{1}{D_{NO}}\Big(\frac{1}{\Delta t} + k_{Hb}\Big)C_{NO}^{n+1} = -\frac{1}{D_{NO}}\Big(\frac{C_{NO}^{n}}{\Delta t} - \vec{v}^{n} \cdot \vec{\nabla} C_{NO}^{n}\Big),$$

which is a Helmholtz equation for C_{NO}^{n+1}, and therefore can be solved as studied in section 2.1.3.

2.1.5.2 Second-order reaction (*in vitro* nitric oxide transport)

In aqueous solutions, NO reacts with oxygen. The kinetics of NO auto-oxidation can be represented by the following pseudo-second order reaction:

$$V_{NO} = k_{O_2}(C_{NO})^2,$$

and hence

$$\frac{\partial C_{NO}}{\partial t} = -\vec{v} \cdot \vec{\nabla} C_{NO} + D_{NO}\nabla^2 C_{NO} - k_{O_2}(C_{NO})^2. \tag{2.38}$$

Eq. 2.38 can be discretised in time following an semi-implicit first-order scheme :

$$\frac{C_{NO}^{n+1} - C_{NO}^{n}}{\Delta t} = -\vec{v}^{n} \cdot \vec{\nabla} C_{NO}^{n} + D_{NO}\nabla^2 C_{NO}^{n+1} - k_{O_2}(C_{NO}^{n})^2. \tag{2.39}$$

Note that for these cases both the convective and the reaction terms are treated explicitly. Numerical experiments were carried out to ensure the stability of such numerical scheme for the range of parameters investigated. Δt is now chosen to satisfy a more general stability condition that addresses the effect of NO reaction.

On reordering the terms in Eq. 2.39 one obtains

$$\nabla^2 C_{NO}^{n+1} - \frac{1}{D_{NO}\Delta t}C_{NO}^{n+1} = -\frac{1}{D_{NO}}\Big(\frac{C_{NO}^{n}}{\Delta t} - \vec{v}^{n} \cdot \vec{\nabla} C_{NO}^{n} - k_{O_2}(C_{NO}^{n})^2\Big),$$

which again is a Helmtholtz equation for C_{NO}^{n+1} and hence can be solved using the spectral/hp element method as reviewed in section 2.1.3.

2.2 High-order mesh generation

This section overviews numerical issues concerning the generation of high-order (curvilinear) computational meshes suitable for spectral/hp element methods. High-order mesh generation algorithms are relatively scarce in the literature, since traditional (straight-sided) mesh generation techniques cannot be trivially extended to spectral/hp approaches.

Computational meshes for high-order schemes are typically coarser than those for use with low-order methods. Therefore, curved surface elements may be required in order for high-order meshes to conform to the boundary geometry. This requirement may lead to distorted or even *invalid* [2] boundary elements, such as the ones illustrated in Fig. 2.5.

Defining a mesh generation algorithm that controls the occurrence of invalid elements is a difficult task. A more practical approach is to initially define a underlying straight-sided mesh (straight-sided meshes do not present so called invalid elements and can be generated using commercial software), and thereafter deform it to create a curvilinear conforming mesh. Note that a limited number of invalid elements can be introduced during the deformation process. However, a number of strategies can be followed to minimise their incidence [130] and to correct such elements [129].

This section firstly reviews fundamental concepts of high-order mesh generation, and subsequently presents an algorithm to curve straight-sided meshes using so called SPHERIGON patches [147].

[2] Invalid elements are those whose mapping function between the standard and the physical regions is not bijective, and hence the jacobian of such mapping function is not strictly positive.

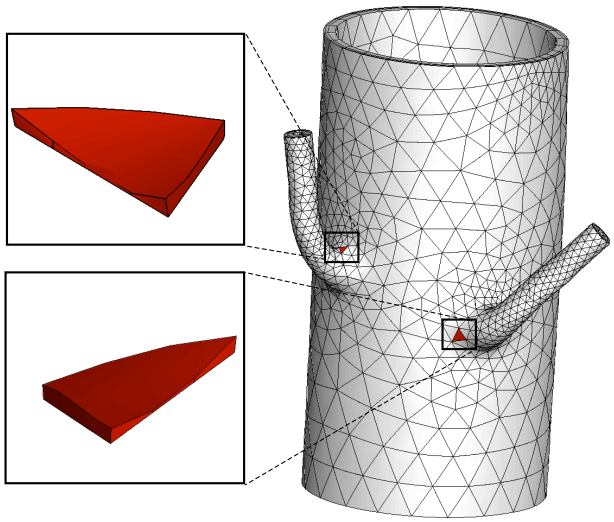


Figure 2.5: Invalid elements (in red) in a high-order representation of the third pair of intercostal arteries in the rabbit aorta.

2.2.1 High-order meshes in spectral/hp element methods

The spectral/hp element method requires the definition of mappings χ_i between the physical elements Ω_i and the standard region Ω_{st}. The construction of such mappings depends significantly on the nature (straight-sided or curvilinear) of the physical elements being mapped.

This section describes mappings for both straight-sided and curvilinear elements. For simplicity, only high-order mappings for quadrilateral elements are reviewed. An extension to triangular and 3D elements can be found in [129].

2.2.1.1 Elemental mappings for straight-sided elements

Consider a quadrangular element of vertices A (x_1^A, x_2^A), B (x_1^B, x_2^B), C (x_1^C, x_2^C) and D(x_1^C, x_2^C). A mapping χ between such an element and the standard quadrilateral

region (Fig. 2.6) is given by:

$$x_i = \chi(\xi_1, \xi_2) = x_i^A \Big(\frac{1-\xi_1}{2}\Big)\Big(\frac{1-\xi_2}{2}\Big) + x_i^B \Big(\frac{1+\xi_1}{2}\Big)\Big(\frac{1-\xi_2}{2}\Big) +$$

$$+ x_i^C \Big(\frac{1-\xi_1}{2}\Big)\Big(\frac{1+\xi_2}{2}\Big) + x_i^D \Big(\frac{1+\xi_1}{2}\Big)\Big(\frac{1+\xi_2}{2}\Big), \quad i = 1, 2.$$

It can be shown that the previous mapping is bijective (and hence does not generate invalid elements) provided that the internal angles of the quadrilateral element are convex (that is, there are less than 180 degrees).

2.2.1.2 Elemental mappings for curvilinear elements

In spectral/hp element methods the boundary geometry can be approximated in terms of the local expansion modes. Therefore, a high-order mapping χ can be defined as

$$x_i = \chi(\xi_1, \xi_2) = \sum_{p=0}^{p=P1} \sum_{q=0}^{q=P2} \widehat{x}_{pq}^i \phi_{pq}(\xi_1, \xi_2), \tag{2.40}$$

where $\phi_{pq}(\xi_1, \xi_2)$ is the local expansion basis (see section 2.1.3.5) and $\widehat{x}_{pq}^i$ are the unknown coefficients of the mapping to be determined. Note that when the all the modes within $\phi_{pq}(\xi_1, \xi_2)$ are zero, except for the vertex modes (i.e. $\widehat{x}_{pq}^i = 0$, except for $\widehat{x}_{00}^i = x_i^A$, $\widehat{x}_{P_1 0}^i = x_i^B$, $\widehat{x}_{P_1 P_2}^i = x_i^C$ and $\widehat{x}_{0 P_2}^i = x_i^D$) the straight-sided mapping is recovered.

Consider a quadrangular element of curved edges a, b, c and d (see Fig. 2.6). Further, consider that the geometry of the edge k is known and it can be represented by a function $f^k(\xi_i)$. Provided that the edge definitions are continuous at the vertices (e.g. $f^a(1) = f^b(-1)$), it is possible [52] to construct a mapping $\chi(\xi_1, \xi_2)$ as a linear

blending of the functions f^k as follows:

$$\begin{aligned}\chi_(\xi_1,\xi_2) = f^a(\xi_1)\Big(\frac{1-\xi_2}{2}\Big) + f^c(\xi_1)\Big(\frac{1+\xi_2}{2}\Big) + f^d(\xi_2)\Big(\frac{1-\xi_1}{2}\Big) + f^b(\xi_2)\Big(\frac{1+\xi_1}{2}\Big) \\ - f^a(-1)\Big(\frac{1-\xi_1}{2}\Big)\Big(\frac{1-\xi_2}{2}\Big) - f^a(1)\Big(\frac{1+\xi_1}{2}\Big)\Big(\frac{1-\xi_2}{2}\Big) \\ - f^c(-1)\Big(\frac{1-\xi_1}{2}\Big)\Big(\frac{1+\xi_2}{2}\Big) - f^c(1)\Big(\frac{1+\xi_1}{2}\Big)\Big(\frac{1+\xi_2}{2}\Big).\end{aligned} \tag{2.41}$$

Recall that $\phi_{pq}(\xi_1,\xi_2) = \psi(\xi_1)\psi(\xi_2)$ within the quadrilateral standard element. The functions f^k can therefore be approximated by an expansion $\bar{f}^k$ in terms of the principal functions $\psi(\xi_i)$. For instance:

$$f^a \approx \bar{f}^a = \sum_{p=0}^{p=P_1} \widehat{f}^a(\xi_j) h_p(\xi_1) = \sum_{p=0}^{p=P_1} \widehat{u}_{p0}\psi_p(\xi_1), \tag{2.42}$$

where $h_p(\xi_1)$ is a nodal basis (e.g. Lagrange basis) defined within the standard space and ξ_j are the nodes of such basis, hence $\widehat{f}^a(\xi_j) = f^a(\xi_j)$. The modal mapping coefficients $\widehat{u}_{p0}$ can be determined as:

$$\widehat{\mathbf{u}}^T = \widehat{\mathbf{f}}^T\ \mathbf{h}\ \mathbf{d}^{-1}, \tag{2.43}$$

where the vectors $\widehat{\mathbf{f}}$, $\widehat{\mathbf{u}}$, $\mathbf{h}$ and $\mathbf{d}$ are defined as

$$\widehat{\mathbf{f}}[l] = \widehat{f}^k(\xi_l), \qquad \widehat{\mathbf{u}}[l] = \widehat{u}_{0l}, \qquad \mathbf{h} = h_l(\xi_1), \qquad \mathbf{d}[l] = \phi_l(\xi_1), \quad 0 \le l \le P_1.$$

Substituting the functions f^k in Eq. 2.41 by their approximations $\bar{f}^k$ leads to an expression of the mapping $\chi_(\xi_1,\xi_2)$ in the form given by Eq. 2.40, where the coefficients $\widehat{x}^i_{pq}$ are now known. Fig. 2.6 illustrates the construction of the mapping $\chi_(\xi_1,\xi_2)$ as described above.

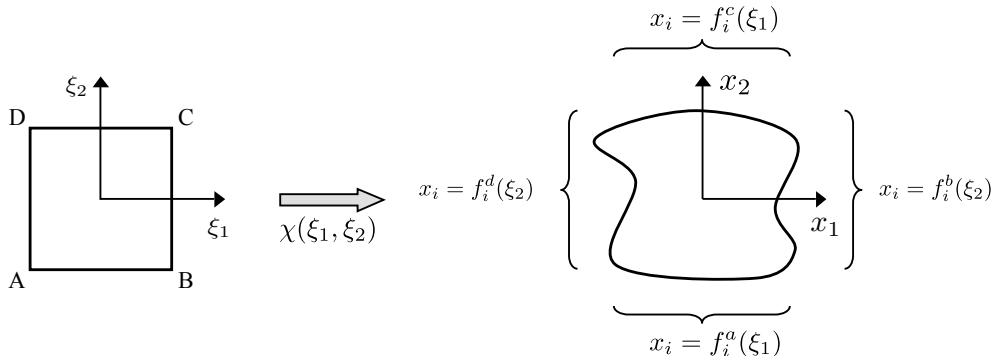


Figure 2.6: Construction of a mapping $\chi(\xi_1, \xi_2)$ between a curved quadrangular element and the standard space. Such a mapping is constructed by linear blending of the edge definitions f^k.

2.2.2 High-order mesh generation using SPHERIGON patches

The analytic functions f^k that describe the edges geometry (or the faces in 3D problems) are often unknown, and therefore the nodal coefficients $\widehat{f^k}$ need to be estimated. Once such nodal coefficients $\widehat{f^k}$ are known, the modal mapping coefficients can be directly determined using Eq. 2.43.

Most of the estimation techniques available are based on approximating the surface geometry by high-order patches. Such patches are generally constructed using the topological information contained in an underlying straight-sided mesh.

SPHERIGON patches [147] provide a curvilinear approximation of a polygonal element given its vertices and vertex normals. This section describes a mesh generation algorithm based on such patches [54] and proposes a new algorithm to accurately approximate the vertex normals from a coarse straight-sided mesh.

2.2.2.1 The SPHERIGON patch

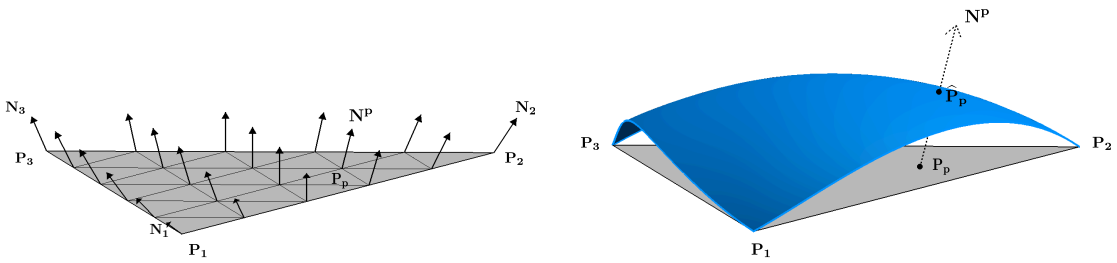
The SPHERIGON patch allows the approximation of a curved polygonal surface given its vertices and vertex normals. Specifically, the SPHERIGON patch approx-

imates a curved polygon of n vertices by blending n spherical surfaces orthogonal to the n vertex normals at the n vertices. The blending functions are chosen to guarantee C_0 and C_1 across patches. The process of constructing a SPHERIGON patch is outlined below.

Consider a triangle with vertices $\mathbf{P_1}$, $\mathbf{P_2}$ and $\mathbf{P_3}$ and vertex normals $\mathbf{N_1}$, $\mathbf{N_2}$ and $\mathbf{N_3}$. Let $\mathbf{P_p}$ be an arbitrary point within such triangle, and $\mathbf{N^p}$ the Phong normal at the point $\mathbf{P_p}$ defined as:

$$\mathbf{N^p} = \frac{\sum_{i=1}^{3} r_i \mathbf{N_i}}{|| \sum_{i=1}^{3} r_i \mathbf{N_i} ||},$$

where r_i are the barycentric coordinates of the point $\mathbf{P}$ (i.e. $\mathbf{P_p} = \sum_{i=1}^{3} r_i \mathbf{P_i}$). Further, let $\widehat{\mathbf{P}}_\mathbf{p}$ be the Phong projection of $\mathbf{P_p}$ onto the SPHERIGON patch (see Fig. 2.7).



(a) (b)

Figure 2.7: Phong normals distribution (a) and Phong projection (b). The SPHERIGON patch (blue) provides a curvilinear approximation of a polygonal element given its vertices $\mathbf{P_i}$ and vertex normals $\mathbf{N_i}$.

The SPHERIGON patch at the point $\mathbf{P_p}$ ($\widehat{\mathbf{P}}_\mathbf{p}$) is constructed by blending the three spheres S_i orthogonal to $\mathbf{N_i}$ at $\mathbf{P_i}$ and orthogonal to the line defined by $\mathbf{P_p}$ and $\mathbf{N^p}$. Let $\mathbf{Q_i^p}$ be the point where the sphere S_i intersects the line defined by $\mathbf{P_p}$ and $\mathbf{N^p}$, as illustrated in Fig 2.8. It can be shown [147] that

$$\mathbf{Q_i^p} = \mathbf{K_i^p} + \frac{(\mathbf{P_i} - \mathbf{K_i})\mathbf{N_i}}{1 + \mathbf{N^p N_i}},$$

where $\mathbf{K_i^p}$ is the orthogonal projection of $\mathbf{P_i}$ onto the line defined by $\mathbf{P_p}$ and $\mathbf{N^p}$ given by

$$\mathbf{K_i^p} = \mathbf{P_p} + ((\mathbf{P_i} - \mathbf{P_p})\mathbf{N^p})\mathbf{N^p}.$$

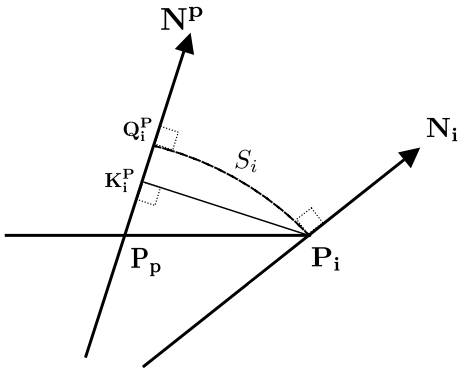


Figure 2.8: Construction of a sphere S_i orthogonal to $\mathbf{N_i}$ at $\mathbf{P_i}$ and orthogonal to the line defined by $\mathbf{P_p}$ and $\mathbf{N^p}$.

The point $\widehat{\mathbf{P}}_\mathbf{p}$ can now be determined by the blending of the points $\mathbf{Q_i^p}$. Thus

$$\widehat{\mathbf{P}}_\mathbf{p} = \sum_{i=1}^{3} f_i^p \mathbf{Q_i^p}$$

where f_i^p are blending functions chosen to guarantee C_0 and C_1 across patches [147] defined by:

$$f_i^p = r_i^2\Big(\frac{r_{i-1}^2(\mathbf{Q_{i-1}^p} - \mathbf{P_p})^2}{(\mathbf{Q_{i-1}^p} - \mathbf{P_p})^2 + (\mathbf{Q_i^p} - \mathbf{P_p})^2} + \frac{r_{i+1}^2(\mathbf{Q_{i+1}^p} - \mathbf{P_p})^2}{(\mathbf{Q_{i+1}^p} - \mathbf{P_p})^2 + (\mathbf{Q_i^p} - \mathbf{P_p})^2}\Big),$$

where i is cyclic index.

Since the points $\mathbf{P_p}$ are arbitrary, they can be chosen to be the nodes $\mathbf{x}(\bar{\xi}_j)$ of the nodal expansion $h_p(\bar{\xi})$. Therefore the nodal coefficients $f^k(\bar{\xi}_j)$ can be approximated by $\widehat{\mathbf{P}}_\mathbf{p}$. Hence

$$\mathbf{x}(\bar{\xi}_j) = \mathbf{P_p}, \qquad f(\bar{\xi}_j) = \widehat{\mathbf{P}}_\mathbf{p}.$$

2.2.2.2 Vertex normal approximation

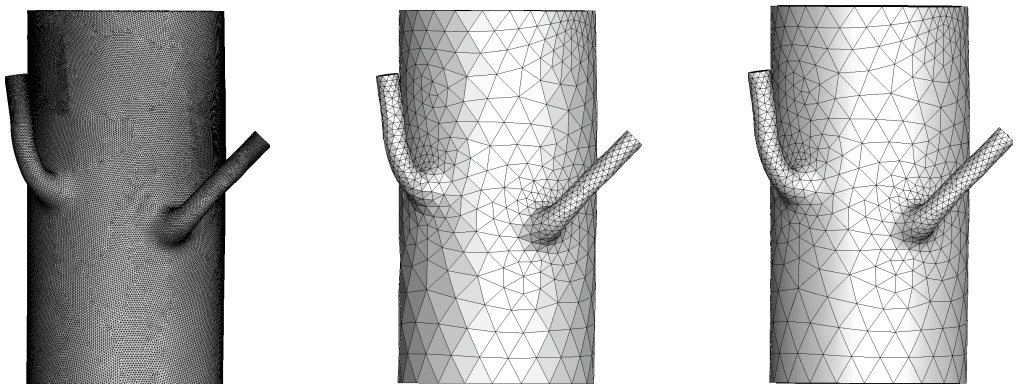
Given a straight-sided mesh, the normal $\mathbf{N_i}$ at the vertex $\mathbf{V_i}$ can be approximated by averaging the face normals $\mathbf{N_j}$ of the elements Ω_j connected to such vertex $\mathbf{V_i}$

(see Fig. 2.10). That is

$$\mathbf{N_i} = \frac{1}{\sum_{j=1}^{n} A_j} \sum_{j} \mathbf{N_j} A_j,$$

where A_j is the face area of the element Ω_j. The accuracy of such an algorithm strongly depends on the size of the mesh. A poor vertex approximation result in computational meshes that are not C_1 continuous, as illustrated later in Fig. 2.11. Since computational meshes for high-order methods are coarse, an alternative method to estimate the vertex normals may be necessary. This thesis proposes the use of an auxiliary straight-sided mesh (Fig. 2.9(a)) to compute the vertex normals, as described next.

Consider the coarse straight-sided mesh $\mathcal{M}$ shown in Fig. 2.9(b) and the finer discretisation of such mesh $\bar{\mathcal{M}}$ shown in Fig. 2.9(a). Note that it is assumed that such a finer discretisation can de defined. That is the case when the computational mesh is generated from medical data, as explained in Chapter 4.



(a) (b) (c)

Figure 2.9: Computational meshes of the third pair of intercostal arteries in the rabbit aorta. a)Fine straight-sided mesh $\bar{\mathcal{M}}$; b)coarse straight-sided mesh $\mathcal{M}$ and c)curvilinear high-order mesh.

Let $\mathbf{V_i}$ be a arbitrary vertex in $\mathcal{M}$ and $\bar{\mathbf{V}}_\mathbf{j}^\mathbf{i}$ be the n vertices in $\bar{\mathcal{M}}$ closer to $\mathbf{V^i}$. Further, let $\bar{\Omega}_j$ be n elements constructed from the vertices $\bar{\mathbf{V}}_\mathbf{j}^\mathbf{i}$ as shown in Fig. 2.10. The vertex normal $\mathbf{N_i}$ at $\mathbf{V_i}$ can now be approximated by averaging the face normals

$\bar{\mathbf{N}}_\mathbf{j}$ of the elements $\bar{\Omega}_j$. Thus

$$\mathbf{N_i} = \frac{1}{\sum_{j=1}^{n} \bar{A}_j} \sum_j \bar{\mathbf{N}}_\mathbf{j} \bar{A}_j,$$

where $\bar{A}_j$ is the face area of the element $\bar{\Omega}_j$. Note that n is arbitrary.

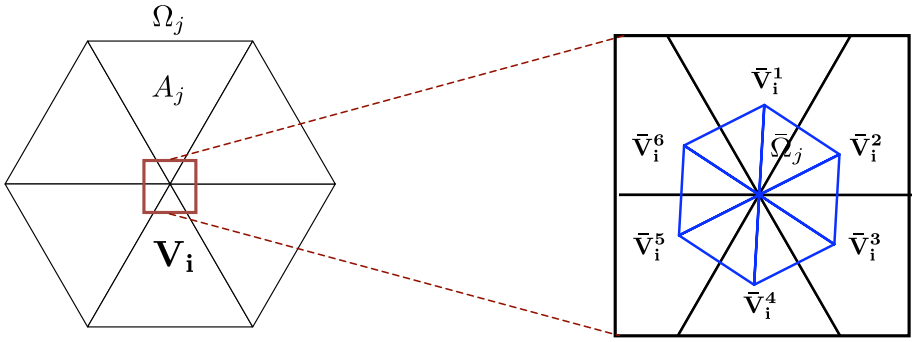


Figure 2.10: The normal $\mathbf{N_i}$ at the vertex $\mathbf{V_i}$ can be computed by area-averaging the face normals of the elements Ω_i. A better approximation is given by the area-averaging the face normals of the elements $\bar{\Omega}_j$ (blue triangles), constructed from the vertex $\bar{\mathbf{V}}_\mathbf{j}^\mathbf{i}$ of the finer straight-sided mesh $\bar{\mathcal{M}}$.

Figure 2.11 shows the curvilinear surface obtained when the vertex normals are approximated from the coarse mesh $\mathcal{M}$ (Fig. 2.11(a)), and from the auxiliary mesh $\bar{\mathcal{M}}$ (Fig. 2.11(b)). One can observe that the later surface (Fig. 2.11(b)) presents a greater geometrical accuracy and smoothness.

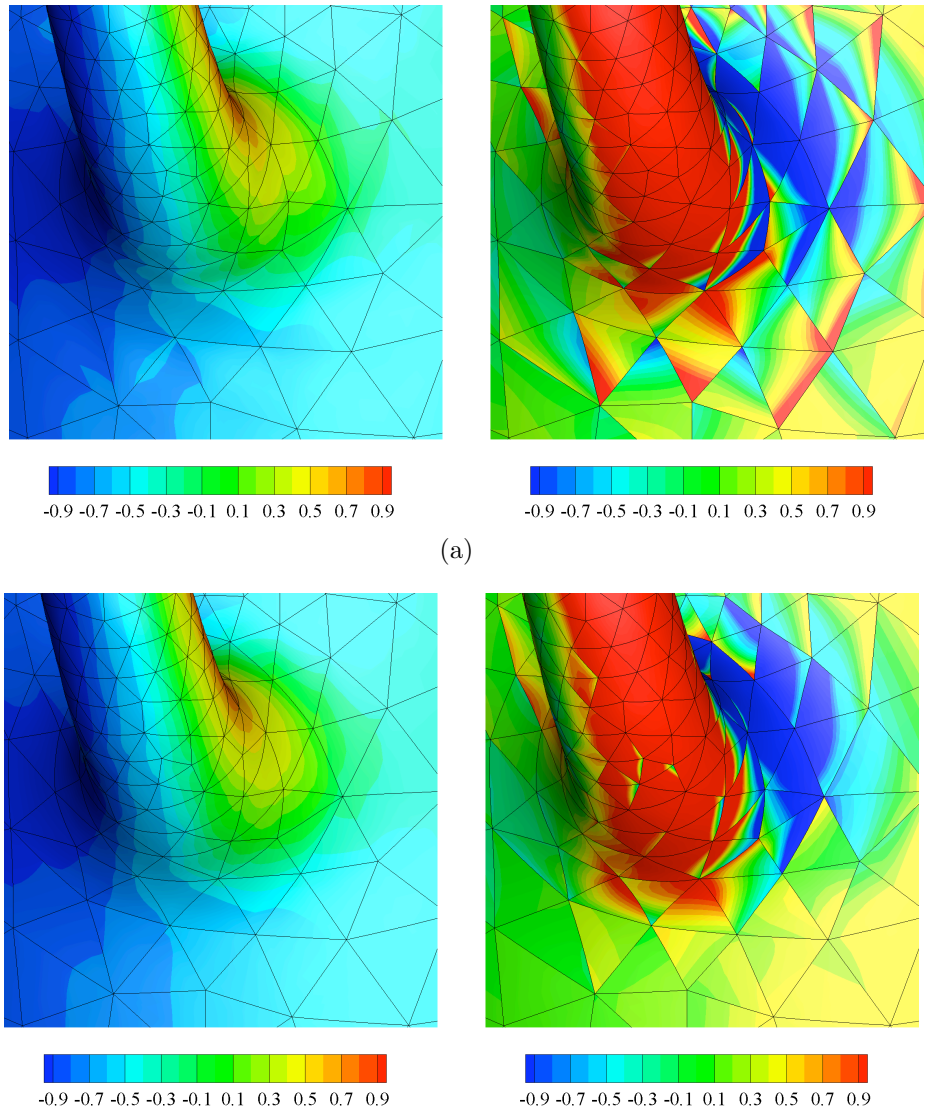


Figure 2.11: Colour map of the x-component of the surface normal *(left)* and the partial derivative of the x-component of the surface normal with respect to x *(right)*, when the vertex normals are approximated from a coarse straight-sided mesh (a), and from a fine straight-sided mesh (b). The computational meshes represent a detail of the third pair of intercostal arteries of the rabbit aorta.

Given a straight-sided mesh, the vertex normals can be estimated using one of methods described above. Such estimation along with the vertex position can be used to deform the straight-sided mesh using SPHERIGON patches, and therefore

create a curvilinear mesh as illustrated in Fig. 2.9(c).

2.3 Summary

A description of the numerical methods used in this thesis has been presented. Firstly, a basic formulation of the spectral/hp element method was described. An in-house implementation of such method (the code $N\epsilon\kappa\tau\alpha r$ [156]) was used to perform the blood flow and mass transfer simulations presented in subsequent chapters. Secondly, a review of fundamental concepts in high-order generation was given, and an algorithm to curve straight-sided meshes was proposed. Such algorithm was used to create the computational meshes in the simulations presented in Chapters 4 and 5.

Chapter 3

Nitric Oxide Transport in Flow Chambers

This chapter presents a computational study of Nitric Oxide (NO) production and transport within a parallel-plate flow chamber coated with endothelial cells. A model for endothelial NO production is developed. Further, the relationship between endothelial NO concentration (C_{NO}) and wall shear stress (WSS) is investigated in detail. This study aims to develop a more detailed understanding of the NO distribution within flow chambers, identifying key parameters that regulate NO production and transport, and illustrating the crucial role of flow on NO concentration distribution. Note that the proposed model for endothelial NO production will be also used to investigate vascular NO transport within the rabbit aorta as detailed in Chapter 5.

3.1 Introduction

Reduced bioavailability of the atheroprotective agent NO is postulated to be one of the factors that mediate the onset of atherosclerosis [86]. Evidence suggests that Endothelial Nitric Oxide Synthase (eNOS) concentration and hence NO production

strongly depend on WSS [25, 24]. This WSS-dependent NO production (possibly in conjunction with an impaired NO transport due to biological factors such as oxygen radicals) may provide an explanation for the flow-mediated onset of the disease.

Despite its relevance to atherosclerosis, the relationship between WSS and endothelial NO production remains a point of contention. NO is avidly scavenged by the haemoglobin contained in red blood cells [8], complicating direct *in vivo* measurements [70]. In order to facilitate such NO concentration measurements, numerous *in vitro* studies [46, 65] have used parallel plate flow chambers to determine the relationship between NO production and WSS in a quantitative fashion.

Despite these efforts, experimental data are scarce and often conflicting, leading to NO production rate estimations in the literature that vary over several orders of magnitude [23]. These discrepancies may be explained, in part, by an insufficient characterisation of the fluid-dynamics aspects of the experiments, such as convection. Undefined or uncontrolled flow profiles may lead to misinterpretation of experimental results. In fact, some authors [150] have suggested that reconciliation between apparently conflicting findings may be possible with a more careful review of the flow regimes within the flow chambers.

Numerous computational studies have modelled NO production and transport under *in vitro* [40] scenarios. The main goals of these models have been to determine the effective diffusion distance of NO into the culture medium. From a biological standpoint, these models are limited in two ways: 1) variations in NO production rate with WSS are not considered (NO production rate remains constant) and 2) NO transport due to convection is not modelled.

Only a small number of studies in the literature have addressed the aforementioned limitations. Kanai *et al.* [65] investigated the NO distribution in a parallel plate flow chamber coated with endothelial cells. They developed a mathematical model that included both convective and diffusive NO transport. Indirect measures of NO concentration were used (in conjunction with the numerical model) in order to estimate the endothelial NO production rate for different levels of WSS. Although

this study experimentally characterised the relationship between NO production rate and WSS (which was found to be linear in the range studied), it did not investigate the dependence of endothelial NO concentration on WSS.

To the author's knowledge, only one previous paper [40] has modelled both convective and diffusive NO transport within a parallel-plate flow chamber, paying particular attention to their effect on NO concentration. However, although this previous study considered a WSS-dependent NO production rate, this dependency is not physiologically realistic. Furthermore, other mass transport phenomena that affect NO production rate (such as a negative feedback mechanism on NO production) were not taken into account.

This chapter aims to develop a more detailed understanding of the NO distribution within flow chambers, identifying key parameters that regulate NO production and transport, and illustrating the crucial role of flow on NO concentration distribution. It is hoped that the numerical model presented here may aid accurate interpretation of experimental data.

3.1.1 Limitations of the model

The model proposed in this section presents several limitations, as it simplifies and neglects many aspects of endothelial NO production. In particular the model fails to take into account transient endothelial responses, such as a burst in NO production due to the onset of flow in the experiments [150]. Therefore, the model cannot predict NO distribution at the initial stage of the experiments (in the order of minutes), before the steady-state is reached.

Furthermore, the kinetics of the intracellular reactions that lead to NO production are not modelled. In particular, the effects of aspects such as cellular eNOS distribution or substrates availability on endothelial NO production are not considered. However, such effects are unlikely to be significant under standard experimental conditions [23]. Despite these limitations, the model provides a conceptual framework

for the analysis of NO production and transport in *in vitro* experiments. Specifically, the results of this study highlight the role of convection in NO transport, which has been neglected or misinterpreted in most previous theoretical studies.

3.2 Computational model for nitric oxide production and transport in flow chambers

This section proposes a computational model for endothelial NO production and transport in *in vitro* scenarios. In particular NO distribution within a commercial parallel plate flow chamber (Ibidi Slide VI) is modelled. The model is constructed under the following general assumptions:

- Given the geometry of the chamber ($b \gg h$, where b and h are the width and the height of the flow chamber respectively), infinite width is assumed and consequently the problem becomes bidimensional in nature.
- The culture medium is assumed to have the same dynamic viscosity as water.
- The endothelial cell monolayer is modelled as a surface source of NO. This assumption is based on the fact that the thickness of the endothelium ($\sim 5\mu$m) can be neglected *c.f.* the height of the flow chamber. Previous numerical studies [40] have shown that variations in NO concentration throughout the endothelial cells are negligible.
- A distance d is allowed between the entrance of the flow chamber and the endothelial cell monolayer, mimicking the configuration of the experimental set-up associated with this study. In such an experimental set-up, this distance prevents endothelial cells being exposed to developing flow profiles. Here, a fully developed Poiseuille flow is assumed throughout the chamber.
- It is assumed that NO concentration is zero at the entrance of the chamber *i.e* there is no NO dissolved in the culture medium.

3.2.1 Computational domain

In line with these assumptions, the computational domain is defined as shown in Fig. 3.1. The parameters of the model are summarised in Table 3.1.

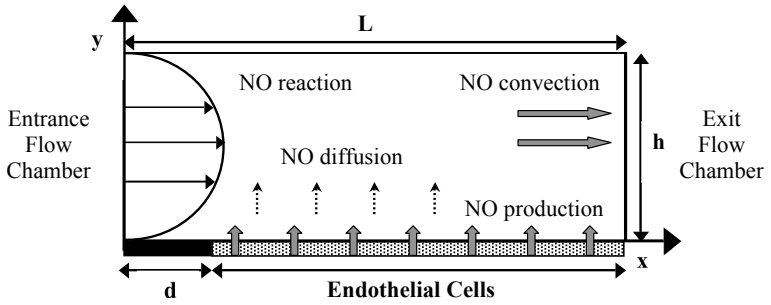


Figure 3.1: Computational domain. NO is produced by endothelial cells. It subsequently diffuses and reacts with the culture media. Finally, NO is convected out of the chamber due to the effect of flow.

3.2.2 Governing equation

NO transport is governed by the following steady Advection-Diffusion-Reaction equation

$$0 = -\vec{v} \cdot \vec{\nabla} C_{NO} + D_{NO} \nabla^2 C_{NO} - V_{NO}, \tag{3.1}$$

where C_{NO} denotes NO concentration, D_{NO} is the NO diffusion coefficient, $\vec{v}$ represents the velocity field within the domain and V_{NO} is the rate at which NO is consumed by reaction with the culture medium, which will be shown shortly to depend on C_{NO}.

3.2.3 Nitric oxide reaction with the culture medium

In aqueous solutions, NO auto-oxidises to yield nitrogen dioxide(NO_2) [56]. This reaction is expressed in the following equation:

$$2NO + O_2 \rightarrow 2NO_2.$$

The kinetics of NO auto-oxidation are assumed to be third order [78], thus

$$V_{NO} = \mathrm{k_3} C_{\mathrm{O_2}} C_{NO}^2, \tag{3.2}$$

where $C_{\mathrm{O_2}}$ is oxygen concentration in the aqueous medium and $\mathrm{k_3}$ is the third order NO auto-oxidative reaction rate. Since $C_{\mathrm{O_2}}$ is significantly larger ($C_{\mathrm{O_2}} \sim 10^{-3}$M) than C_{NO} ($C_{NO} \leq 10^{-6}$M) [65], it is assumed that oxygen concentration in the fluid remains constant throughout the experiments. Therefore, the kinetics of NO auto-oxidation given by Eq. 3.2 can be represented by the following pseudo-second order reaction

$$V_{NO} = \mathrm{k} C_{NO}^2,$$

where k is the pseudo-second order reaction rate. Table 3.1 summarises the values of all the constant parameters involved in the simulations. Note that the value of k used here is slightly larger than the one used in [40] and [153]. However, the estimated value for k in this study is in better agreement with the experimental results of Kanai *et al.* [65].

Symbol	Value, Units	Description, Reference
h	0.04 cm	Height of the flow chamber
L	1.7 cm	Length of the flow chamber
b	0.38 cm	Width of the flow chamber
d	0.2 cm	Entrance length
μ_w	$7.06 \cdot 10^{-3}$ dyn s cm^{-2}	Dynamic viscosity of the culture medium [38]
D_{NO}	$3.3 \cdot 10^{-5}$ cm^2 s^{-1}	NO diffusion coefficient [90]
$\mathrm{k_3}$	$6 \cdot 10^6$ M^{-2}s^{-1}	Third order auto-oxidative NO reaction rate [72]
k	$7.56 \cdot 10^3$ M^{-1}s^{-1}	Second order auto-oxidative NO reaction rate [65]

Table 3.1: Description of the constant parameters of the model of nitric oxide production and transport in flow chambers.

3.2.4 Nitric oxide production at endothelial cells

The NO production rate at the endothelium is a critical parameter in the computational simulation of NO transport. Despite an increasing number of experimental studies, the pathways that lead to NO production in response to WSS remain unclear and hence uncharacterised [22]. In particular, the order of magnitude of eNOS (endothelial Nitric Oxide Synthase) concentration is still a contentious point, leading to large discrepancies in the reported values of the endothelial NO production rate [23].

The model for endothelial NO production rate proposed here is constructed under the following assumptions:

1. Substrates for NO synthesis (L-arginine, oxygen, etc) are present in excess.
2. NO production rate depends linearly on intracellular eNOS concentration [23].
3. The relationship between eNOS concentration and WSS magnitude is assumed to be sigmoidal [25]. This assumption is supported by several *in vivo* studies [25, 24]. Furthermore, for a wide range of the parameter space investigated, the proposed model is also in good agreement with the results of the *in vitro* study of Kanai *et al.* [65], in which a linear relationship between NO production rate and WSS in the range 2-10 dynescm^{-2} was found.

Under the aforementioned assumptions, the NO production rate R_{NO} at the endothelium ($x \geq d$, $y = 0$) is given by

$$R_{NO}(x) = \frac{R_{NO_{\mathrm{MAX}}}}{1 + \gamma \exp(-W_{\mathrm{o}}|\tau|)}, \tag{3.3}$$

where

- $R_{NO_{\mathrm{MAX}}}$ is the maximum production rate, which corresponds to the product of the maximum intracellular eNOS concentration and the maximum catalytic velocity rate.

- τ represents WSS magnitude.
- γ and W_o are parameters that characterise the endothelial response to WSS. This nomenclature is consistent with that used in [108] and [151].

The proposed model assumes that endothelial NO production does not indefinitely increase with WSS, but instead it reaches a saturated production rate for a given value of WSS (see Fig. 3.2). *In vivo* evidence [25] supports this hypothesis, which was overlooked by previous mathematical models [40] investigating NO distribution in flow chambers.

Negative feedback mechanism

The previous model does not consider chemical reactions that take place in the endothelial cell once NO has started to be produced. In fact, endothelial NO can bind to different forms of eNOS heme [23], leading to a reduction in NO production rate. Further, NO inhibits the activation of NF-κB, a protein that may be also responsible for enhanced eNOS transcription in response to laminar WSS [55]. These reactions have been postulated to constitute a negative feedback mechanism that regulates endothelial NO production.

To the author's knowledge, this is the first study that models the effect of a negative feedback mechanism on endothelial NO production. As a first approximation such a mechanism is modelled as a linear process. Therefore, NO production rate can be described by

$$R_{NO}(x) = \frac{R_{NO_{\mathrm{MAX}}}}{1 + \gamma \exp(-W_o|\tau|)} - \beta C_{NO}(x, 0), \tag{3.4}$$

where β is a parameter that quantifies the effect of the negative feedback mechanism on endothelial NO production.

Note that this mechanism implies that the endothelial NO production rate decreases as the NO concentration at the endothelial surface increases. Given that NO concentration substantially varies within the flow chamber (as a NO concentration boundary layer develops), NO production rate also spatially varies along the flow chamber.

3.2.5 Boundary conditions

The NO concentration flux at the top plate ($y = h$) is set to be zero, thus

$$\frac{\partial C_{NO}}{\partial y}\Big|_{y=h} = 0. \tag{3.5}$$

It can be shown that the endothelial NO concentration at the endothelium ($C_{NO}(x, 0)$) asymptotes to a constant value C_{k} at some finite distance (*i.e* $C_{NO}(x, 0) \to C_{\mathrm{k}}$ for some finite x). Thus

$$\frac{\partial C_{NO}}{\partial x}\Big|_{x\to\infty} = 0.$$

Since the computational domain is finite, the previous boundary condition is applied at $x = L_\infty$ instead, where L_∞ is sufficiently downstream of the domain of interest. Hence

$$\frac{\partial C_{NO}}{\partial x}\Big|_{x=L_\infty} = 0. \tag{3.6}$$

It is also assumed that NO concentration is zero at the entrance of the chamber ($x = 0$), thus

$$C_{NO}\Big|_{x=0} = 0. \tag{3.7}$$

Finally, at the interface between the endothelial cell monolayer and the culture medium ($y = 0$) a balance between NO production and NO transport is enforced, thus

$$R_{NO} = -D_{NO}\frac{\partial C_{NO}}{\partial y}\Big|_{y=0}. \tag{3.8}$$

Non-dimensional equations

Let

$$x^* = \frac{x}{h}, \tag{3.9}$$

$$y^* = \frac{y}{h}, \tag{3.10}$$

$$\mathrm{v}^{\vec{*}} = \frac{\vec{v}}{V_{\mathrm{o}}}, \tag{3.11}$$

$$\mathrm{k}^* = \frac{\mathrm{k}h^3 R_{NO_{\mathrm{MAX}}}}{D_{NO}^2}, \tag{3.12}$$

$$C^* = \frac{C_{NO}D_{NO}}{R_{NO_{\mathrm{MAX}}}h}, \tag{3.13}$$

and

$$R^*_{NO} = \frac{R_{NO}}{R_{NO_{\mathrm{MAX}}}}, \tag{3.14}$$

where V_o is the average velocity of the parabolic flow profile.

Substituting Eqs. 3.9-3.13 into Eq. 3.1 leads to the following non-dimensional governing equation,

$$0 = -\mathrm{Pe}\ \vec{\mathrm{v}^*} \cdot \vec{\nabla} C^* + \nabla^2 C^* - \mathrm{k}^* C^{*2}, \tag{3.15}$$

where Pe is a Peclet Number defined as

$$\mathrm{Pe} = \frac{V_\mathrm{o} h}{D_{NO}}. \tag{3.16}$$

Substituting Eqs. 3.9, 3.10, 3.13 and 3.14 into the equations that describe the boundary conditions Eq. 3.5 - 3.8 leads to Eqs. 3.17 - 3.20.

$$\left.\frac{\partial C^*}{\partial y^*}\right|_{y^*=1} = 0, \tag{3.17}$$

$$\left. C^* \right|_{x^*=0} = 0, \tag{3.18}$$

$$\left.\frac{\partial C^*}{\partial x^*}\right|_{x^*=L^*} = 0, \tag{3.19}$$

$$R^*_{NO} = \left.\frac{\partial C^*}{\partial y^*}\right|_{y^*=0}, \tag{3.20}$$

with

$$R^*_{NO} = \frac{1}{1 + \gamma \exp(-W^*_\mathrm{o}\mathrm{Pe})}, \tag{3.21}$$

and

$$L^* = \frac{L}{h},$$

where

$$W^*_\mathrm{o} = \frac{\tau W_\mathrm{o}}{\mathrm{Pe}}.$$

Negative feedback mechanism

In cases where a negative feedback mechanism on endothelial NO production is taken into account, the non-dimensional NO production rate can be expressed by

$$R^*_{NO} = \frac{1}{1 + \gamma \exp(-W^*_\mathrm{o}\mathrm{Pe})} - \beta^* C^*, \tag{3.22}$$

where

$$\beta^* = \frac{\beta h}{D_{NO}}.$$

3.2.6 Velocity field

The non-dimensional velocity field is obtained analytically using a Hagen–Poiseuille parabolic profile, thus

$$\vec{v}^* = 6y^*(1 - y^*)\vec{i},$$

where $\vec{i}$ is a unit vector normal to the exit of the flow chamber.

3.2.7 Parameters

As shown in section 3.2.5, the non-dimensional NO concentration C^* depends on the three non-dimensional parameters Pe, W_o^* and γ. (Note that when a negative feedback mechanism is modelled, C^* also depends on the non-dimensional parameter β^*). Table 3.2 defines the range over which these non-dimensional parameters are varied. Note that C^* is independent of the maximum NO production rate $R_{NO_{\mathrm{MAX}}}$.

Note that some parameters have been varied over an extremely wide range. The scarce – and often conflicting – experimental data present in the literature have motivated the choice of such wide ranges.

Non-dimen. Parameter	Non-dimensional Physiological Range	Dimensional Parameters
Pe	$1000 - 15000$	$V_o = 1 - 15 cms^{-1}$, $D_{NO} = 3.3 \cdot 10^{-5} cm^2 s^{-1}$
W_o^*	$0 - \infty$	$W_o = 0 - \infty Pa^{-1}$, $D_{NO} = 3.3 \cdot 10^{-5} cm^2 s^{-1}$;
γ	$0 - 100$	$\gamma = 0 - 100$
β^*	$0 - 10^3$	$\beta = 0 - 1 cms^{-1}$, $D_{NO} = 3.3 \cdot 10^{-5} cm^2 s^{-1}$

Table 3.2: Description of the non-dimensional parameter ranges for the simulation of nitric oxide transport in flow chambers.

3.2.8 Numerical method

The concentration field is calculated using the in-house spectral/hp element method solver $Ne\kappa\tau\alpha r$ [129]. The computational mesh was refined to guarantee an accuracy of 10^{-5} for the simulations.

3.3 Results

3.3.1 Nitric oxide production rate

The dependence of the endothelial NO production rate on Pe (and hence WSS) is characterised by the non-dimensional parameters W_{o}^* and γ. In this section the physical meaning of these parameters and their effect on the non-dimensional NO production rate R_{NO}^* is described.

Effect of W_{o}^*

Fig. 3.2 shows a plot of R_{NO}^* against Pe for various values of the parameter W_{o}^* with a fixed value of γ. It can be observed that W_{o}^* characterises the sensitivity of the endothelial response to Pe. Very sensitive responses are associated with high values of W_{o}^*, while less sensitive responses are associated with low values of W_{o}^*. In the limiting cases $W_{\mathrm{o}}^* = 0$ and $W_{\mathrm{o}}^* \to \infty$, the NO production rate is constant in the studied range of the parameter space and therefore independent of Pe.

Effect of γ

It is clear from Eq. 3.22 that the value of the parameter γ characterises the basal level of NO production rate. Higher values of γ are associated with a lower basal level of NO production, while low values correspond to a high basal level of NO production.

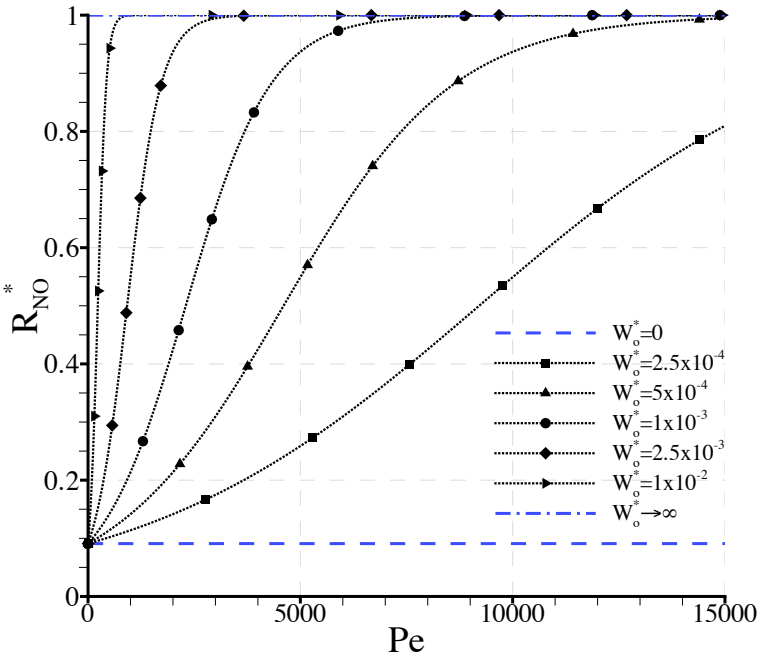
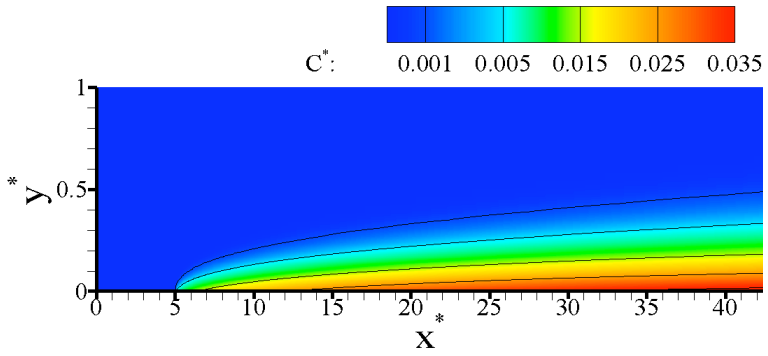


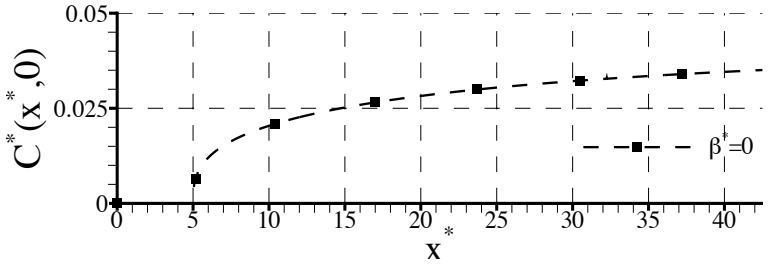
Figure 3.2: Plots of R^*_{NO} against Pe for several values of the parameter W^*_{o} with fixed $\gamma = 10$ and $\beta^* = 0$

3.3.2 Nitric oxide concentration field

The non-dimensional NO concentration field C^* depends on Pe and two additional non-dimensional parameters (W^*_{o} and γ). Fig. 3.3 shows NO distribution within the flow chamber for a given set of conditions within the parameter space (Pe = 1200, $W^*_{\mathrm{o}} = 2.5 \cdot 10^{-3}$ and $\gamma = 10$). Note that for all the cases presented in this section, the effect of the feedback mechanism is neglected (hence $\beta^* = 0$).



(a) Colourmap of C^* within the chamber



(b) Plot of C^* evaluated at $y^* = 0$

Figure 3.3: Plots of C^* distribution within the flow chamber for a given value of the parameter space (Pe = 1200, $W_o^* = 2.5 \cdot 10^{-3}$, $\gamma = 10$ and $\beta^* = 0$).

It can be observed that an NO Concentration Boundary Layer (CBL) develops within the flow chamber, leading to significant spatial variations in endothelial NO concentration. In order to investigate the relationship between endothelial NO concentration and WSS, we define the parameter C_L^* as the non-dimensional NO concentration at the point located adjacent to the endothelial cells at the exit of the flow chamber *i.e.* $C_L^* = \mathrm{C}^*(L^*, 0)$.

It can be shown that for cases where $\mathrm{k}^* > 0$, the NO concentration at the endothelial surface asymptotes to a constant value C_k^* at some finite distance (*i.e* $C^*(x^*, 0) \rightarrow C_\mathrm{k}^*$ for some finite x^*). However this distance may be greater or lesser than the length of the flow chamber. Note that for the given device studied here, the CBL is not fully developed within length of the chamber and therefore $C_L^* \neq C_\mathrm{k}^*$.

To the author's knowledge there are no published analytic solutions to the convection-diffusion-reaction equation with the boundary conditions considered in this study.

David *et al.* [32] proposed a similarity solution for ATP endothelial concentration under similar conditions as the model described here. However, this analytic solution does not consider reaction with the medium, and therefore is not applicable to this study. Another related analytic approach is given in [109] by Probstein *et al.*, where a constant wall concentration is considered.

The aim of this study is to investigate the relationship between endothelial NO concentration and WSS. Fig. 3.4 reproduces a plot of R^*_{NO} and C^*_L against Pe for a given point within the parameter space ($W^*_o = 10^{-3}$, $\gamma = 10$ and $\beta^* = 0$). It can be observed that C^*_L depends on Pe in a non-monotonic fashion (*solid line*), despite the fact that R^*_{NO} monotonically increases with Pe (*dashed line*).

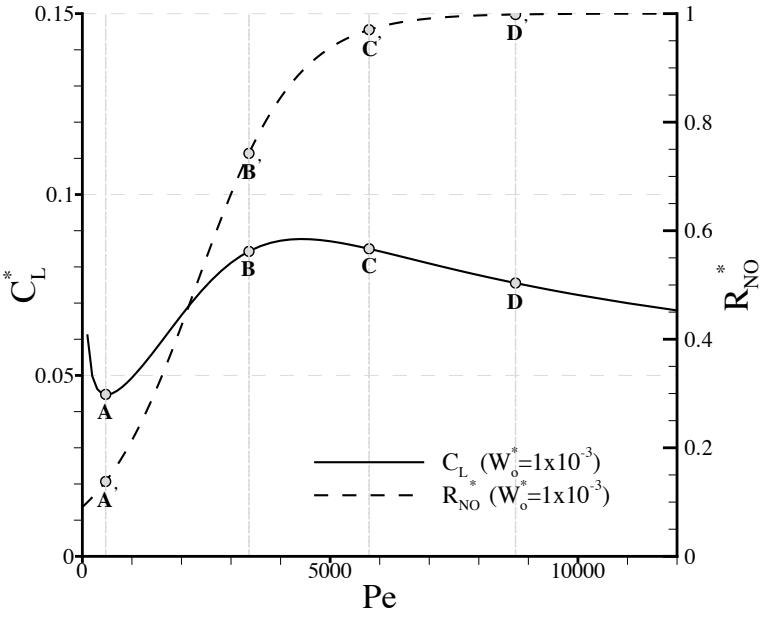


Figure 3.4: Plot of C^*_L and R^*_{NO} against Pe for given endothelial response ($W^*_o = 10^{-3}$, $\gamma = 10$ and $\beta^* = 0$).

An increase in Pe, which physically can be achieved through an increase in the flow velocity and thereby increasing the WSS, is associated with two different phenomena: 1) Increased NO production R^*_{NO} at the endothelium until it reaches a saturated level (*dashed line*), and 2) An increase in the product Pe $\vec{v}^*$ (referred to as the local Peclet number, which can be interpreted as a local scaled convective velocity when

all other quantities are fixed).

These two phenomena have opposite effects on endothelial NO concentration: an enhanced R^*_{NO} results in an increase in the endothelial NO concentration C^*_L, while an increase in the local Peclet number leads to a decrease in C^*_L, as NO is convected out of the chamber at a faster rate.

Whether C^*_L increases or decreases with Pe is determined by the balance between the two phenomena which are associated with an increase in Pe. Cases where the enhancement of R^*_{NO} outweighs the increase in the scaled convective velocity result in an increase in C^*_L (points A $\rightarrow$ B). However, cases where the increased convective velocity is larger than the increased R^*_{NO} lead to a decrease in C^*_L (points C $\rightarrow$ D).

Note that for the case illustrated in Fig. 3.4 the balance between both phenomena (increased R^*_{NO} and increased Pe $\vec{v}^*$) varies as Pe rises, leading to the non-monotonic relationship between Pe and C^*_L shown by the solid line.

Once the maximum R^*_{NO} has been reached (point D-D'), R^*_{NO} remains constant and the only effect of an increase in Pe on NO concentration field is an increase in non-dimensional scaled convective velocity. Therefore, once the NO production rate is saturated, C^*_L monotonically decreases with Pe.

It is clear from the previous discussion that the relationship between C^*_L and Pe strongly depends on the specific form of the endothelial response (in terms of NO production) to Pe. Figures 3.2 and 3.5 reproduce plots of R^*_{NO} and C^*_L against Pe for different endothelial responses (characterised by the parameter W^*_{o}).

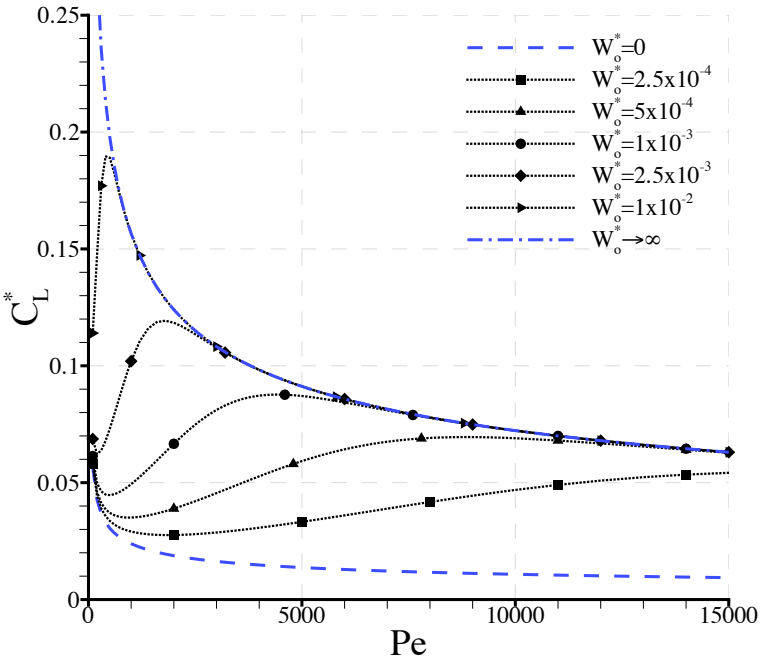


Figure 3.5: Plots of C_L^* against Pe for different values of W_o^* with fixed $\gamma = 10$ and $\beta^* = 0$.

It can be seen that C_L^* depends on Pe in a non-trivial fashion. In the limiting cases $W_o^* = 0$ (*dashed line*) and $W_o^* \to \infty$ (*dash-dotted line*), R_{NO}^* is constant and independent of Pe within the studied parameter ranges. Therefore, the only effect of increasing Pe is to increase the scaled NO convective velocity. In these cases, for a given NO production rate, C_L^* is proportional to Pe^{-1}, and therefore C_L^* monotonically decreases with Pe. Since experimental data strongly suggest a dependence of NO production rate on Pe, these cases may not be physiologically relevant, although they are conceptually important.

In the remaining cases ($W_o^* \neq 0$), an increase in Pe is associated with two different phenomena (as previously discussed): 1) Increased NO production at the endothelium and 2) Increased non-dimensional scaled convective velocity (Pe $\vec{v}^*$). Depending on the form of the endothelial response to Pe, the balance between these two phenomena may vary as Pe rises, resulting in a non-monotonic dependence of C_L^* on Pe, as shown by the *dotted lines* in Fig. 3.5. Note that for physiological realistic endothelial responses, an initial decrease of endothelial NO concentration should be expected as Pe rises.

Once the maximum non-dimensional NO production rate has been reached ($R^*_{NO} = 1$), R^*_{NO} remains constant and the NO concentration field is exclusively regulated by convection. Therefore, the value of C^*_L tends towards the solution that is obtained when $W^*_o \to \infty$.

Influence of γ

The dependence of C^*_L on the parameter γ was also investigated. It was found that although γ had a significant quantitative impact on the results, it did not affect the NO distribution structure within the flow chamber. Cases where γ was modified were associated with a vertical expansion/stretching of the curves $C^*_L = f(Pe)$ (data not shown).

3.3.3 Negative feedback mechanism

This section analyses the effect of a negative feedback mechanism on the non-dimensional NO concentration C^*. Fig. 3.6 compares the endothelial NO distribution $C^*(x^*, 0)$ within the flow chamber for cases where the feedback mechanism is neglected ($\beta^* = 0$) and cases where the feedback mechanism is considered ($\beta^* \neq 0$).

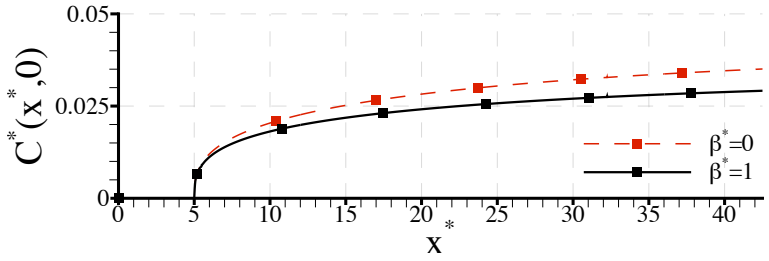


Figure 3.6: Plot of $C^*(x^*, 0)$ for cases where $\beta^* = 0$ *(dashed line)* and $\beta^* = 1$ *(solid line)*, with a fixed value of the parameter space (Pe = 1200, $W^*_o = 2.5 \cdot 10^{-3}$ and $\gamma = 10$).

It can be observed that the negative feedback mechanism modifies the growth rate of the NO CBL. Discrepancies in the thickness of such a CBL between both cases ($\beta^* = 0$ and $\beta^* \neq 0$) are maximum towards the exit of the chamber. Such discrepancies become more significant as the parameter β^* rises (data not shown).

Figure 3.7 shows the relationship between C_L^* and Pe for cases where $\beta^* = 1$. A decrease in C_L^* *c.f.* cases where $\beta^* = 0$ (grey dash and dash-dot lines) can be observed. The existence of a negative feedback mechanism leads to a decreased NO production rate, resulting in a decrease in the overall NO concentration within the chamber. This decrease is more significant as the parameter β^* rises (data not shown).

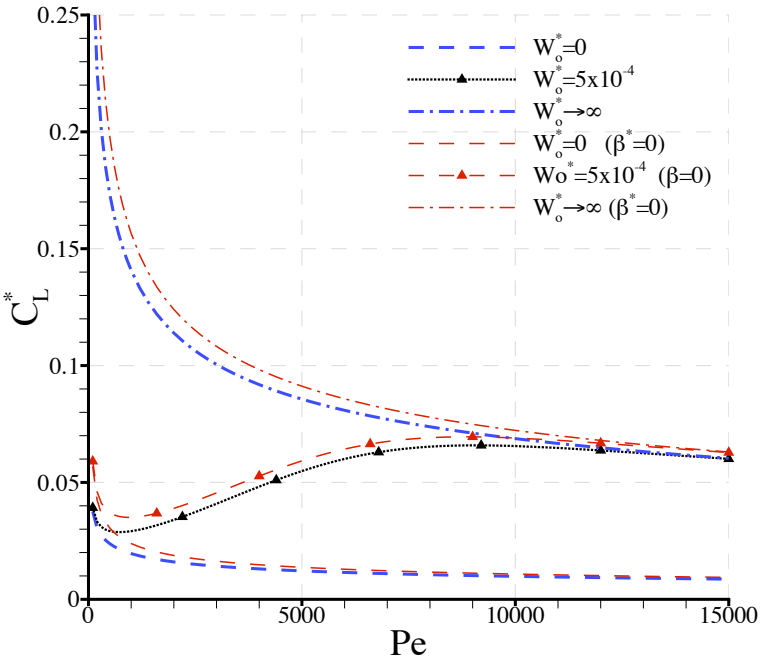


Figure 3.7: Plots of C_L^* against Pe for different values of W_o^* with fixed with fixed $\gamma = 10$ and $\beta^* = 1$.

3.3.4 Dimensional results

Despite the great number of experimental studies, endothelial NO production rate estimations in the literature vary over several order of magnitudes [23]. Furthermore, neither the sensitivity of the endothelial response to WSS nor the maximum increase of NO production rate with WSS have been experimentally determined.

Given the lack of consistent experimental data, the results presented in this section should be cautiously interpreted. The dimensional NO concentration results have been obtained under the following assumptions:

- The maximum NO production rate is assumed to be $R_{NO_{\mathrm{MAX}}} = 8.33 \cdot 10^{-4} \mu$M cm s^{-1}. This value is within the range of NO production estimations in the literature [23] and leads to a characteristic concentration $C_o = 1$ μM ($C_o = \frac{hR_{NO_{\mathrm{MAX}}}}{D_{NO}}$) that is consistent with previous computational studies [144].
- The maximum NO production rate is assumed to be 11-fold higher than the basal NO production rate (*i.e.* $\gamma = 10$).
- Different endothelial responses to WSS (characterised by the parameter W_{o}^*) are analysed.

Figure 3.8 reproduce plots of endothelial NO concentration at the exit of the flow chamber (C_L) against WSS for different endothelial responses (characterised by the parameter W_{o}^*).

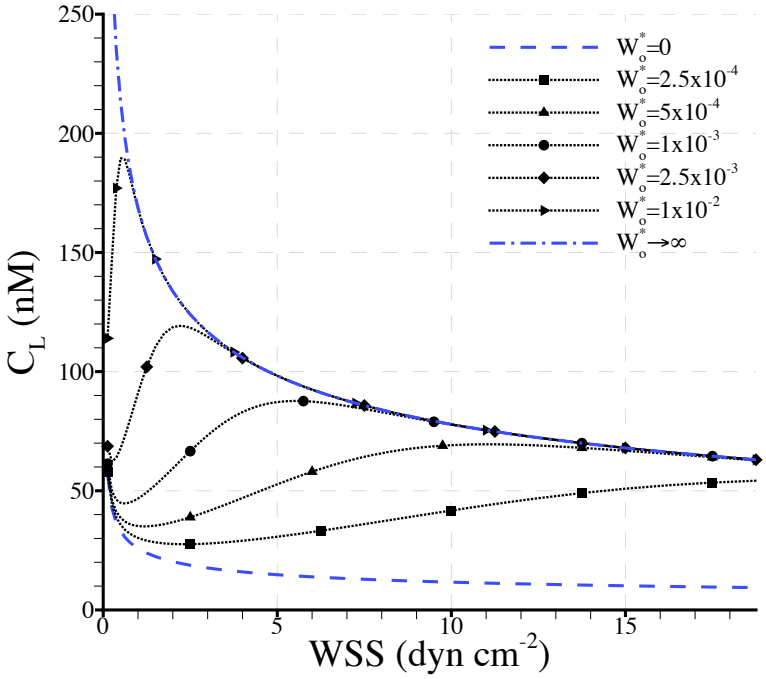


Figure 3.8: Plots of C_L (nM) against WSS (dynes cm^{-2}) for different values of W_{o}^* with fixed with fixed $\gamma = 10$ and $\beta^* = 0$.

Under the aforementioned assumptions, NO concentration at the endothelial surface is of the order of nM ($C_L \in$ [0-250]nM). These results are in good agreement with

the results from Fadel *et al.* [40]. However, such study differs from ours in many fundamental points: (Note that most discrepancies between both models are due to the large variations in reported experimental data)

- The reaction rate considered in this study is larger than the one used in [40].
- The maximum NO production rate considered here is significantly larger than the one used in [40].
- In this study the maximum NO production rate is assumed to be 11-fold higher than the basal NO production rate, while Fadel *et al.* consider larger increases in NO production (up to 20-fold).
- The height of the flow chamber considered here is approximately half of the one modelled in [40].

Given the large differences between both models, the good agreement between the results presented here and in [40] should be carefully interpreted, as it may lead to misleading conclusions. Further experimental characterisation of endothelial NO production and its relationship with WSS is necessary in order to accurately predict NO concentration.

3.4 Discussion

In this study NO distribution within a commonly-used commercial flow chamber [155] is investigated. The results obtained here are hence specific to the geometry of the flow chamber studied. However, it is expected that similar results will be observed for other flow chamber geometries. Therefore, the following discussion is likely to be applicable to a wide range of commercial flow chambers.

3.4.1 Nitric oxide concentration boundary layer

It is found that a NO concentration boundary layer (CBL) develops within the flow chamber. The thickness of such a CBL asymptotes to a constant value at some finite distance, which may be greater or lesser than the length of the chamber.

The formation of an NO CBL has important implications for associated experimental studies. In cases where the CBL is not fully developed (such as those investigated here), special attention should be paid to the spatial resolution of NO measurement techniques [97] used in the experiments, as there may be significant spatial variations in NO concentration within the flow chambers.

NO is known to trigger a number of endothelial responses, such as the activation of various transcription factors. Spatial variations in NO concentration within the chamber may therefore also lead to spatially heterogeneous biological responses. If such spatial variations in the endothelial response are neglected and local measurements are extrapolated to the whole chamber, the resulting conclusions may not be accurate.

Furthermore, the existence of a NO CBL could potentially be used to decouple mass transfer effects from fluid-dynamics effects in experiments. The formation of a NO CLB leads to substantial differences between the entrance and the exit of the flow chamber:

- **Entrance of the flow chamber.** The effect of mass transfer related phenomena (such as the negative feedback mechanism on NO production) is minimum in this area and can be neglected. Cells located at the beginning of the cell monolayer are only affected by fluid-dynamic phenomena. Therefore, a precise characterisation of such fluid related effects (such as activation of NO production by WSS) on endothelial responses may be possible by investigating cells situated in this area.

- **Exit of the flow chamber.** Both fluid-dynamic and mass transfer related

phenomena affect the endothelial cells located towards the end of the device, allowing the study of the combined effect of both phenomena on the endothelial response.

Note that the previous discussion is only applicable once the transient effects have passed (since the onset of the flow can trigger a burst in NO production).

3.4.2 Nitric oxide concentration at the endothelium

Endothelial NO concentration has been extensively investigated for a wide range of relationships between NO production and WSS. As WSS rises, so too does NO production rate. However, an increase in WSS is also associated with an increase in the velocity at which NO is convected out of the chamber. The balance between enhanced NO production and increased convective velocity may vary as WSS rises, resulting in a non-monotonic dependence of endothelial NO concentration on WSS.

These results are at variance with the conclusions from a previous study by Fadel *et al.* [40]. Our conclusions differ from theirs in two ways: 1) Fadel *et al.* reported a simpler biphasic relationship between endothelial NO concentration and WSS, with no maximums in endothelial NO concentration and 2) this non-monotonic relationship was found only in cases where a linear relationship between NO production and WSS was considered.

The first discrepancy is clearly due to the fact that endothelial NO production does not indefinitely increase with WSS. Instead, it reaches a saturated production rate for a given value of WSS, as *in vivo* evidence [25] suggests. Once the saturated production level has been reached, NO concentration at the endothelial surface decreases with increasing WSS, leading to a maximum in the endothelial NO concentration that has not been previously reported.

Regarding the second point of disagreement, a non-monotonic relationship between endothelial NO concentration and WSS is found in this study (in which a non-linear

relationship between NO production and WSS is considered). Based on the results presented, we hypothesise that the initial non-monotonic behaviour (before reaching the saturated level) depends on the sensitivity of the endothelial response to WSS rather than its linearity.

Figures 3.2 and 3.5 show that for physiological realistic endothelial responses, an initial decrease of endothelial NO concentration should be expected as WSS rises. Therefore, results from experimental studies [158, 110] using measurement techniques that cannot register decreases in NO concentration (such as NO detection by diaminofluoresceins (DAF) [98]) should be carefully interpreted.

3.4.3 Effect of convection on NO concentration

It has already been stated that an increase in WSS is associated with an increase in NO convective velocity. However it is important to note that such an increase in NO convective velocity does not necessary imply an increase in NO bulk convection out of the chamber, since the NO concentration distribution also varies with WSS.

In steady state, the NO convected out of the chamber balances NO produced by the endothelial cells (since NO transported out of the chamber by diffusion is negligible). Therefore, the increase in NO bulk convection with Pe is caused by the increase in NO production with Pe, and not by the increase in Pe *per se*.

The effect of convection on NO concentration has been misinterpreted in previous studies. Variations in NO concentration with WSS are not due to an imbalance between increased NO production and increased NO convection out of the chamber, as suggested in [40] . The NO concentration distribution changes with WSS to ensure a balance between NO production at the endothelial cells and NO bulk convection out of the chamber.

3.4.4 Negative feedback mechanism

The effect of a negative feedback mechanism has been assessed. Such a mechanism leads to a decrease in NO production rate proportional to the NO concentration at the endothelium. Since NO concentration is not constant along the chamber, NO production rate also varies spatially within the device. This mechanism acts to autoregulate endothelial NO concentration, resulting in a more uniform NO distribution within the chamber.

To the author's knowledge, the magnitude and time-scale of the feedback mechanism that affects endothelial NO production has not been experimentally characterised. As described in the Methods section, diverse reactions (with characteristic times between seconds [23] and hours [55]) may be responsible for the existence of such a feedback mechanism.

In this study it is observed that the effect of this mechanism on endothelial NO concentration is not spatially homogeneous within the chamber (Fig. 3.6): such an effect is minimum at the beginning of the cell monolayer and maximum towards the exit of the flow chamber. Therefore, experiments studying NO concentration variations with time in the exit region could potentially help elucidate the nature of the negative feedback mechanism.

3.4.5 Experimental studies

Further experimental work is encouraged in order to determine the relationship between endothelial NO production and WSS and hence the parameters of the model presented in this study.

The following experimental aspects should be considered: 1)ramped flow profiles should be used in order to minimise the effect of transient endothelial responses [46], 2)given the formation of a NO CBL, the measurement technique used should provide information of NO concentration in different locations along the flow chamber. (This

can be achieved by using various sensors along the chamber or NO detention by diaminofluoresceins, for example) and 3) NO concentration at a given location within the chamber should be studied over time to ensure that the steady state is reached.

3.5 Summary

The distribution of NO within a flow chamber seeded with endothelial cells has been investigated numerically. It is found that a NO concentration boundary layer develops within the chamber, leading to substantial spatial variations in NO concentration along the length of the chamber. The structure of such a boundary layer depends strongly on the relationship between NO production at the endothelium and WSS. However, this relationship remains quantitatively uncharacterised. The results presented in this study provide renewed motivation for further experimental work.

Special attention is paid to the relationship between endothelial NO concentration and WSS. An increase in WSS is associated with two different phenomena: increased NO production by the endothelial cells, and an increase in the velocity at which NO is convected out of the chamber. These two phenomena have opposite effects on NO concentration. In physiologically realistic cases, the balance between both phenomena is found to vary as WSS rises, resulting in a complex non-monotonic dependence of endothelial NO concentration on WSS. These results illustrate the key role of convective transport on NO distribution, and suggest that models exclusively considering diffusive transport may not accurately predict NO concentration.

Finally, the influence of a negative feedback mechanism on NO production is also investigated. This mechanism leads to a decrease of the NO production rate proportional to endothelial NO concentration, acting to autoregulate NO concentration within the chamber. Additional experimental work is encouraged in order to determine the magnitude of this mechanism. It is hoped that this study provides a theoretical framework to aid accurate interpretation of related experimental studies.

Chapter 4

Blood Flow in the Rabbit Aorta

This chapter presents a computational study of blood flow within a realistic representation of the rabbit aorta and its branches. Various flow features and various flow metrics (such as wall shear stress (WSS)) are analysed, along with their possible relevance to the spatially varying onset of atherosclerosis. This study aims to contribute to an enhanced understanding of blood flow dynamics and hence the flow-dependent mechanisms that trigger atherogenesis. Further, the computed flow field (along with the model of endothelial nitric oxide (NO) production proposed in Chapter 3) is used in Chapter 5 in order to investigate vascular NO transport within the same computational representation of the rabbit aorta.

4.1 Introduction

Atherosclerosis is known to occur in a spatially non-uniform fashion within the arterial system, with plaques preferentially developing in areas of high curvature and arterial branching. The current understanding of the disease postulates that atherogenesis may be driven by flow-dependent mechanisms. In particular, the patchy nature of the disease is thought to reflect spatial variation in the stresses exerted on the arterial wall by the flow of blood.

A great number of computational studies have attempted to correlate areas of disease prevalence in the vasculature with various flow metrics such as WSS [106, 107, 58]. However the computational geometry used in these studies often lack detail and accuracy. Flow metrics (in particular WSS [95]) have been shown to depend strongly on subject-specific geometrical features. Therefore, generating a detailed and faithful computational definition of the vascular geometry is necessary in order to accurately model blood flow within the arterial system.

Only a few computational studies have investigated blood flow in physiologically realistic representations of the arterial tree in mice [138, 42] and humans [83, 127]. (for further details refer to section 1.5 and [140]). To the authors knowledge, no previous studies have modelled blood flow in a realistic representation of the rabbit thoracic aorta and its branches. In the present study, the arterial geometry was obtained from high resolution CT scan data of a vascular corrosion cast of a male New Zealand White rabbit. The computational domain comprises the ascending aorta, aortic arch and proximal descending thoracic aorta. In terms of combined detail and extent, the computational geometry in this study represents a significant advance from previous studies.

4.1.1 Limitations of the model

In the present study several aspects of the rabbit haemodynamics are simplified. In particular blood is assumed to be a Newtonian fluid, blood flow dynamics are assumed to be quasi-steady, and the arterial wall is assumed to be rigid and stationary.

However, despite these limitations, the model provides insight into the underlying (and likely dominant) fluid dynamics within the rabbit aorta. Future studies should attempt to overcome the present limitations, and hence to include more complex physics such as pulsatile flow and compliant walls.

4.2 Methods

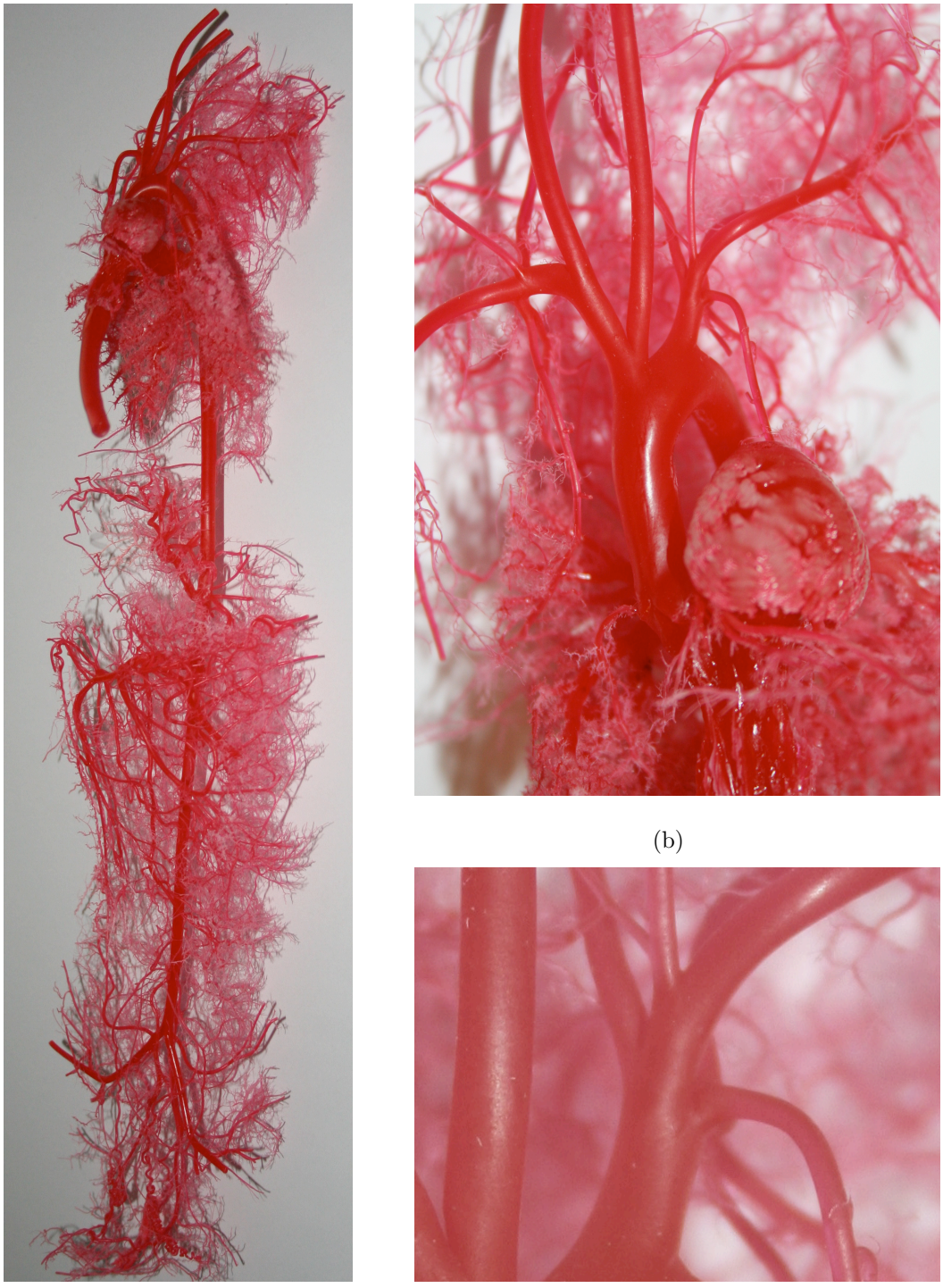
4.2.1 Reconstruction of the vascular geometry

4.2.1.1 Obtaining the vascular corrosion cast

The vascular corrosion cast was made by Mr. Anthony Hunt (Department of Bioengineering, Imperial College London). All experimental protocols were approved by Imperial Colleges Ethical Review Process Committee, in accordance with the UK Animals Act 1986.

A male New Zealand White rabbit aged 18 months and weighing 3.25 kg was administered heparin (2000 USP units, iv) and subsequently was euthanised with an intravenous overdose of sodium pentobarbitone (Euthatal, 160 mg/kg). A cannula was placed and secured into the cardiac left ventricle, via which physiological saline was then infused to flush through the arterial system.

The casting procedure was performed in accordance with the manufactures Technical Data Sheet 105 (Polysciences, Inc). The casting material (Batsons No 17, Polysciences, Inc.) was injected at a pressure of 95-100 mmHg until the resin hardened and no more resin could be infused (70 ml casting material was injected). Throughout the injection process the rabbit chest and abdominal cavities were cooled with water. The casting resin was allowed to set overnight. The following morning the specimen was entirely submerged in a potassium hydroxide corrosion bath (approximately 30% w/v). After two weeks the corrosive solution was renewed, and corrosion was allowed for further 24 hours. The second potassium hydroxide solution was then replaced by a solution of DECON detergent for another 24 hours. Finally the vascular cast was rinsed gently with warm water to remove tissue remnants, and then air dried. The resulting vascular cast is shown in Fig. 4.1.



(a) (b) (c)

Figure 4.1: Images of the vascular corrosion cast showing: (a) the entire resin cast prepared for the CT scanner (the anterior and posterior legs have been removed, as well as the head and the kidneys), (b) the aortic arch and emanating branches and (c) an enlargement of a quadfurcation of the left subclavian artery.

4.2.1.2 Scanning the vascular corrosion cast

The vascular corrosion cast was scanned by Dr. Richie Abel and Dr. Stig Walsh at the Natural History Museum (London, UK), using a Metris X-Tek HMX-ST micro-CT with a voxel size of 55.2 μM. Approximately 2000 DICOM images (9.2 GB) were obtained. There are over 100 voxels across the 6mm diameter of the aortic root.

4.2.1.3 Obtaining a surface definition

The protocol detailed in this section for the reconstruction of vascular geometries from CT scan data sets was designed by Dr. Peter Vincent (Department of Aeronautics, Imperial College London).

An intensity isosurface was segmented from the micro-CT scan data using Amira (Visage Imaging, Inc.). Further processing was carried out using the open-source software VMTK (www.vmtk.org). Firstly the surface was cropped in order to remove unwanted arteries and bound the computational domain. Further, flow extensions were extruded from each outflow vessel. Such extensions allow the imposition of boundary conditions sufficiently far from the domain of interest. Finally, the surface was smoothed to remove any artefacts introduced during the scan and segmentation process. The smoothing procedure was limited such that small-scale geometrical features were preserved.

The final surface comprises the ascending aorta, aortic arch and proximal descending thoracic aorta. Vessels emanating from the aortic arch (followed to at least their second branching generation) and five pairs of intercostal arteries are also included. In terms of combined detail and extent, the geometry represents a significant advance over previous studies. Figure 4.2 shows images of the surface definition subsequently used to create the computational mesh.

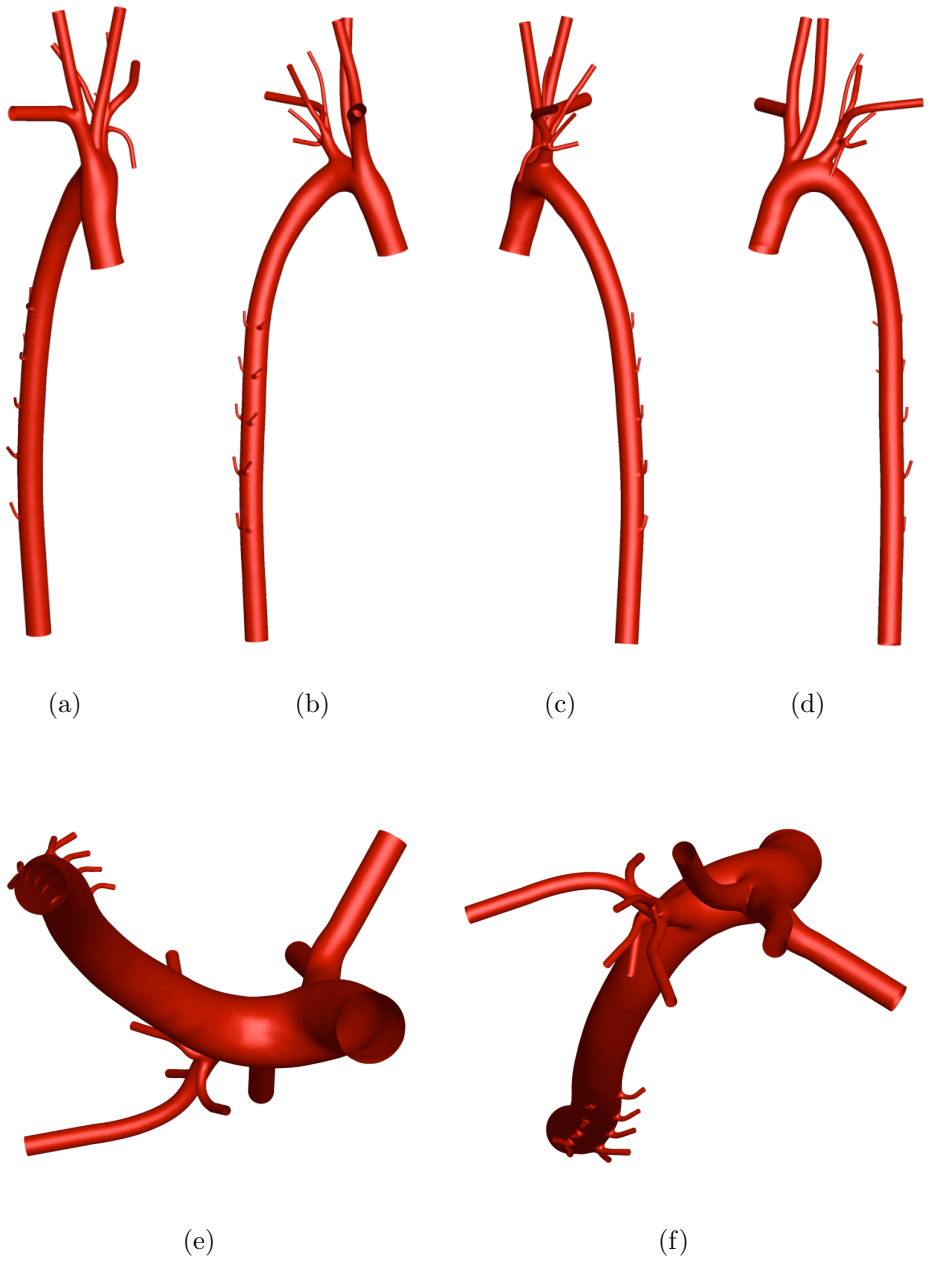


Figure 4.2: The reconstructed aortic geometry (including flow extensions) viewed right-left (a), dorsal-ventral (b), left-right (c), ventral-dorsal (d), posterior-anterior (e) and anterior-posterior (f). Note that vessels emanating from the aortic arch (followed to at least their second branching generation) and five pairs of intercostal arteries are included.

4.2.2 Obtaining a volume mesh

An initial surface triangulation was constructed with Gambit 2.4.6 (ANSYS, Inc). The size of the elements was based on the curvature of the surface definition, such that smaller elements were position in areas of greater curvature. The volume mesh was generated with Tgrid 4.0.24 (ANSYS, Inc). A prismatic boundary layer of variable thickness (based on the curvature) was defined first. An interior mesh of linear tetrahedral elements was then generated. Subsequently, the external faces of the prismatic boundary elements were curved using SPHERIGON patches [147] as described in Chapter 2. The resulting volume mesh shown in Figure 4.3 contains 25,498 prismatic and 79,847 tetrahedral elements (thus 105,345 elements in total).

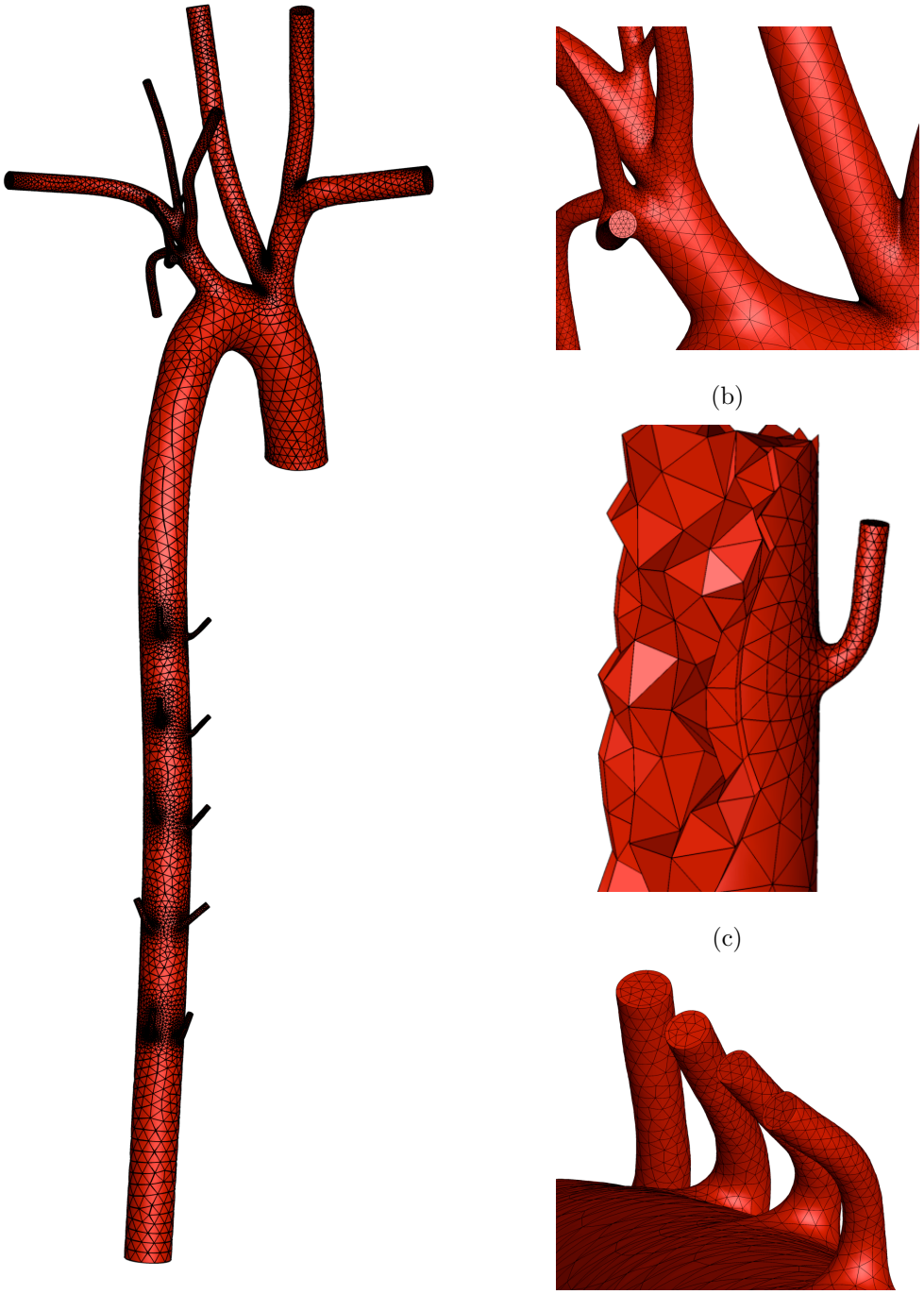


Figure 4.3: Images of the high-order curved volume mesh showing the whole computational mesh (a), an enlargement of the mesh at the quadfurcation of the left subclavian artery (b), an axial section of the descending aorta (c) and four intercostal arteries (d). The computational mesh contains 105,345 conforming prismatic and linear tetrahedral elements. Note that smaller elements have been positioned in regions of high curvature.

4.2.3 Blood flow model

Blood flow was investigated in the representation of the rabbit aorta presented in section 4.2.2. The following general assumptions were made:

- Blood was assumed to be an Newtonian fluid.
- Blood flow dynamics were assumed to be quasi-steady. A Womersley number (which is the ratio of the pulsatile inertial forces to the viscous forces) can be defined as
$$\alpha = \frac{D_0}{2}\left(\frac{\omega\rho}{\mu}\right)^{\frac{1}{2}},$$
where D_0 is the hydraulic diameter of the aortic root inflow plane, ω is the cardiac cycle frequency, ρ is the blood density and μ is the blood dynamic viscosity. For the case considered in this study, the Womersley number is estimated to be $\alpha \approx 7$, corresponding to a cardiac cycle frequency of 180bpm [7]. Therefore the inertial and viscous forces are of the same order of magnitude, and hence the effect of pulsatility on blood flow should be investigated further.
- The arterial wall was assumed to be rigid and stationary.
- The velocity profile at the inflow plane was assumed to be uniform.
- It was assumed that the flow split ratios between the aorta and its branches were dictated by Murray's Law [94], except where experimental measurements were available.

4.2.3.1 Governing equation

In line with the previous assumptions, blood flow was modelled using the steady-state incompressible Navier-Stokes equations for a Newtonian flow. Thus

$$\nabla \cdot \mathbf{u} = 0, \tag{4.1}$$

and

$$\rho \mathbf{u} \cdot \nabla \mathbf{u} = -\nabla p + \mu \nabla^2 \mathbf{u}, \tag{4.2}$$

where $\mathbf{u}$ represents the velocity vector and p denotes the pressure field.

4.2.3.2 Boundary conditions

Inflow boundary condition

The velocity profile at the aortic root was assumed to be uniform and perpendicular to the inflow plane.

Outflow boundary conditions

Vessels emanating from the aortic arch

Based on in-vivo measurements [9], the flow entering the innominate and the left subclavian artery were specified to be 14.7% and 7.1% of the inlet flow respectively. The flow distribution in the branches emanating from these major vessels (the innominate and the left subclavian artery) was prescribed in accordance with Murray's law [94].

Intercostal arteries

To the author's knowledge the flow split ratios between the aorta and the intercostal arteries have not been experimentally characterised. In this study it was estimated that 2% of the thoracic aortic flow (corresponding to 1.564% of aortic root flow) enters the first 5 pairs of intercostal arteries. Such estimation lies within the range investigated by Kazakidi *et al.* [68]. The flow rate at each intercostal artery was calculated following Murray's law.

Distal aortic outlet

A zero velocity gradient condition was imposed perpendicular to the outflow plane.

Wall boundary condition

A non-slip boundary condition was applied at the rigid wall.

4.2.3.3 Parameters

Reynolds number

The flow simulations are characterised by the Reynolds number (Re) defined as

$$Re = \frac{\rho U_0 D_0}{\mu},$$

where U_0 is the average inflow velocity magnitude at the aortic root. In this study constant values of $\rho = 1.044\text{gcm}^{-3}$ [71], $\mu = 4.043$ x $10^{-2}\text{gcm}^{-1}\text{s}^{-1}$ [152] and $D_0 =$ 5.838 x 10^{-1}cm (measured from the computational geometry) are assumed.

The numerical values for inflow velocity U_0 were chosen based on the in-vivo experimental study of Avolio *et al.* [7]. This study measured the average flow rate in the ascending aorta in the rabbit to be 3.3mls^{-1}. Flow measurements were performed using a 5mm diameter electromagnetic transducer, causing "*minimal constriction*" of the vessel. Considering that the wall thickness is 7% of the vessel diameter [21], it can be assumed that the internal aortic root diameter was 4.3mm on average in the experiments of Avolio *et al.*, leading to an average inflow area of $\sim 15\text{mm}^2$. This average inflow area, along with the averaged measured inflow rate of 3.3mls^{-1}, corresponds to an average inflow velocity of 22cms^{-1}. The average peak inflow velocity in the rabbit was also measured by Avolio *et al.* to be 92.7cms^{-1}.

In the present study blood flow was computed for three Reynolds numbers (Re = 50, Re = 300 and Re = 1300) corresponding to a low ($U_0 = 3.32\text{cms}^{-1}$), average ($U_0 = 19.9\text{cms}^{-1}$) and peak ($U_0 = 86.2\text{cms}^{-1}$) inflow aortic velocity respectively. Note that the numerical values for the average and peak inflow velocities are approximated, in order to yield round Reynolds numbers, and that the low inflow velocity is arbitrary.

Table 4.1 summarises the constant parameters of the model, and Table 4.2 shows the choice for the inflow velocity values and shows the associated Reynolds numbers.

Symbol	Value, Units	Description, Reference
ρ	1.044 gcm^{-3}	Density of blood in rabbits [71]
μ	0.04043 gcm^{-1} s^{-1}	Dynamic viscosity of blood in rabbits [152]
D_0	0.5838 cm	Aortic root diameter

Table 4.1: Description of the constant parameters used in the blood flow simulations within the rabbit aorta

Re	U_0	Description	Experimental value
50	3.32 cms^{-1}	Low aortic inflow velocity	– (arbitrary)
300	19.9 cms^{-1}	Average aortic inflow velocity	22 cms^{-1} [7]
1300	86.2 cms^{-1}	Peak aortic inflow velocity	92.7 cms^{-1} [7]

Table 4.2: Description of the inflow aortic velocities used in the blood flow simulations within the rabbit aorta

Dean number

The influence of the aortic curvature on blood flow can be characterised by the Dean number (De) defined as

$$De = Re\left(\frac{D_0}{2R_c}\right)^{\frac{1}{2}},$$

where R_c is the radius of curvature of the aortic arch. For the arterial geometry considered in this study $R_c \approx D_0$ and thus $De \approx 0.707Re$. Therefore the three Reynolds numbers investigated (Re = 50, Re = 300 and Re = 1300) correspond to Dean numbers of De = 35, De = 210 and De = 920 respectively.

4.2.4 Numerical method

Blood flow was calculated using the in-house spectral/hp element method solver $Nεκταr$ [129] as described in Chapter 2. An expansion basis of 5^{th} order was used to represent the solution within each element. Such an expansion corresponds to

504 and 224 degrees of freedom per prismatic and tetrahedral element respectively, leading to $\sim$ 3.07 x 10^7 degrees of freedom in total.

Convergence was verified by performing simulations with Re = 300 using 3^{rd}, 5^{th} and 7^{th} order expansions, corresponding to $\sim$ 1.05 x 10^7, $\sim$ 3.07 x 10^7 and $\sim$ 6.77 x 10^7 total degrees of freedom respectively. It was found that the total force varied by 0.019% when going from the 3^{rd} to the 5^{th} order expansions; and 0.004% when going from the 5^{th} to the 7^{th} order expansions. Thus, it was assumed that the solution had converged when using a 5th order expansion.

4.3 Results

This section presents an analysis of the computed blood flow within the aortic arch (section 4.3.1), the descending thoracic aorta (section 4.3.2) and the intercostal arteries (section 4.3.3). Blood flow in the vessels emanating from the aortic arch will be investigated in future studies.

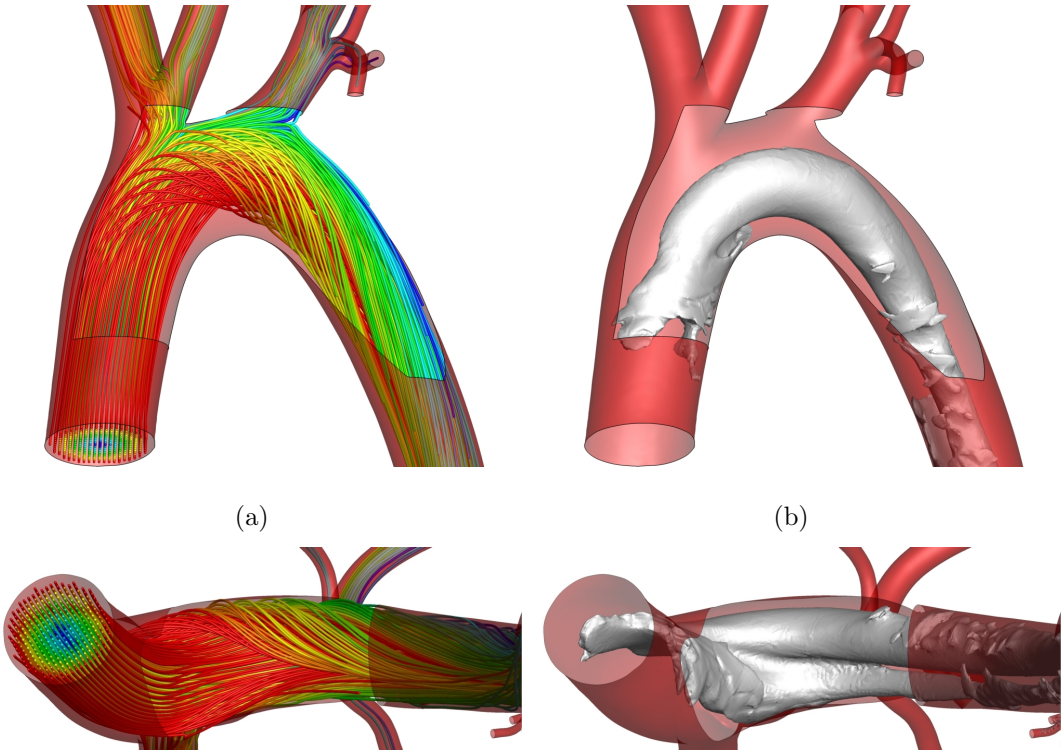
Results are presented for the three Reynolds number (Re = 50, Re = 300 and Re = 1300). Various flow features and flow metrics are analysed. Coherent vortical structures are characterised via computation of the metric λ_2. This metric is widely used and has been shown to accurately identify vortex cores for low Reynolds numbers, unlike minimum-pressure criteria (for further details see [61]). The blood streamlines are computed following the approach proposed by Coppola *et al.* [28]. The distributions of various flow metrics (such as WSS) are discussed, along with their possible relevance to the spatially varying onset of atherosclerosis. In particular, the computed WSS distribution is compared with lesions patterns when experimental data were available. The results of this computational study are discussed within the context of previous studies.

4.3.1 Blood flow in the aortic arch

Figure 4.4 shows blood flow streamlines and coherent vortical structures within the aortic arch for the average inflow velocity (Re = 300). It can be observed that the blunt inflow profile rapidly evolves into a highly complex flow. The aortic arch curvature induces a centripetal acceleration (translated to a radial pressure gradient) towards the inner wall. Such a radial pressure gradient leads to the formation of two Dean-type vortices [34] and hence the establishment of secondary flow. These Dean vortices are found to be unequal in strength, inducing asymmetrical flow patterns.

The axial velocity is affected by both the secondary motion and the centripetal acceleration caused by the aortic curvature. Further, other geometrical features such as the aortic torsion and tapering act to further increase the complexity of blood flow, leading to highly heterogeneous flow patterns within the aortic arch.

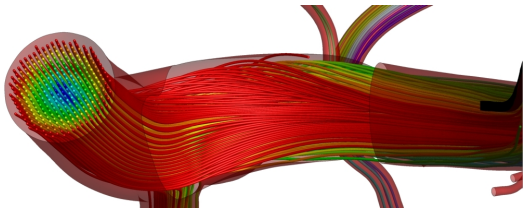
Blood flow is found to depend significantly on Re, as shown in Fig. 4.5. In particular, an increase in Re is associate with increased vortical strength and therefore enhanced secondary flow. Such blood flow variations with Re are reflected in the spatial WSS distribution, as subsequently discussed.



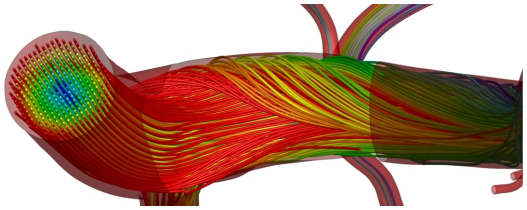
(a) (b)

(c) (d)

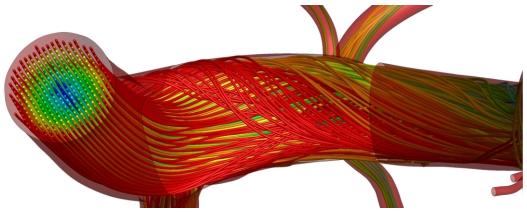
Figure 4.4: Blood flow streamlines in the aortic arch for Re = 300 viewed ventral-dorsal (a) and posterior-anterior (c). Vortical structures characterised by a λ_2 isosurface ($\lambda_2 = -0.5$) also viewed ventral-dorsal (b) and posterior anterior (d).



(a)



(b)



(c)

Figure 4.5: Blood flow streamlines viewed posterior-anterior for Re = 50 (a), Re = 300 (b) and Re = 1300 (c).

Wall Shear Stress in the aortic arch

The computed WSS distributions exhibit significant spatial heterogeneity. The WSS in the ascending aorta, especially upstream of the entrance of the innominate artery, was found to be low (however, it should be noted that the computed WSS distribution in this vascular region may be affected by the simplified inflow boundary condition). The WSS distribution in the outer curvature of the aortic arch exhibited great heterogeneity, with areas of significant low WSS (e.g. upstream of the entrance the major branch vessels) and areas of high WSS (e.g. downstream of the entrance of the innominate artery and flow dividers). On the other hand, WSS distribution in the inner curvature was found to be qualitatively lower and spatially more homogeneous.

In the three cases considered, an unexpected WSS pattern is observed in the inner wall of the proximal descending aorta. Such deviation in the WSS distribution is produced by a cusp at the attachment site of the ligamentum arteriosum. This result highlights the accuracy of the surface definition, showing that small-scale features have been preserved. Note that the variation in WSS due to the cusp are of the same order of magnitude as flow-induced variations.

The WSS distribution was found to depend significantly on Re. Increasing Re increases the strength of the vortical structures that develop in the arch, leading to increasing relative differences between areas of low and high WSS. For lower Re (Re = 50), the vortical structures that form in the arch are weak, resulting in a relatively homogeneous WSS distribution. However, for large Re (Re = 300 and Re = 1300) a greater spatial heterogeneity of the WSS distribution is observed, due to a stronger secondary flow.

Discussion

It is often assumed in the literature that the inner curvature of the aortic arch is exposed to low WSS, while the outer curvature exhibits high WSS levels [126, 76]. The results presented in this section suggest that such an accepted hypothesis may be too simplistic. Blood flow within the aortic arch was found to be highly complex. In particular, the formation of two vortices of unequal strength in the aortic arch leads to complex asymmetric flow and WSS patterns.

The cusp due to the ligamentum arteriosum causes a deviation in WSS comparable to that produced by blood flow features. This result emphasises the role of vascular geometry on WSS distribution and highlights the need to obtain detailed and faithful computational geometries in order to accurately model blood flow.

In terms of pathological relevance, regions of low WSS in the proposed model qualitatively correlate with the sites of disease prevalence described by Farthing [41]. To the author's knowledge, no other previous studies have investigated the lesions distribution within the rabbit aortic arch in mature rabbits.

The described WSS patterns are in good agreement with those computed by Ethier *et al.* [95] and Shahcheraghi *et al.* [127] for the mouse and human aortas respectively. Such studies also reported a great heterogeneity in WSS distribution in the aortic arch. They found low WSS levels in the inner curvature region, and high WSS levels at flow dividers and certain locations within the outer curvature region.

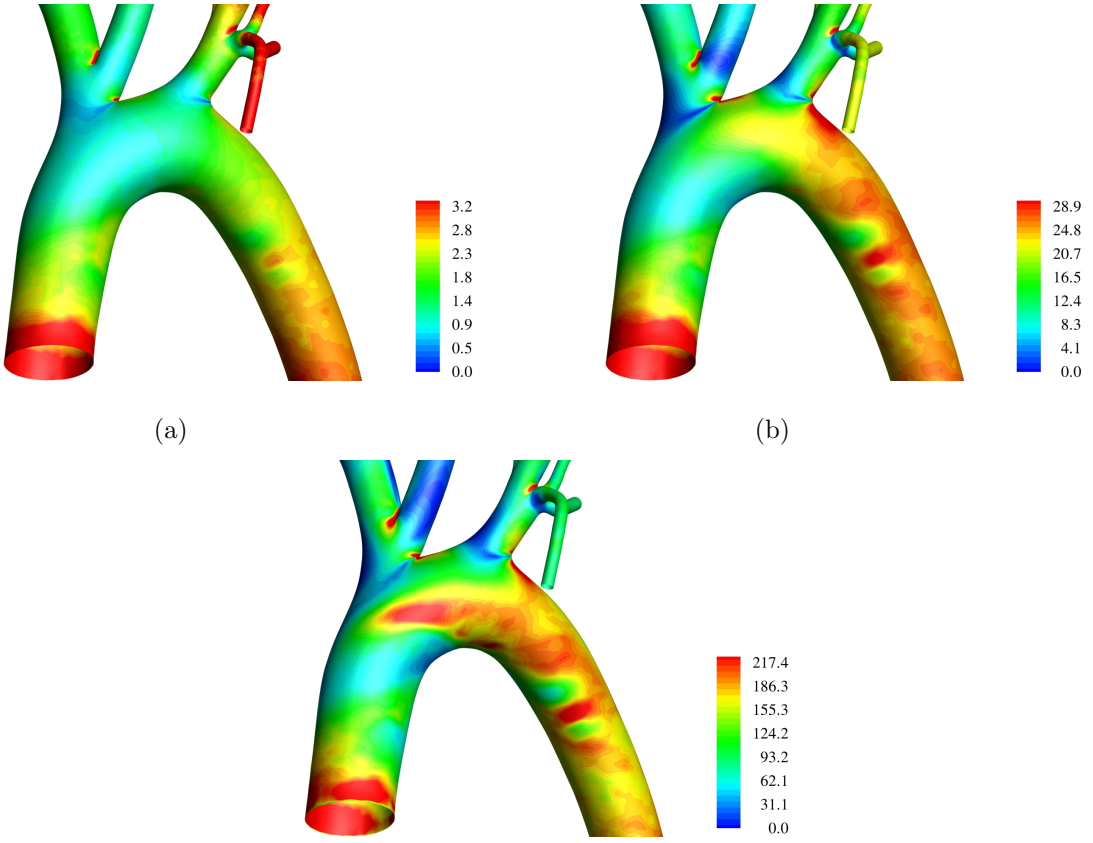


Figure 4.6: Colour maps of WSS (dynes cm^{-2}) at the aortic arch viewed ventral-dorsal for Re = 50 (a), Re = 300 (b) and Re = 1300 (c).

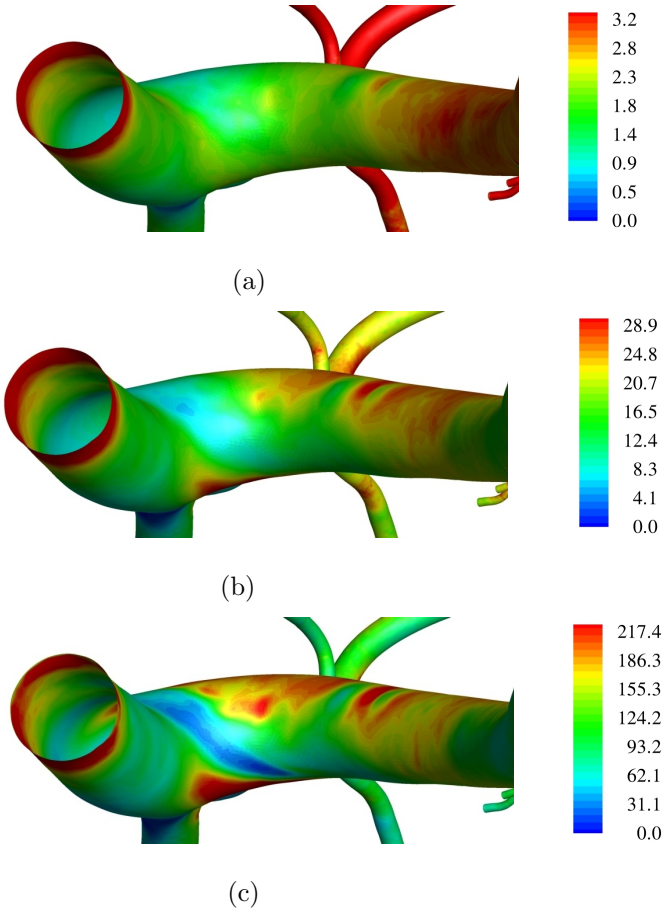


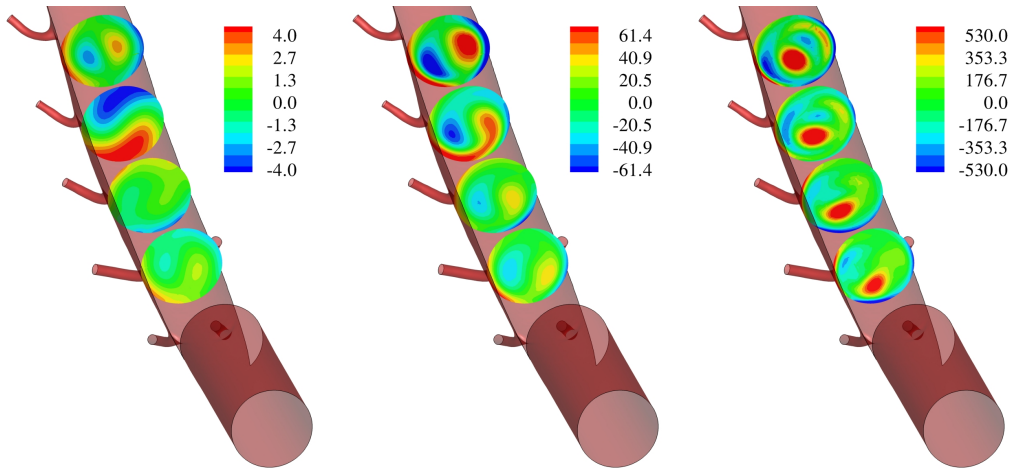
Figure 4.7: Colour maps of WSS (dynes cm^{-2}) at the aortic arch viewed posterior-anterior for Re = 50 (a), Re = 300 (b) and Re = 1300 (c).

4.3.2 Blood flow in proximal descending thoracic aorta

Figures 4.8 - 4.10 illustrates the complexity of blood flow in the proximal descending thoracic aorta. The two Dean vortices generated in the aortic arch propagate along the vessel. It can be observed that the strength of the vortices decreases streamwise as does the secondary motion induced by the aortic curvature (Fig. 4.8). For large enough Reynolds numbers (e.g. Re = 300 and Re = 1300) the axial velocity is skewed to one side and rotates about the streamwise axis, describing a helical trajectory (Fig. 4.9).

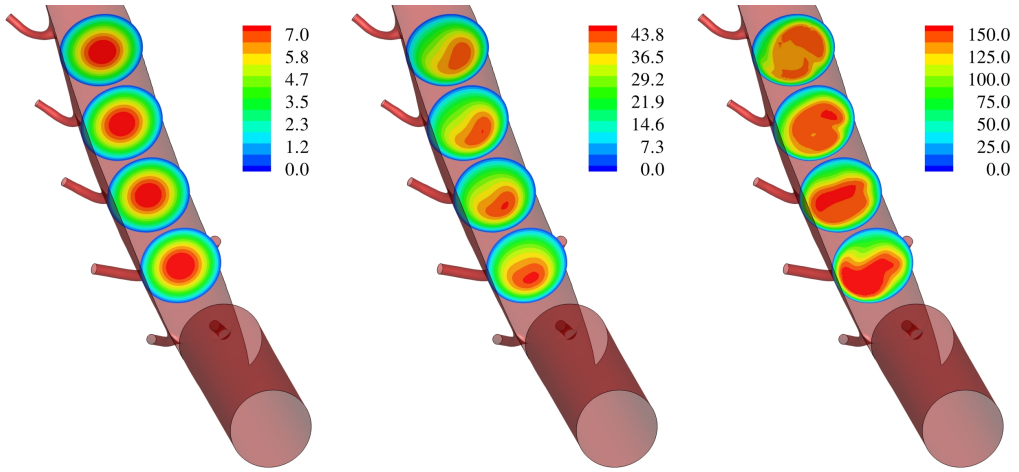
The configuration of vortices in the descending aorta is found to highly depend on

Re. The strength and asymmetry of the Dean vortices increases with Re, as illustrated in Fig. 4.10. Further, for large Re it is found that the centrifugal forces associated with the aortic curvature are sufficient to induce the formation of secondary vortices in the vicinity of the arterial wall [133]. These secondary vortices interact with the primary Dean vortices leading to complex internal vortical configurations (Fig. 4.8(c)).



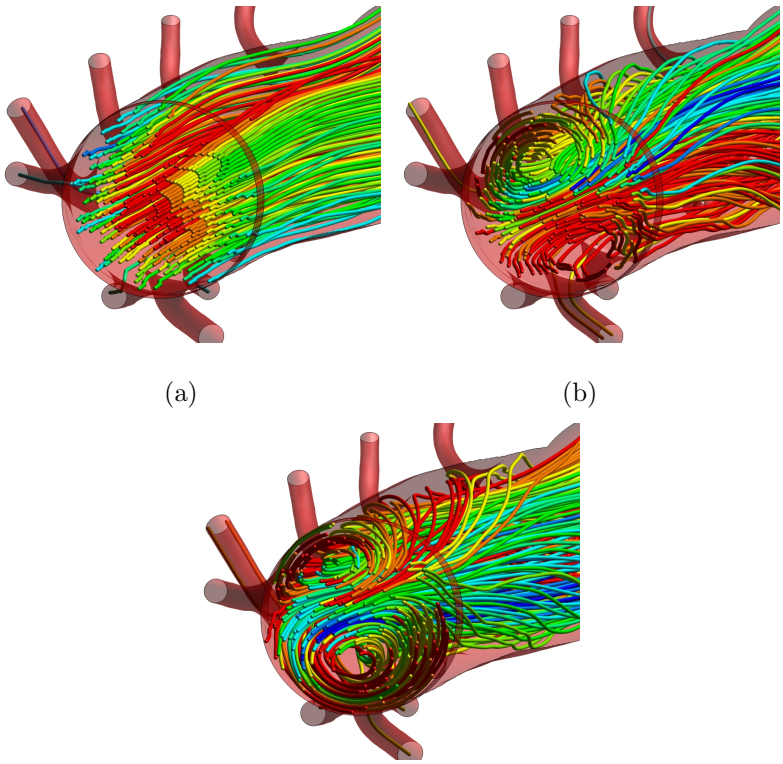
(a) (b) (c)

Figure 4.8: Colour maps of blood vorticity (s^{-1}) perpendicular to four planes within the descending aorta viewed ventral-dorsal for Re = 50 (a), Re = 300 (b) and Re = 1300 (c).



(a) (b) (c)

Figure 4.9: Colour maps of blood flow velocity (cms^{-1}) perpendicular to four planes within the descending aorta viewed ventral-dorsal for Re = 50 (a), Re = 300 (b) and Re = 1300 (c).



(a) (b)

(c)

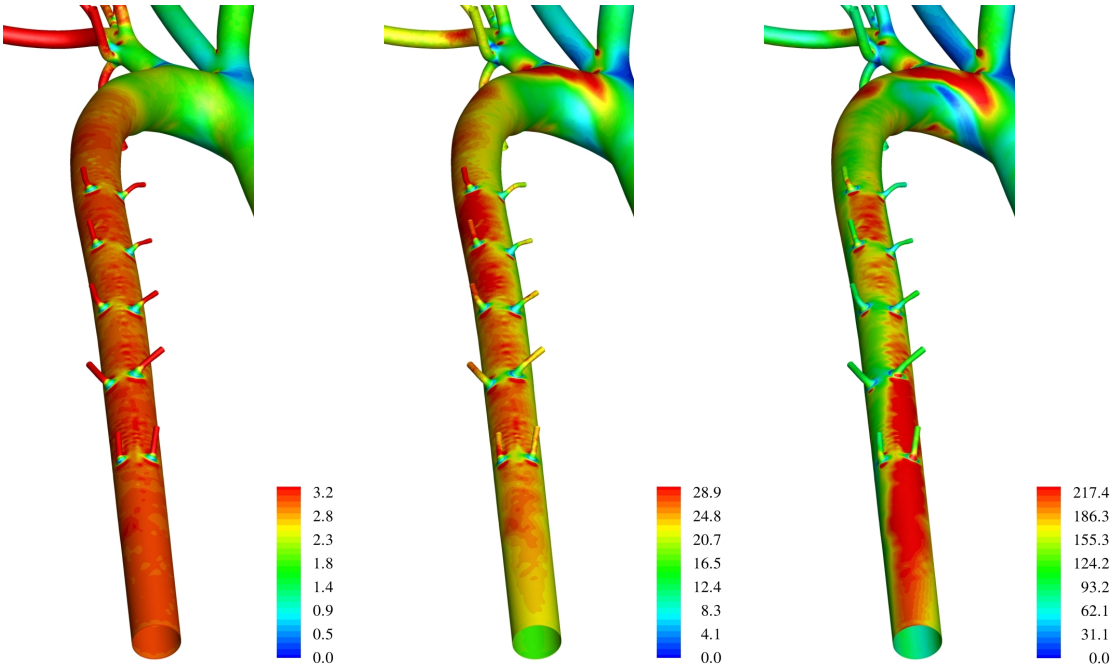
Figure 4.10: Streamlines of blood flow in the descending thoracic aorta viewed posterior-anterior for Re = 50 (a), Re = 300 (b) and Re = 1300 (c).

Wall shear stress

The computed WSS distribution is shown in Figs. 4.11 and 4.12. In the latter, WSS distribution is shown in the computationally-unwrapped descending aorta (created via a computational incision along the ventral aortic wall) and with the endothelial surface facing upwards, in order to facilitate comparison of numerical and experimental data.

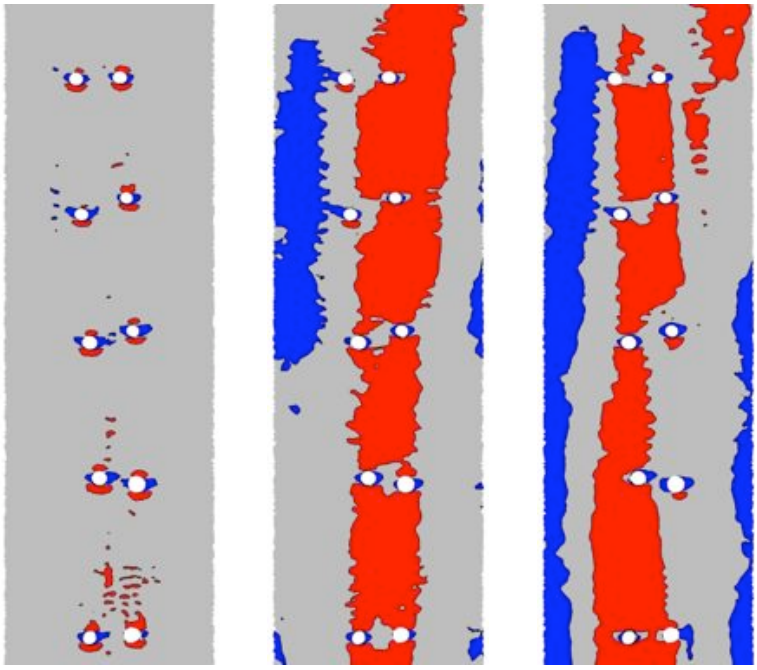
The macroscale WSS in the descending aorta is largely influenced by the presence of the Dean-type vortices. The skewness of the axial velocity (that is affected by the vortices structure) causes streaks of low and high WSS. Such streaks rotate streamwise following the rotation of the axial velocity.

The WSS distribution in the descending aorta depends significantly on Re. For a given vascular geometry, the skewness of the axial velocity dictate the location of the low and high WSS streaks, and hence the macroscale WSS distribution. In particular, an increase in Reynolds number is associate with enhanced swirling of the blood flow, resulting in greater rotation of the axial velocity (and hence the WSS streaks) about the streamwise axis.



(a) (b) (c)

Figure 4.11: Colour maps of WSS (dynes cm^{-2}) at the proximal descending thoracic aorta, viewed dorsal-ventral, when Re = 50 (a), Re = 300 (b) and Re = 1300 (c).



(a) (b) (c)

Figure 4.12: *En face* three tone colour maps of WSS in the descending aorta when Re = 50 (a), Re = 300 (b) and Re = 1300 (c). For the Re = 50 case blue denotes a WSS < 2.5 dynes cm^{-2} and red denotes a WSS > 3.2 dynes cm^{-2}. For the Re = 300 case blue colour denotes a WSS < 15.2 dynes cm^{-2} and red denotes a WSS > 23.4 dynes cm^{-2}. For the Re = 1300 case blue denotes a WSS < 77.6 dynes cm^{-2} and red denotes a WSS > 155.0 dynes cm^{-2}. In all cases the descending aorta was unwrapped via a computational incision along the ventral aortic wall. The colour maps are presented with the endothelial surface facing upwards. Flow direction is from top to bottom is all images.

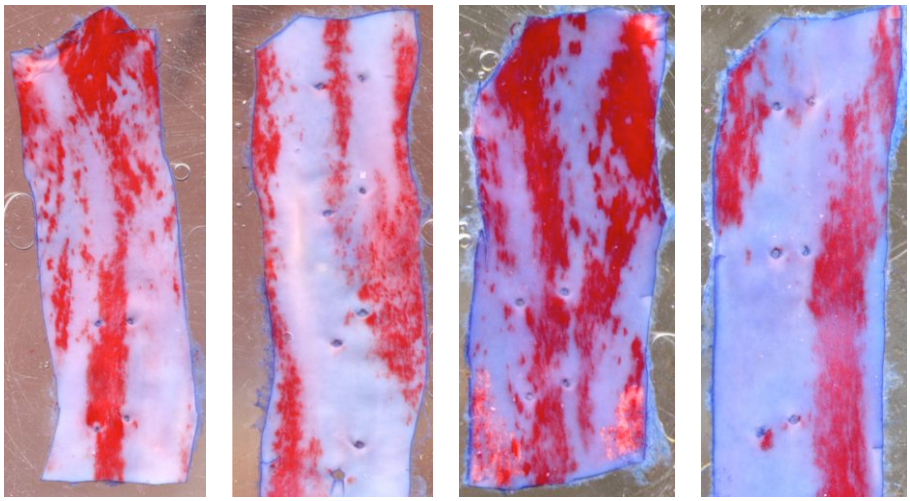
Discussion

The distribution of atherosclerotic lesions in the descending aorta has been extensively investigated for the rabbit [11, 10]. Several experimental studies have reported the presence of streaked lesion patterns in the proximal thoracic aorta in mature rabbits, as shown in Fig. 4.13. Further, enhanced wall permeability in the rabbit thoracic aorta has been reported to *"occur in streaks largely oriented in the bulk flow direction"* [10]. In this study the computed WSS was also found to exhibit a streaked distribution. This result certainly suggests that blood flow –in particular

WSS– plays a significant role in regulating the onset of the disease. However, drawing further conclusions (such as establishing a direct correlation between the streak of low WSS and the disease) is not yet possible, given the disease pattern variability across specimens (Fig. 4.13) and the lack of lesion data for the rabbit studied.

We hypothesise that the marked heterogeneity in the location of the streaked lesions across specimens may be partially driven by subject-specific geometrical features. In particular, the aortic torsion [157] and tapering may have a significant influence on the secondary motion (hence on the WSS distribution) in the descending aorta. Further computational work is needed in order to assess such the effect of geometrical features on blood flow.

To the author's knowledge only two previous studies have modelled blood flow within the descending aorta in the mouse [58] and the human [83], although no thorough analysis was provided by [58]. In [83] blood flow was also found to follow a helical trajectory within the proximal descending human aorta, leading to a streaked WSS distribution similar to that reported in this study.



(a) (b) (c) (d)

Figure 4.13: *En face* view of sections from the descending aorta of mature cholesterol-fed New Zealand White rabbits stained with oil red O dye to identify fatty streaks (early stage atherosclerotic lesions). In all cases the descending aorta was unwrapped via a incision along the ventral aortic wall, and the sections are shown with the endothelial surface facing upwards. Images (a) and (b) are from the same aorta. The most proximal section in shown in (a); containing the first and second pair of intercostals branches. A more distal section is shown in (b) containing the fourth, fifth, sixth and seventh pair of intercostals branches. Images (c) and (d) correspond to a different aorta. Image (c) shows the first and the second pair of intercostal arteries while image (d) shows the fourth, fifth, sixth and seventh pairs. Note that the third pair of intercostals branches is missing from both data sets as they were used in a different study. Blood flow is from top to bottom in all images. Unpublished data courtesy of S. G. Cremers, S. J. Wolffram and P.D. Weinberg, obtained following an identical procedure to Weinberg *et al.* [11].

4.3.3 Blood flow in the vicinity of the intercostal arteries

Figure 4.14 shows the computed WSS distribution in the vicinity of the intercostal arteries. It can be observed that the macroscale WSS patterns within the descending aorta are superimposed on local shear patterns produced by the blood flow entering the intercostal arteries.

Local WSS patterns are similar across intercostal arteries, with high WSS regions upstream and downstream of the entrance of the arteries, and low WSS areas at the sides and the lip. It can be noted that such local patterns do not exhibit a significant dependence on Re, suggesting that local WSS distribution may be mainly determined by the vascular geometry. On the other hand, the macroscale WSS that the intercostal region is exposed to depends strongly on Re, as described in a previous section. Therefore, WSS distribution surrounding the intercostal arteries is affected by both, the vascular geometry (the branching configuration and the position of the branch within the descending aorta) and the underlying macroscale flow field.

Discussion

A number of experimental studies have identified the vicinity of the intercostal arteries entrance as a site of disease prevalence in immature rabbits [11]. Lesion patterns surrounding the branches ostia are known to vary within a specimen (different intercostal pairs exhibit different lesion distributions). This study shows that the descending aorta is exposed to spatially-varying complex WSS distribution. Such diverse range of WSS environments in which branch pairs reside may explain variation in disease between branch pairs. This result calls into question the accepted experimental practise of averaging disease patterns over many branch pairs in order to construct disease maps.

Previous computational studies have investigated blood flow entering the intercostals branches using geometrically idealised models of the aorto-intercostal junction [68]. These studies assumed uniform flow conditions (generally Poiseuille flow) within the descending aorta. Here it is shown that the intercostal arteries are exposed to a complex non-uniform flow field instead, leading to substantial differences in WSS across intercostal arteries. Therefore, the applicability of studies considering idealised aortic flow conditions may be restricted to the study of local WSS features.

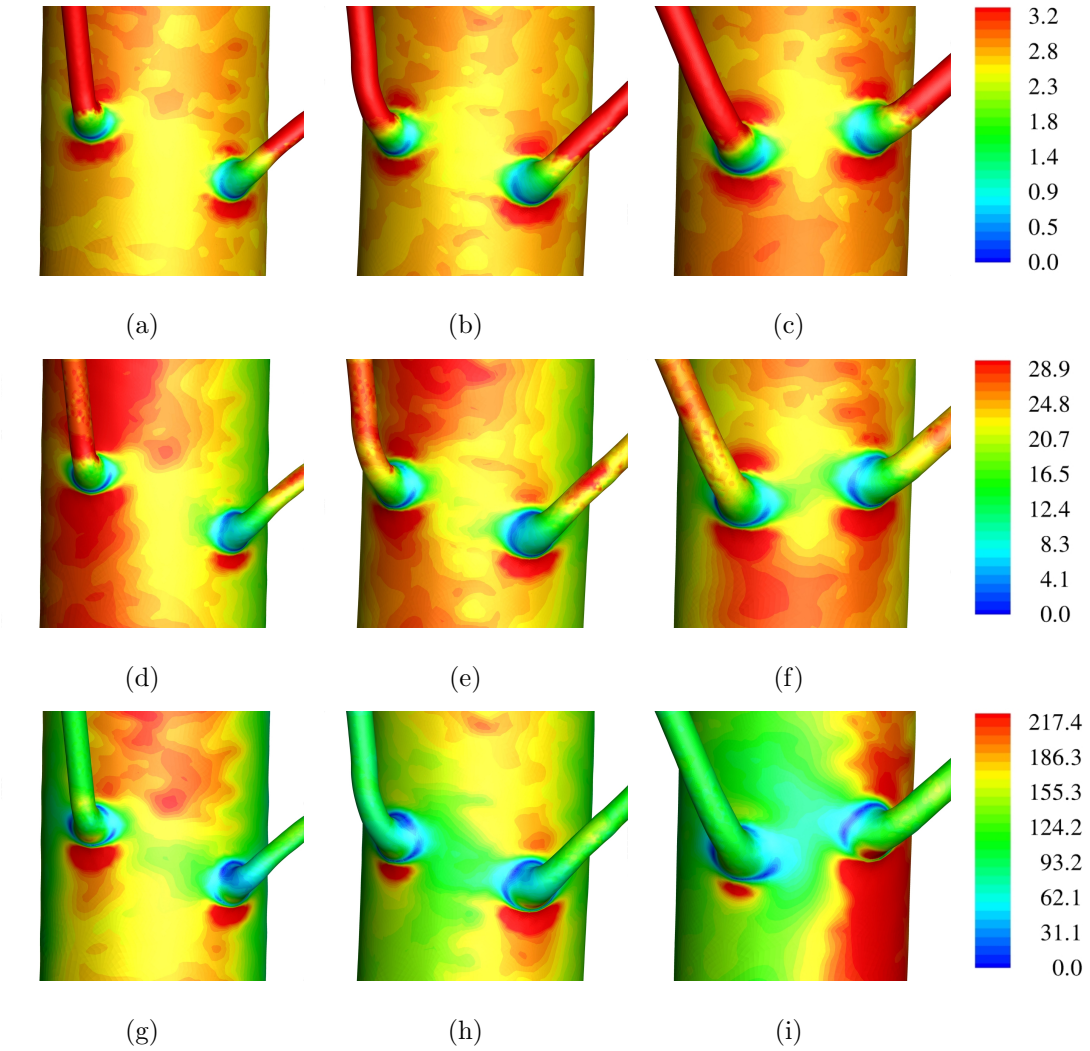


Figure 4.14: Colour maps of WSS (dynes cm^{-2}) at the vicinity of the second pair of intercostal arteries for Re = 50 (a), Re = 300 (d) and Re = 1300 (g); at the third pair of intercostal arteries for Re = 50 (b), Re = 300 (e) and Re = 1300 (h); and at the fourth pair of intercostal arteries for Re = 50 (c), Re = 300 (f) and Re = 1300 (i). Images in each row corresponds to the same Re, while images in each column correspond the same branch pair.

4.4 Summary

Blood flow was numerically investigated within a realistic representation of the rabbit aorta. The vascular geometry was reconstructed from high resolution CT scan

data of a vascular corrosion cast. In terms of combined detail and extent, the computational geometry represents a significant advance *c.f.* previous studies.

The computed blood flow was highly complex. The curvature of the aortic arch was found to induce the formation of two Dean-type vortices that propagated along the descending aorta. Such vortices were unequal in strength, leading to asymmetric flow features. Further, other geometrical features such as the aortic torsion and tapering act to further increase the flow complexity. The computed WSS distribution exhibited a marked spatial heterogeneity. This result suggest that widely accepted hypotheses on vascular WSS distribution (such as that the inner aortic arch is exposed to low WSS) may be too simplistic.

For physiologically realistic Reynolds numbers the axial velocity in the descending aorta was found to be follow a helical trajectory, rotating about the streamwise axis. This skewness of the axial velocity results in streaks of low and high WSS. Since atherosclerosis lesions are also streaked in the descending aorta in mature rabbits, the results of this study certainly support the hypothesis that flow (in particular WSS) mediates the onset of the disease.

It is also found that the local WSS patterns around the intercostal arteries produced by the blood flow entering the vessels are superimposed on the streaked macroscale WSS distribution within the descending aorta. Such diverse range of WSS environment in which pairs reside may explain variation in disease between branch pairs. This result calls into question the accepted experimental practise of averaging disease patterns over many branch pairs in order to construct disease maps.

The results of this study emphasises the importance of geometrical accuracy when computing vascular WSS distribution. In particular it is showed that small-scale features, such as the cusp at the attachment site of the ligamentum arteriosum, cause deviations in the WSS of the same order of magnitude as flow-induced variations. Further, the vascular geometry (in particular the aortic torsion and tapering) may play a significant role in the formation and propagation of Dean vortices, and hence in determining the localisation of the WSS streaks. Therefore further computational

work is encouraged in order to assess the effect of diverse geometrical features on blood flow. Finally, future studies should aim to overcome the present limitations of the model, and include more complex physics such as pulsatile flow and compliant walls.

Chapter 5

Nitric Oxide Transport in the Rabbit Aorta

This chapter presents a computational study of NO production and transport within the rabbit aorta and its branches. Vascular NO concentration is calculated using the mathematical model of endothelial NO production proposed in Chapter 3, along with the blood flow field computed in Chapter 4. Endothelial NO distribution is investigated in detail, along with its possible relevance to the spatially heterogeneous distribution of atherosclerotic plaques.

5.1 Introduction

Reduced bioavailability of Nitric Oxide (NO) is postulated to be one of the factors that mediate atherogenesis [27]. Under physiological conditions, NO produced by the endothelium is thought to be the major NO source for regulating vascular tone and endothelial health [22]. Endothelial NO production has been shown to depend significantly on the level of WSS that the endothelium is exposed to [37, 65]. This WSS-dependent production of NO (possibly in conjunction with blood flow-dependent NO transport) may provide an explanation for the flow-mediated onset

of the atherosclerosis.

However, despite its relevance to the disease, many aspects of endothelial NO production and vascular NO transport remain unclear. In particular, the relationship between endothelial NO production and WSS remain quantitatively uncharacterised. Further, the kinetics of NO reaction with multiple vascular components (especially haemoglobin) is a major point of contention in the literature [4].

Previous computational studies modelling NO transport have helped gaining understanding of vascular NO dynamics [144, 134, 96]. However, such studies present several limitations. First, vascular NO transport is investigated within idealised vascular geometries. In particular vessels are assumed to be infinite straight cylinders. Further, blood flow dynamics are not modelled, and Poiseuille flow is assumed within the vessel studied. Therefore the endothelium is assumed to be uniformly exposed to WSS, and hence NO transport becomes bidimensional in nature. Finally, variations in NO production with WSS are often not considered.

Furthermore, previous work has focused on investigating NO transport within the microvasculature [144, 96, 134, 145]. To the author's knowledge, no previous studies have modelled NO transport within a realistic representation of the major arteries (where atheromas actually develop). In the present study, vascular NO transport is investigated within the same vascular geometry used in Chapter 4 (the rabbit aorta and its branches). This chapter aims to contribute towards an enhanced understanding of vascular NO transport within major arteries in the vasculature, identifying key parameters that regulate vascular NO concentration.

5.2 Methods

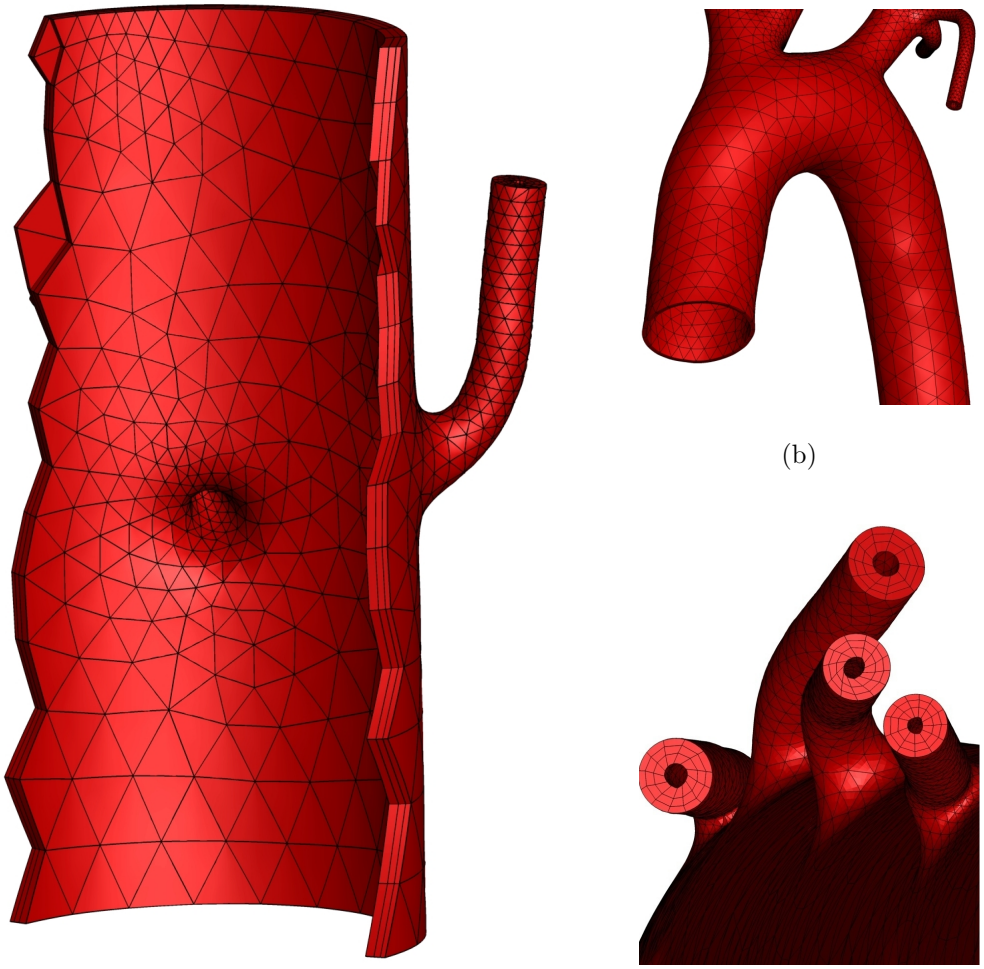
5.2.1 Obtaining the computational geometry

Vascular NO production and transport is investigated within the rabbit aorta and its branches, using the same vascular geometry as in Chapter 4. The reader is referred to section 4.2.1 for a complete description of the methodology employed to obtain the computational surface definition.

5.2.2 Generating a computational mesh

Luminal NO is known to be confined within a thin concentration boundary layer adjacent to the luminal side of the endothelium [22]. Thus, since the NO concentration C_{NO} in the core of the vessel lumen is known (C_{NO}=0), meshes of solely the boundary layer can be used in order to reduce the computational cost.

The boundary layer mesh was generated with Tgrid 2.0.24 (ANSYS, Inc). Three layers of prismatic elements with a thickness of 50, 67 and 91 μm respectively (corresponding to a total thickness of 208μm) were defined first. Subsequently, the faces of both the internal and external surface elements were curved using SPHERIGON patches [147], as described in Chapter 2. The resulting boundary layer mesh shown in Fig. 5.1 contains 76,494 prismatic elements. It will be shown later (section 5.2.5) that the NO concentration boundary layer is well contained within the computational domain.



(a) (b) (c)

Figure 5.1: Images of the high-order curved boundary layer mesh showing an axial section of the descending thoracic aorta (a), the aortic arch (b), and four intercostal arteries (c). The computational mesh contains 76,494 prismatic elements. Note that both the internal and external mesh surfaces have been curved.

5.2.3 Computational model of nitric oxide production and transport within the vasculature

5.2.3.1 Overview

Endothelial NO production is thought to play a fundamental role in the regulation of vascular tone and endothelial health. NO production has been shown to depend

significantly on the level of WSS that the endothelium is exposed. However, the specific form of the endothelial response to WSS remains uncharacterised.

NO produced in the endothelium rapidly diffuses into both the subjacent arterial wall and the lumen of the vessel. In the lumen, NO readily reacts with haemoglobin contained in the RBCs. Some authors [123, 74] have suggested that the kinetics of such a reaction may be altered by the existence of NO diffusional barriers and competing reactions of NO with other constituents of blood plasma. Finally, note that NO diffusing into the lumen is convected downstream by the flow of blood.

In the arterial wall, NO activates a complex signalling pathway which leads to SMC relaxation, and therefore vasodilation. NO dynamics within the arterial wall have as yet not been quantitatively characterised. In particular, the level of NO concentration necessary to trigger the vasodilation pathway remains a point of contention, with values in the literature that vary over several orders of magnitude (see [22] and references therein).

5.2.3.2 Simplified model

The overview given above highlights the multiple aspects involved in vascular NO transport and the lack of a quantitative characterisation of many of them. This section proposes a simplified model for vascular NO production and transport within the rabbit aorta. The model makes the following assumptions:

- As in Chapter 4, blood flow dynamics are assumed to be quasi-steady. Vascular NO transport is investigated using the blood flow field computed in Chapter 4 for the case Re = 300, corresponding to the average aortic root velocity within the cardiac cycle.
- Convective NO transport due to the flow of blood is neglected. Note that although convective transport is neglected, vascular NO transport is still influenced by haemodynamics, since NO production depends strongly on the

WSS distribution (that directly depends on the blood flow).

This assumption is justified in Appendix B. It is found that for cases where a WSS-dependent NO production rate is considered, NO convective transport is negligible for NO reaction rates with blood k_{Hb} greater than 100 s^{-1}. Further, when a constant NO production rate is considered, NO convective transport is found to be negligible regardless of the value of k_{Hb}. The previous discussion is applicable to most vascular regions considered in this study. However the effect of convection on NO transport may be significant in vascular areas exposed to extreme shear rates, such as the vicinity of the flow dividers at the aortic arch (see Appendix B for full details). Therefore, the proposed model may fail to accurately predict NO distribution in such areas.

- NO diffusion into the arterial wall is neglected. Previous computational studies [144, 96] have shown that endothelial NO distribution is dominantly governed by the luminal NO dynamics. Further, recent experimental evidence suggest that NO diffusion within the arterial wall may be significantly slower than in blood [84], reinforcing the leading role of luminal NO dynamics in endothelial NO distribution. Finally, the effect of NO diffusion into the arterial wall is unlikely to affect the relative endothelial NO distribution, since NO dynamics within the arterial wall are thought to be homogenous within the vasculature (it can be described using 1D equations in the radial direction, as there is no axial convection within the arterial wall) [144].

  Nevertheless, we acknowledge that neglecting NO diffusion into the arterial wall may affect the level of endothelial NO concentration. In particular, the model may overestimate endothelial NO concentration levels, as NO migration into the wall is not considered. Further, the model fails to predict NO concentration within the arterial wall (where NO vasodilation action takes place).

- As in Chapter 3, the kinetics of the intracellular reactions that lead to NO production are not modelled. In particular, the effects of cellular eNOS distribution or the substrate availability on endothelial NO production are not

considered. However, such effects are unlikely to significantly influence the macroscale NO distribution [23].

Despite the previous simplifications, the model provides an enhanced understanding of vascular NO distribution, identifying key parameters that regulate NO production and transport and highlighting aspects of NO transport that require further experimental characterisation.

To the author's knowledge, this is the first study investigating NO production and transport within a 3D realistic representation of the macrovasculature. Therefore this study should be understood as a first step towards more sophisticated multiscale models that eventually will integrate all the different aspects involved in vascular NO transport.

5.2.3.3 Governing equation

In line with the previous assumptions, NO transport is modelled within the vessel lumen using the steady-state diffusion-reaction equation

$$0 = D_{NO}\nabla^2 C_{NO} - V_{NO}, \tag{5.1}$$

where (as in Chapter 3) C_{NO} represents NO concentration, D_{NO} is the NO diffusion coefficient and V_{NO} is the rate at which NO is consumed by reaction within the lumen, which will be shown shortly to depend on C_{NO}.

5.2.3.4 NO reaction within the vessel lumen

NO is known to be readily scavenged by haemoglobin. In fact, the half-life of NO in the presence of physiological concentrations of free haemoglobin ($\sim$ 10 mM) is estimated to be 1 μs based on *in vitro* measurements. However, if NO was consumed by haemoglobin at such a rapid rate *in vivo*, NO vasodilator action would be impeded [51].

During the last decade extensive research has been conducted to solve this paradox. Two types of mechanisms have been postulated to prevent NO being scavenged by haemoglobin: diffusional barriers and competing chemical reactions of NO with other constituents of blood.

A number of diffusional barriers have been suggested to hinder NO diffusion from the endothelium to the haemoglobin contained in RBCs [123, 74, 22]. First, the RBCs membrane is thought to constitute an intrinsic barrier to NO diffusion into the cell (vascular haemoglobin is encapsulated within the RBC, rather than free in blood plasma). This may lead to the formation of a NO unstirred layer around to RBC that eventually may act to further slow NO uptake. Second, NO diffusion into the arterial wall may be facilitated by the existence of a RBC-free layer attached to the luminal side of the endothelium. Within this layer (formed due to steric effects) NO is postulated to be consumed at a much lower rate. However, while the existence of a RBC-free layer in the microvasculature is widely accepted [73], its presence in the major arteries remains contentious.

Competing reactions of NO with other substances in blood plasma may also reduce NO consumption by haemoglobin. In particular, NO is postulated to react with plasma constituents to yield a number of nitrogen compounds (nitrites, nitrated lipids and other nitrosylated species) [87]. Recent experimental evidence suggest that such nitrogen compounds may be reconverted in NO under hypoxic conditions, and hence blood may potentially act as a NO reservoir [132, 135].

The quantitative effect of the diffusional barriers and the competing reactions described above on luminal NO dynamics remains unclear [22]. A number of mathematical models have been proposed in order to simulate NO interaction with blood. Here a similar approach to that adopted by [144] is employed, and NO reaction with haemoglobin is modelled as a pseudo-first order reaction (haemoglobin concentration is assumed to be constant within the vasculature). Further, a RBC-free layer adjacent to the endothelium is considered. Within this layer, NO consumption kinetics are also assumed to be first order. Therefore the reactive term V_{NO} in Eq. 5.1

can be expressed as

$$V_{NO} = \begin{cases} \mathrm{k}_{Hb} C_{NO}, & \text{if } \eta > \delta, \\ \mathrm{k}_{pl} C_{NO}, & \text{if } \eta \leq \delta, \end{cases}$$

where k_{pl} is the NO reaction rate with blood plasma, η is a coordinate in the direction normal to the arterial wall, and δ is the thickness of the RBC-free layer attached to the endothelium. Note that the effect of the RBC membrane and the unstirred layer, as well as the reversible competing reactions, on NO luminal consumption are included within the parameters k_{Hb} and k_{pl}. Figure 5.2 illustrates the model proposed for NO reaction within the arterial lumen.

5.2.3.5 Endothelial nitric oxide production

The following model for endothelial NO production was developed in Chapter 3. The reader is referred to section 3.2.4 for further details. The NO production rate R_{NO} at the endothelium is modelled as

$$R_{NO} = \frac{R_{NO_{\mathrm{MAX}}}}{1 + \gamma \exp(-W_{\mathrm{o}}|\tau|)}, \tag{5.2}$$

where (as in Chapter 3)

- $R_{NO_{\mathrm{MAX}}}$ is the maximum production rate, which corresponds to the product of the maximum intracellular eNOS concentration and the maximum catalytic velocity rate.
- τ represents WSS magnitude.
- γ and W_{o} are parameters that characterise the endothelial response to WSS. This nomenclature is consistent with that used in [108] and [151].

Figure 5.2 illustrates the model proposed for NO production and transport within the vasculature.

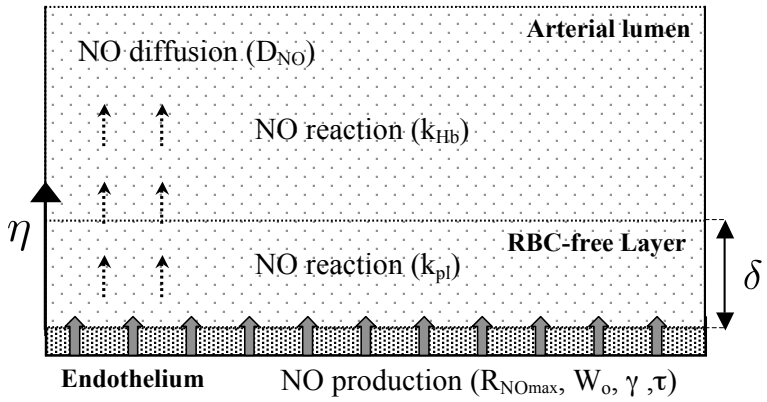


Figure 5.2: Diagram illustrating how vascular NO transport is modelled within the rabbit aorta. NO is produced by the endothelium. It subsequently diffuses into the lumen of the vessel (diffusion into the arterial wall is not modelled), where it reacts with different blood constituents.

5.2.3.6 Boundary conditions

Wall boundary condition

At the outer mesh wall (representing the interface between the endothelium and the lumen of the vessel), a balance between NO production and NO transport is enforced. Thus at the outer mesh wall

$$R_{NO} = -D_{NO}\frac{\partial C_{NO}}{\partial \eta}.$$

Outflow boundary conditions

The NO concentration boundary layer is assumed to be fully developed at the outflows. Therefore, the NO concentration flux at the outflows is set to be zero. Note that such an assumption has a negligible effect on NO concentration within the rest of the computational domain, since the height of the NO concentration boundary layer (H) is significantly lesser than the aortic diameter (*i.e.* $\frac{H}{D_o} << 1$).

Inner mesh wall boundary condition

Since a boundary layer computational mesh is used, an extra boundary condition needs to be imposed at the inner mesh wall. Following the discussion in section 5.2.2, NO concentration is set to be zero.

5.2.3.7 Parameters

As shown in previous sections, the NO concentration C_{NO} depends on NO diffusivity D_{NO}, the NO reaction rate within the lumen k_{Hb} and k_{pl}, the thickness of the RBC-free layer δ, the relationship between NO production and WSS (characterised by the parameters W_o, γ, $R_{NO_{MAX}}$), and the WSS distribution that the endothelium is exposed to. Table 5.1 defines the ranges over which these parameters are varied. Recall that NO transport is investigated using the blood flow computed in Chapter 4 for the case Re = 300. Thus the WSS field is known.

Symbol	Range, Units	Description
D_{NO}	$3.3 \cdot 10^{-5}$ cm^{2}s^{-1}	NO diffusion coefficient [90]
$R_{NO_{MAX}}$	$8.33 \cdot 10^{-4}$ μM cm s^{-1}	Maximum NO production rate
k_{Hb}	10 - 10^6 s^{-1}	NO reaction rate with haemoglobin
k_{pl}	0 - 10^2 s^{-1}	NO reaction rate with blood plasma
δ	0 - 50 μm	RBC-free layer thickness
W_o	0 - ∞ Pa^{-1}	Parameter endothelial response to WSS (see text)
γ	0-100	Parameter endothelial response to WSS (see text)

Table 5.1: Description of the parameters ranges used for the simulation of vascular NO production and transport within the rabbit aorta

Note that the NO diffusion coefficient is known (D_{NO} = 3.3 x 10^{-5}cm^{2}s^{-1} [90]). Also note that the maximum NO production rate $R_{NO_{MAX}}$ is assumed to be 8.33 x 10^{-4} μM cm s^{-1}. This value of NO production rate is within the ranges reported in the literature [23], and leads to a characteristic NO concentration C_o = 1 μM

($C_o = \frac{HR_{NO_{\mathrm{MAX}}}}{D_{NO}}$, where H is the height of the NO concentration boundary layer), that is consistent with previous computational studies [144]. Further, in Chapter 3, $R_{NO_{\mathrm{MAX}}}$ was found to scale NO concentration, but not to affect NO distribution (see section 3.2.7). Therefore, the vascular NO distribution for other values of the parameter $R_{NO_{\mathrm{MAX}}}$ can be obtained by simply scaling the NO concentration computed in this study.

Note that the remaining parameters (k_{Hb}, k_{pl}, δ, W_{o} and γ) have been varied over an extremely wide range. The scarce –and often conflicting– experimental data present in the literature have motivated the choice of such wide ranges.

5.2.4 Numerical methods

NO concentration was calculated using the in-house spectral/hp element method solver $Ne\kappa\tau\alpha r$ [156] as described in Chapter 2. An expansion basis of 8^{th} order was used to represent the solution within each element. Such an expansion corresponds to $\sim$ 8.72 x 10^6 degrees of freedom in total.

Convergence was verified by performing NO transport simulations for a fixed point within the parameter space ($W_{\mathrm{o}} = 0.14\mathrm{dynes}^{-1}$ cm^2, $\gamma = 10$, $\mathrm{k}_{Hb} = 1\mathrm{s}^{-1}$ and $\delta = 0$) using 6^{th}, 8^{th} and 10^{th} order expansions. It was found that the average concentration varied by 0.3% when going from the 6^{th} to the 8^{th} order expansions; and 0.05% when going from the 8^{th} to the 10^{th} order expansions. Thus, it was assumed that the solution had converged when using a 8^{th} order expansion.

5.2.5 Suitability of the computational boundary layer mesh

In order to test the suitability of the boundary layer mesh described in section 5.2.2 (of thickness of 208 μm), three additional boundary layers meshes of a thickness of 220, 316 and 350 μm were generated. It was found that the average NO concentration varied by less than 0.1% within the four meshes for a number of NO simulations.

Therefore, the use of a boundary layer mesh is justified. Figure 5.3 illustrates that the NO concentration boundary layer is well contained within the computational mesh.

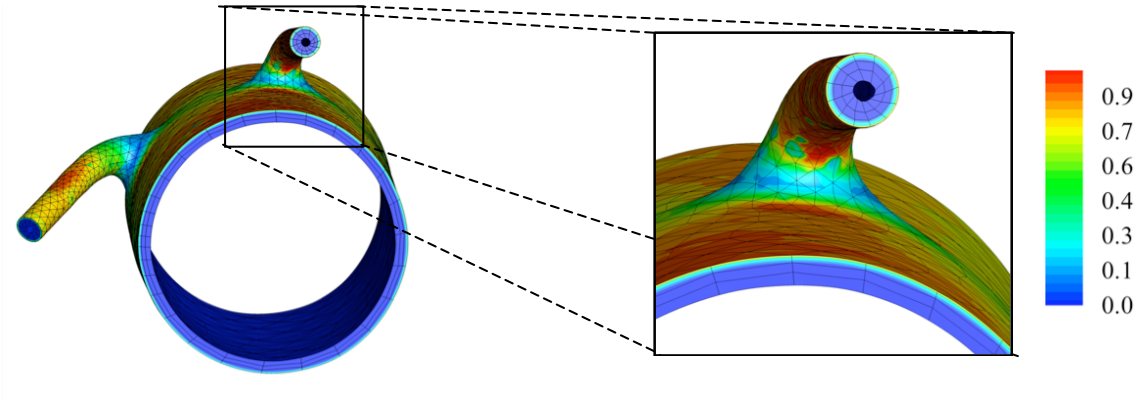


Figure 5.3: Colour maps of non-dimensional NO concentration viewed at a cross-section within the descending thoracic aorta for fixed ($W_o = 0.14$dynes cm^{-2}, $\gamma = 10$, $k_{Hb} = 10$s^{-1} and $\delta = 0$). Note that the NO concentration boundary layer is well confined within the computational mesh.

5.3 Results

This section analyses the effects of the endothelial response to WSS (section 5.3.1), the NO reaction rate within the lumen (section 5.3.2.1) and the thickness of the RBC-free layer (section 5.3.2.2) on vascular NO concentration within the rabbit aorta and its branches.

5.3.1 Effect of the endothelial response to WSS on vascular NO distribution

The dependence of endothelial NO production rate on WSS is characterised by the parameters W_o and γ. This section investigates the effect of such parameters on vascular NO distribution. Fig. 5.4 shows plots of the non-dimensional NO production

rate R^*_{NO} (where as in Chapter 3 R^*_{NO}=$\frac{R_{NO}}{R_{NO_{\mathrm{MAX}}}}$) for various values of the parameter W_{o} and a plot of a constant NO production rate. The red dashed vertical lines indicate the WSS range that over 98% of the endothelium surface is exposed to in the studied case. Note that WSS levels in certain regions of the vasculature (e.g. flow dividers) exceed the upper bound of this range.

The effect of W_{o} and γ on NO production rate was described in detail in Chapter 3. The parameter W_{o} was shown to characterise the sensitivity of the endothelial response to WSS, while the parameter γ was shown to characterise the basal level of NO production (see section 3.3.1 for further details).

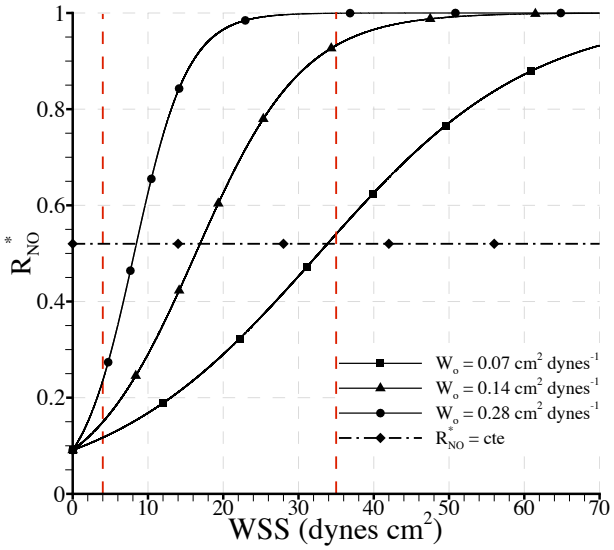


Figure 5.4: Plots of a R^*_{NO} against WSS (dynes cm^2) for several values of the parameter W_{o} with fixed $\gamma = 10$ (solid lines). A plot of a constant production rate (dot-dashed line) is also shown. This constant NO production rate is equal to the average NO production rate computed for the case $W_{\mathrm{o}} = 0.14\mathrm{dynes}^{-1}\mathrm{cm}^2$ within the computational domain. The red dashed vertical lines indicate the WSS range that over 98% of the endothelium is exposed to in the studied case.

5.3.1.1 Effect of WSS-dependent *vs.* constant endothelial NO production rate on NO distribution

In this section the NO distributions obtained using a constant NO production rate ($R^*_{NO} = 0.52$), and a WSS-dependent production rate ($W_o = 0.14 \text{dynes}^{-1}\text{cm}^2$ and $\gamma = 10$), are compared. The constant NO production rate is chosen to be equal to the average NO production rate for the WSS-dependent case. Therefore, the net NO production is the same for the two cases compared. Note that cases where a constant NO production rate is considered are not physiologically relevant, although they will be shown to be conceptually important.

The computed NO distributions, along with the WSS distribution computed in Chapter 4, are shown within the aortic arch (Fig. 5.5), the descending thoracic aorta (Fig. 5.6) and the vicinity of the intercostal arteries (Fig. 5.9). In order to facilitate comparisons between different cases, NO concentration is non-dimensionalised with the maximum NO concentration in the descending thoracic aorta computed for each case.

Constant NO production rate

In cases where a constant NO production rate is considered, NO distribution is found to be homogenous within most of the computational domain. However, areas of high curvature such as the inner wall at the aortic arch (Fig. 5.6c), and areas of arterial branching (Figs. 5.5c - 5.7c) exhibit small variations in NO concentration. Further, it can also be observed that NO concentration is greater within the smaller vessels emanating from the aorta (Fig. 5.7c) than within the aorta itself.

Note that when a constant NO production rate is considered, all the parameters that regulate NO transport (R_{NO}, k_{Hb} and δ) are constant throughout the computational domain. Further, note that convective transport has been neglected (section 5.2.3.2). Therefore, variations in NO concentration for this cases can only be induced by the vascular geometry itself.

Indeed, NO production is proportional to the endothelial surface (hence NO production increases linearly with the vessel diameter), while NO consumption within blood is proportional to the volume enclosed by such surface (thus NO consumption increases quadratically with the vessel diameter). In areas of high curvature and arterial branching the ratio volume-surface increases (in such areas the volume surrounding the endothelial surface is greater than in the cylindrical body of the aorta), leading to a reduction in endothelial concentration. Similarly, NO concentration also decreases with increasing vessel diameter, since the ratio volume-surface increases.

The dependence of endothelial NO concentration on the diameter of the vessel has been discussed in previous computational studies [144]. However, to the author's knowledge the decrease in endothelial NO concentration in areas of high curvature and arterial branching (where atheromas develop preferentially) had not been previously reported. Such a result is significant, as it highlights the influence of vascular geometry *per se* on endothelial NO distribution.

WSS-dependent NO production rate

For the WSS-dependent production rate studied ($W_o = 0.14 \text{dynes}^{-1}\text{cm}^2$ and $\gamma = 10$), the relationship between endothelial NO production and WSS is almost linear for the relevant WSS range (Fig. 5.4). Therefore, the endothelial NO distribution is similar to the WSS distribution in the majority of the computational domain.

However, small discrepancies between WSS and NO distribution patterns can be observed in areas of great curvature (such as the inner wall of the aortic arch) and arterial branching. Further, increased levels of endothelial NO concentration can be observed within the smaller vessels emanating from the aorta (especially in the intercostal arteries). In these vascular regions, geometrical factors were shown to induce changes in NO concentration that affect endothelial NO distribution in the previous section. These geometrically-induced variations result in the aforementioned differences between WSS and NO distributions. Note that such variations in endothelial NO concentration due to volumetric effects are inappreciable within

most of the computational domain. However in certain key vascular regions such as in the aortic arch, geometrically-induced C_{NO} variations are most noticeable.

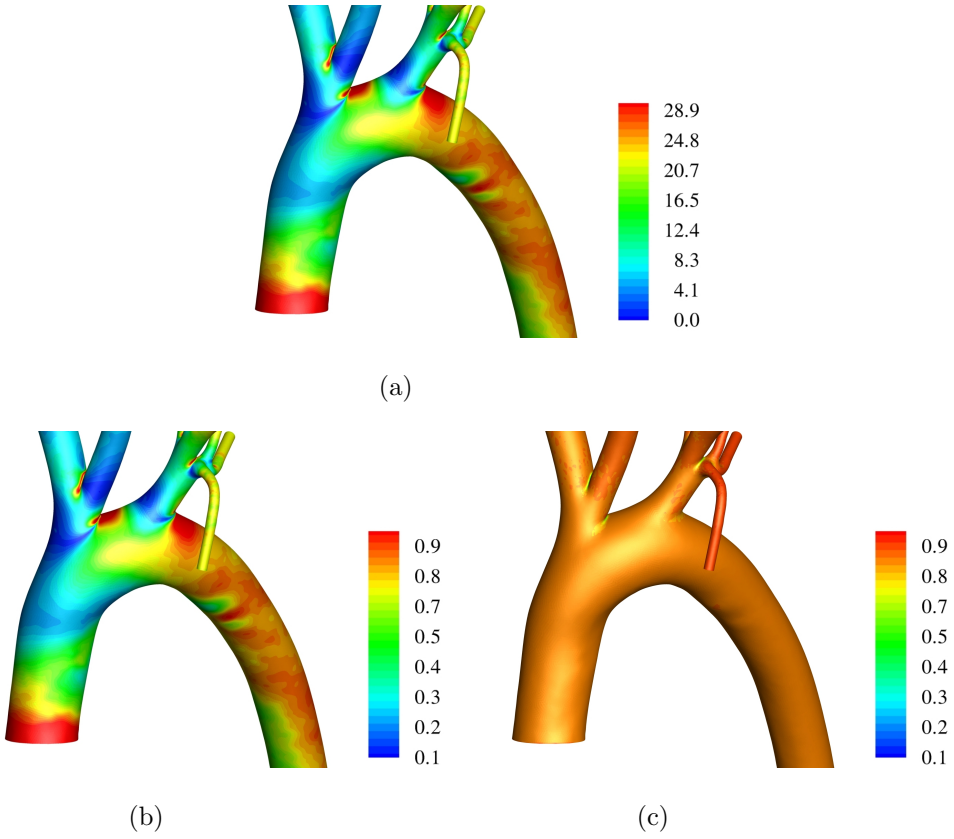
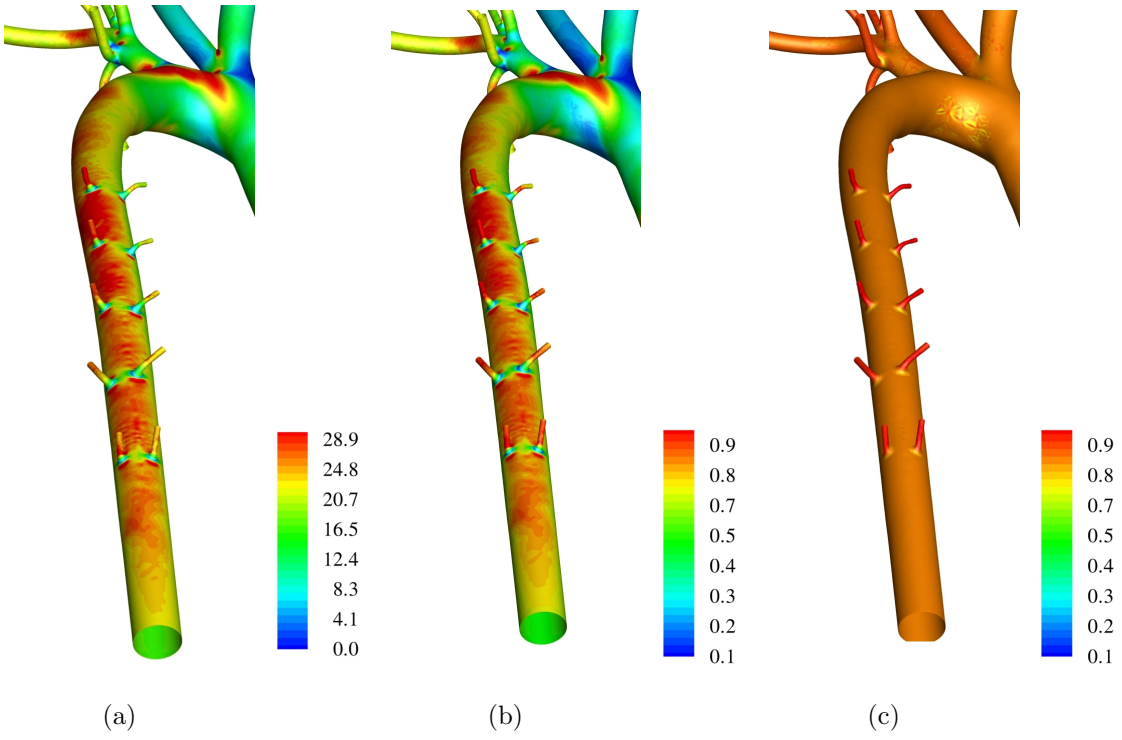


Figure 5.5: Colour maps of WSS (dynes cm^{-2}) (a) and non-dimensional NO concentration (b-c) in the aortic arch viewed ventral-dorsal. NO concentration colour maps are shown for $W_o = 0.14$dynes^{-1}cm^2 (b), and a constant NO production rate (c), with fixed $\gamma = 10$ and $k_{Hb} = 100s^{-1}$. The constant NO production rate imposed in (c) is equal to the average NO production rate computed for the case $W_o = 0.14$dynes^{-1}cm^2 (b). NO concentration has been non-dimensionalised using the maximum NO concentration in the descending aorta for each case.



(a) (b) (c)

Figure 5.6: Colour maps of WSS (dynes cm^{-2}) (a) and non-dimensional NO concentration (b-c) in the descending aorta viewed dorsal-ventral. NO concentration colour maps are shown for $W_o = 0.14 dynes^{-1} cm^2$ (b), and a constant NO production rate (c), with fixed $\gamma = 10$ and $k_{Hb} = 100 s^{-1}$. The constant NO production rate imposed in (c) is equal to the average NO production rate computed for the case $W_o = 0.14 dynes^{-1} cm^2$ (b). NO concentration has been non-dimensionalised using the maximum NO concentration in the descending aorta for each case.

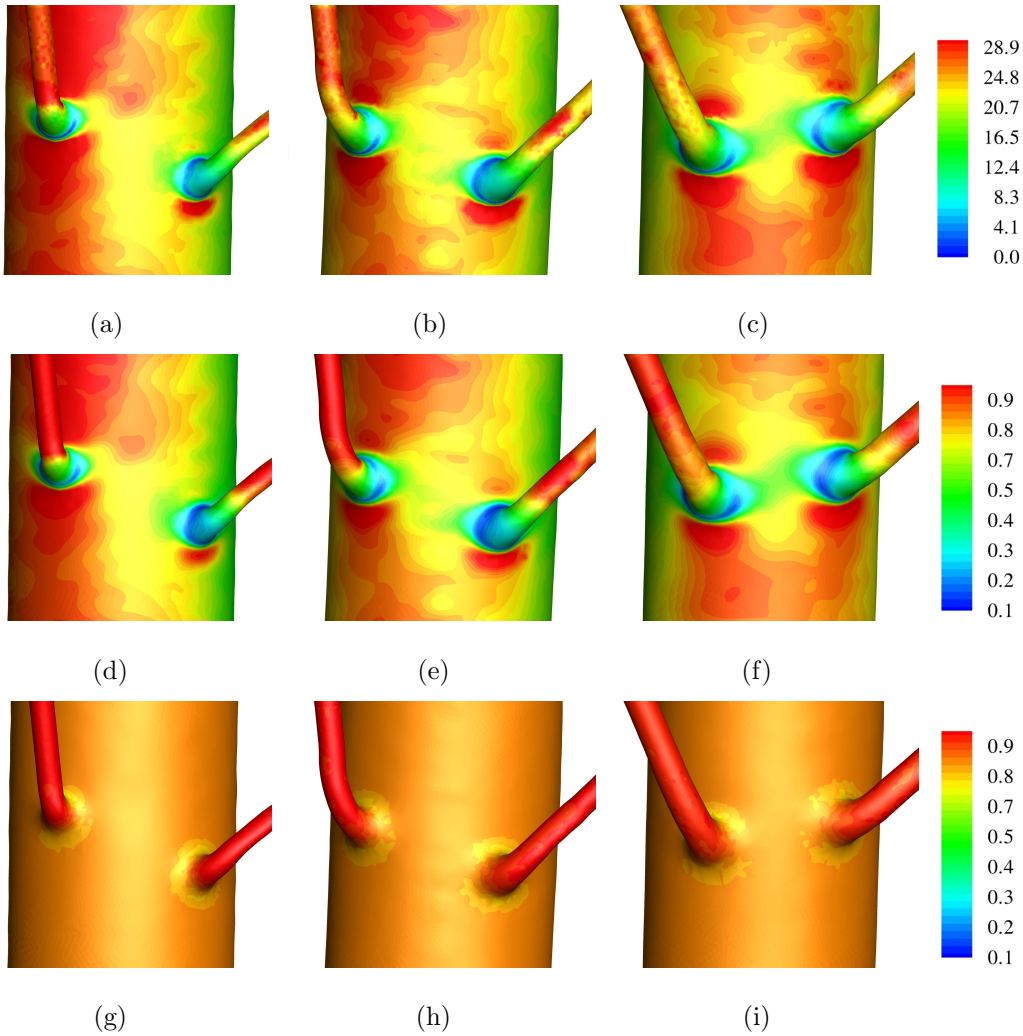


Figure 5.7: Colour maps of WSS (dynes cm^{-2}) (a-c) and non-dimensional NO concentration (d-i) in the vicinity of the intercostal arteries viewed dorsal-ventral. The first, second and third columns shows images corresponding to the second, third and four pairs of intercostal arteries respectively. NO concentration colour maps are shown for $W_o = 0.14 dynes^{-1} cm^2$ (d-f), and a constant NO production rate (g-i), with fixed $\gamma = 10$ and $k_{Hb} = 100 s^{-1}$. The constant NO production rate imposed in (g-i) is equal to the average NO production rate computed for the case $W_o = 0.14 dynes^{-1} cm^2$(d-f). NO concentration has been non-dimensionalised using the maximum NO concentration in the descending aorta for each case.

5.3.1.2 Effect of the specific form of the endothelial response to WSS

The previous section investigated vascular NO distribution for a given relationship between endothelial NO production and WSS. However, the specific form of the endothelial response to WSS remains uncharacterised and hence NO distribution should be investigated for a number of endothelial responses.

In this section endothelial NO distribution is investigated for the three WSS-dependent endothelial responses illustrated in Fig. 5.4. The computed NO distributions, along with the WSS distribution computed in Chapter 4, are shown within the aortic arch (Fig. 5.8) and within the third pair of intercostal arteries (Fig. 5.9). In order to facilitate comparisons between different cases, NO concentration is non-dimensionalised using the maximum NO concentration in the descending thoracic aorta computed for each case.

Endothelial NO distribution is found to depend significantly on the specific form of the endothelial response to WSS. For the case $W_o = 0.14 \text{dynes}^{-1}\text{cm}^2$, the relationship between endothelial NO production and WSS is almost linear for the WSS range studied. Therefore, the endothelial NO distribution is similar to the WSS distribution in most vascular regions (it has been shown previously that geometrical factors induce variations in NO concentration in certain vascular locations).

The case $W_o = 0.07$ dynes^{-1}cm^2 represents a less sensitive endothelial response to WSS, and hence the maximum NO production rate is not reached in the majority of the computational domain. Since less NO is produced by the endothelium, NO concentration is lower than in the previous case.

Finally, the case $W_o = 0.28$ dynes^{-1}cm^2 is associated with a very sensitive endothelial response to WSS, where the maximum NO production rate is reached within the WSS range considered. Thus, the endothelial NO concentration is higher than in the other cases. Further, NO distribution is more homogenous, since NO production reaches the saturated level within the physiologically relevant WSS range.

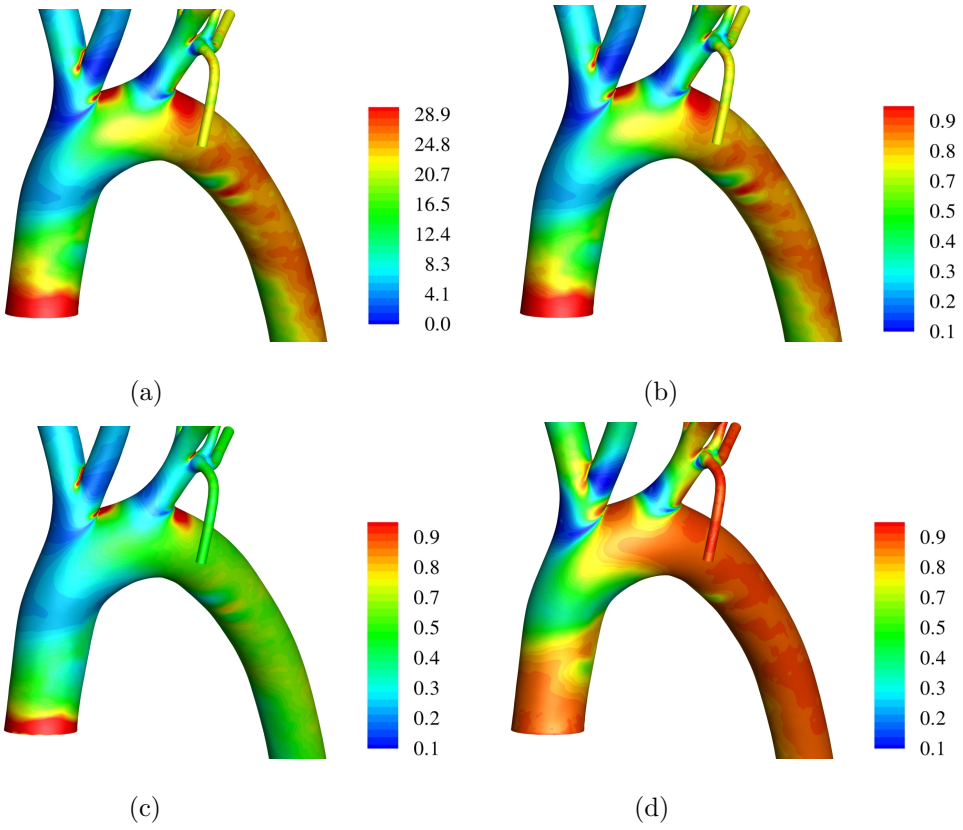


Figure 5.8: Colour maps of WSS (dynes cm^{-2}) (a) and non-dimensional NO concentration (b-d) in the aortic arch viewed ventral-dorsal. NO concentration colour maps are shown for $W_o = 0.14$ dynes^{-1}cm^2 (b), $W_o = 0.07$ dynes^{-1}cm^2 (c) and $W_o = 0.28$ dynes^{-1}cm^2 , with fixed $\gamma = 10$, $k_{Hb} = 100s^{-1}$ and $\delta = 0$. NO concentration has been non-dimensionalised using the maximum NO concentration in the descending aorta for each case.

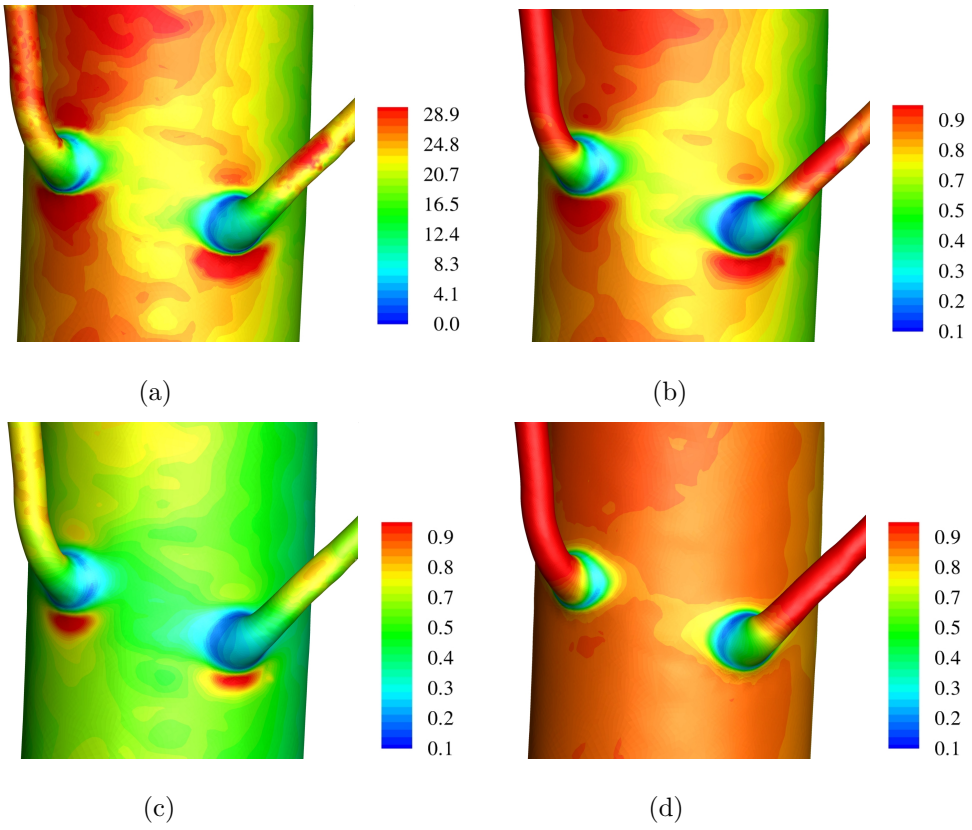


Figure 5.9: Colour maps of WSS (dynes cm^{-2}) (a) and non-dimensional NO concentration (b-d) in the vicinity of the third pair of intercostal arteries viewed dorsal-ventral. NO concentration colour maps are shown for $W_o = 0.14$ dynes^{-1}cm^2 (b), $W_o = 0.07$ dynes^{-1}cm^2 (c) and $W_o = 0.28$ dynes^{-1}cm^2 , with fixed $\gamma = 100$, $k_{Hb} = 100s^{-1}$ and $\delta = 0$. NO concentration has been non-dimensionalised using the maximum NO concentration in the descending aorta for each case.

5.3.1.3 Influence of the basal NO production (γ)

The effect of the parameter γ was also investigated. It was found that the parameter γ acted to scale endothelial NO concentration. However, it did not affect the NO distribution structure within the vascular region studied (data not shown).

5.3.1.4 Influence of NO reaction within the lumen (k_{Hb} and k_{pl}) and the thickness of the RBC-free layer δ

Vascular NO transport simulations were carried out for different values of the parameters k_{pl}, k_{Hb} and δ. It was found that such parameters largely determine the value of endothelial NO concentration, as discussed in subsequent sections. However, the NO distribution pattern was not significantly affected (data not shown).

5.3.2 Effect of NO reaction within the vessel lumen

This section investigates the effect of NO reaction within the vessel lumen for cases where a RBC-free layer is not considered (i.e. $\delta = 0$) and cases where a RBC-free layer is considered (i.e. $\delta \neq 0$).

5.3.2.1 Effect of NO reaction with haemoglobin on vascular NO concentration when a RBC-free layer is not modelled ($\delta = 0$)

This section investigates the effect of NO reaction within the vessel lumen when a RBC-free layer is not modelled. NO transport simulations are performed for the constant NO production rate studied in section 5.3.1 ($R^*_{NO} = 0.52$). The average endothelial NO concentration over the whole geometry ($\bar{C}_{NO_{ec}}$) and the effective NO diffusion distance into the lumen are investigated in detail. Figure 5.10 shows a plot of $\bar{C}_{NO_{ec}}$ against k_{Hb}, and Figure 5.11 plots NO concentration at an arbitrary point within the thoracic descending aorta against η (coordinate in the direction normal to the arterial wall). The horizontal red-dashed line in both figures corresponds to an NO concentration of 1nM. This level of NO concentration is highlighted since it is representative of the estimated value for physiological NO concentrations in plasma [136].

It is observed that the average endothelial NO concentration ($\bar{C}_{NO_{ec}}$) and the NO effective diffusion distance depend significantly on the rate of NO reaction with

haemoglobin k_{Hb}. As expected, both $\bar{C}_{NO_{ec}}$ and the NO diffusion distance rapidly decrease with increasing k_{Hb}. Such a decrease becomes more significant as the parameter k_{Hb} (and hence the rate of NO consumption) rises.

Endothelial NO concentration is effectively zero for cases where $k_{Hb} > 10^4 s^{-1}$. Therefore, if NO reacted within the lumen at the same rate as it does with free haemoglobin ($k_{Hb} \sim 10^5 s^{-1}$), it would be completely scavenged by blood and its vasodilation action would be impeded. Note that in order for $\bar{C}_{NO_{ec}}$ to reach the physiologically relevant level of 1nM, k_{Hb} is found to be of the order of $\sim 10 s^{-1}$. Such a value for the NO reaction with haemoglobin *in vivo* is one order of magnitude lower than the lowest previous estimations [22].

Regarding NO effective diffusion distance, it can be seen that for $k_{Hb} \geq 10\ s^{-1}$ the NO concentration boundary layer is confined within a few micrometers of the endothelial surface. This result illustrates the difficulty of obtaining direct *in-vivo* NO measurements in the lumen vessel.

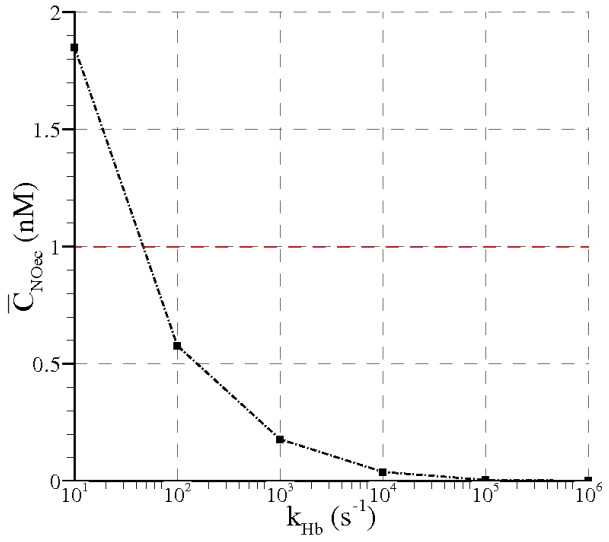


Figure 5.10: Plots of the average endothelial NO concentration $\bar{C}_{NO_{ec}}$ (nM) against NO reaction rate with haemoglobin k_{Hb} (s^{-1}) with fixed $\delta = 0$.

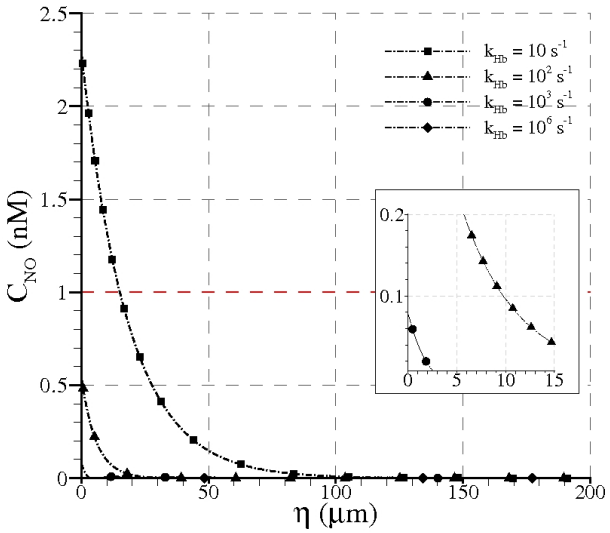


Figure 5.11: Plots of NO concentration (nM) at an arbitrary point within the thoracic descending aorta against the coordinate in the direction normal to the arterial wall η (μm) for various values of k_{Hb} and with fixed $\delta = 0$. Note that this plot is found to be effectively independent of the point studied, since a constant NO production was assumed and hence NO distribution is notably homogeneous.

5.3.2.2 Effect of NO reaction with haemoglobin on vascular NO concentration when a RBC-free layer is modelled ($\delta \neq 0$)

This section investigates the effect of a RBC-free layer on NO concentration. As in the previous section, NO transport simulations are performed for the constant NO production rate studied in section 5.3.1 ($R^*_{NO} = 0.52$). Figure 5.12 shows a plot of $\bar{C}_{NO_{ec}}$ against k_{Hb} for several values of the parameter δ. Further, Figure 5.13 plots NO concentration at an arbitrary point within the thoracic descending aorta against η for several values of the parameter δ and with fixed $k_{Hb} = 10^3 s^{-1}$ and $k_{pl} = 0$. As in the previous section, the horizontal red-dashed line in both figures corresponds to the physiologically relevant NO concentration of 1nM.

Results are presented for the limiting case $k_{pl} = 0$ (i.e. NO reaction rate within the RBC-free boundary layer is neglected). Although this assumption is not physiolo-

gically realistic, it is conceptually relevant as it represents the case where the effect of the RBC-free layer on NO concentration is maximum.

It can been seen that the average endothelial NO concentration ($\bar{C}_{NO_{ec}}$) increases significantly with increasing δ. In particular it is observed that $\bar{C}_{NO_{ec}}$ exceeds 1nM when $\delta \geq 10\mu$m . Further, note that when $\delta \neq 0$, NO concentration is not completely scavenged for any value of the parameter k_{Hb}.

The NO effective diffusion distance is also found to significantly depend on δ. In the case presented ($k_{pl} = 0$), NO can freely diffuse within the RBC-free layer without being scavenged. Thus, the increase in the NO diffusion distance is directly equal to the thickness of the RBC-free layer δ.

In cases where $k_{pl} \neq 0$, the increase in both NO diffusion distance and $\bar{C}_{NO_{ec}}$ was found to be less than in the results presented in this section (data not shown).

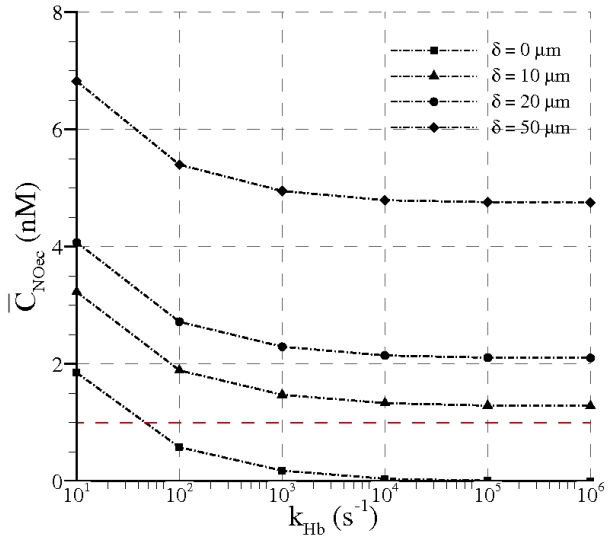


Figure 5.12: Plots of the average endothelial NO concentration $\bar{C}_{NO_{ec}}$ (nM) against NO reaction rate with haemoglobin k_{Hb} (s^{-1}) for various values of the RBC-free layer thickness δ with fixed $k_{pl} = 0$.

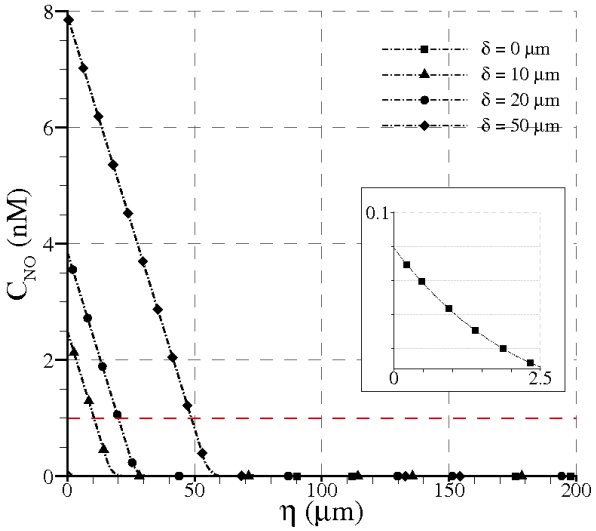


Figure 5.13: Plots of NO concentration (nM) at an arbitrary point within the thoracic descending aorta against the coordinate in the direction normal to the arterial wall η (μm) with fixed $k_{Hb} = 10^3 s^{-1}$ and $k_{pl} = 0$. Note that this plot is found to be effectively independent of the point studied, since a constant NO production was assumed and hence NO distribution is notably homogenous.

5.4 Discussion

5.4.1 Effect of blood flow on vascular NO concentration

The effect of blood flow (via the effect of WSS on NO production) on vascular NO concentration has been studied in detail. For physiologically realistic cases (when WSS-dependent NO production rate is considered), endothelial NO distribution is found to exhibit significant spatial heterogeneity. Such heterogeneity is mainly caused by spatial variation in WSS (and hence NO production) within the vascular region analysed. However it is found that certain geometrical features such as curvature and branching also induce appreciable variations in NO distribution. Further, it is shown that the level of endothelial NO concentration is influenced by volumetric considerations such as the vessel diameter.

Endothelial NO distribution is found to depend significantly on the specific form of the endothelial response to WSS. However, such a response remains quantitatively uncharacterised. Further experimental work is encouraged in order to determine the relationship between endothelial NO production and WSS.

Nevertheless, this is not the only aspect of NO production that requires further experimental characterisation. In this study vascular NO transport is investigated within the rabbit thoracic aorta and its branches. It has been suggested [22] that endothelial NO production may differ across the different levels of the arterial tree. In fact, the large discrepancies in the reported values of endothelial NO production rate may reflect such a hierarchy [22].

Further, the endothelial response to dynamic changes in WSS remains unclear. Both WSS distribution and magnitude significantly vary within the cardiac cycle, as shown in Chapter 4. *In vivo* experiments [25, 24] have shown that eNOS concentration, and hence NO production, varies in response to changes in WSS. However, the time scale over which such variations take place (in the order of days [24]) is notably greater than the cardiac cycle period (approximately 0.2s^{-1} in rabbits). Therefore, it has generally been assumed (as it has in this study) that endothelial NO production solely depends on the average WSS the endothelial cells are exposed to. Such an hypothesis may be too simplistic, and hence additional experimental work is needed to improve the current understanding of dynamic NO production. *In vitro* experiments within flow chambers using different flow regimes [150] and different types of endothelial cells may shed light on the aspects of vascular NO production previously discussed.

Finally, the effect of convective transport on vascular NO concentration needs further investigation. Here blood flow dynamics were assumed to be quasi-steady, and hence NO transport was studied for a given point within the cardiac cycle. Under such an assumption (and based on the shear rate levels computed in Chapter 4), convective NO transport was shown to be negligible within most of the computational domain for $\text{k}_{Hb} \geq 100\ \text{s}^{-1}$ (see Appendix B). However, wall shear rates at

peak systole are significantly higher than the average values considered here, and hence convection is likely to play a role in vascular NO transport for part of the cardiac cycle. Therefore, future studies should aim to model blood flow pulsatility and NO convective transport.

5.4.2 NO reaction within the lumen of the vessel

Endothelial NO concentration was found to depend significantly on the NO consumption rate within the vessel lumen. For cases where the RBC-free layer was not modelled ($\delta = 0$), NO was found to be completely scavenged for $k_{Hb} > 10^4 s^{-1}$. The NO reaction rate with free haemoglobin k_{Hb} is known to be of the order of $\sim 10^5 s^{-1}$. If NO was consumed by the haemoglobin contained in the RBCs at such rate *in vivo*, NO concentration would be effectively zero, and its vasodilation action would be impeded. Thus, it is reasonable to assume that there must exist some mechanisms preventing NO being scavenged by haemoglobin within the macrovasculature.

Diffusional barriers (such as the RBC membrane or the unstirred layer around it) may act to reduce the overall NO reaction rate within the lumen. However, it is found that such barriers should account for a reduction of four orders of magnitude in k_{Hb} (i.e. $k_{Hb} \sim 10$) in order for endothelial NO to reach the physiologically relevant concentration of 1nM.

The existence of a RBC-free layer adjacent to the endothelium has also been postulated to preserve NO bioavailability. When such a layer is modelled, endothelial NO concentration is found to significantly increase. In particular, endothelial NO is found to exceed 1nM regardless of the value of k_{Hb} when a RBC-free layer of a thickness of 10μm is considered and NO is assumed not to react within such a layer. However, the existence of a RBC-free within the major arteries remains unclear. Moreover, the dynamics of NO within such a layer remains uncharacterised.

Further experimental work is encouraged in order to elucidate the mechanisms that preserve NO bioactivity in the major arteries. In particular, NO concentration in

plasma measurements (such as those performed by Stamler et al. [136] in humans) may clarify luminal NO dynamics and validate associated computational studies. Furthermore, the thickness of the RBC-free layer (if any) within the macrovasculature needs quantitative characterisation.

Future computational work should aim to model NO transport in conjunction with other vascular species. For example, NO interaction with oxygen should be modelled, as certain NO reactions with blood constituents are reversible under hypoxic conditions.

5.5 Summary

Vascular NO transport within the rabbit aorta and its branches was investigated numerically. Endothelial NO distribution is found to reflect spatial variations in WSS (and hence endothelial NO production). However, it is observed that certain geometrical features, such as arterial curvature and branching, also induce significant variations in NO concentration. This result is relevant, as atheromas are reported to develop preferentially in such vascular regions. Further, such a result highlights the influence of the arterial geometry *per se* on vascular NO concentration, which has not been considered in most previous computational studies.

Endothelial NO distribution is found to depend significantly on the specific form of the endothelial response to WSS. Such a relationship, along with other aspects of endothelial NO production, remains uncharacterised. Hence this study provides renewed motivation for further experimental work.

The effect of NO reaction within the vessel lumen was also investigated. It was found that if NO reacted with haemoglobin *in vivo* at the same rate as it does with free haemoglobin, its vasodilation action would be impeded. Therefore it is postulated that mechanisms preventing NO consumption by haemoglobin also exist within the major vessels.

Diffusional barriers (such as the RBC membrane and the unstirred layer) may significantly reduce NO consumption rate within the vessel lumen. However, it is found that such barriers should act to reduce NO reaction rate by four orders of magnitude in order for NO concentration to reach physiologically realistic levels ($\sim$1nM). Further, the potential existence of a RBC-free layer adjacent to the endothelium is modelled. It was observed that when such a layer was considered, endothelial NO concentration substantially increased. However, the existence of a RBC-free layer in the major arteries remains contentious. Therefore, further experimental work is encouraged in order to determine the thickness of the RBC-free layer (if any) in the major arteries and determine NO dynamics within it.

To the author's knowledge, this is the first computational study investigating NO production and transport within a 3D realistic representation of the macrovasculature. Therefore this study should be understood as a first effort towards more sophisticated multiscale models. However, despite the present limitations, this study highlights the fundamental role of the arterial geometry and the WSS distribution in determining vascular NO concentration.

Chapter 6

Conclusions and Future Work

This chapter summarises the contributions of this thesis to the field, and discusses possible extensions and future work.

6.1 Summary of key results

This thesis investigated blood flow and nitric oxide (NO) transport numerically using a spectral/hp element method.

Firstly, NO production and transport were investigated within a parallel-plate flow chamber coated with endothelial cells. The relationship between endothelial NO concentration and wall shear stress (WSS) was investigated in detail. Contrary to the accepted hypothesis that NO concentration increases with WSS, we observed that endothelial NO concentration depends on WSS in a non-monotonic fashion. It was also observed that a NO concentration boundary layer develops within the flow chamber, leading to significant spatial variations in NO concentration along the length of the device. These findings call into question the methodology followed in previous experimental studies, as discussed in Chapter 3. Further, the results of this study emphasise the effect of convection on NO transport within flow chambers,

which has been overlooked or misinterpreted in most previous theoretical studies.

Secondly, blood flow was modelled within a highly detailed representation of the rabbit aorta and its branches. This study highlighted the significant effect of vascular geometry on WSS distribution. In particular it was shown that small-scale geometrical features, such as the cusp at the attachment site of the ligamentum arteriosum, introduced deviations in WSS of the same order of magnitude as flow-induced variations. Further, two Dean-type vortices were observed to form in the aortic arch. There, the computed WSS distribution exhibited significant spatial heterogeneity, reflecting the complexity of the blood flow. This result challenges the widespread assumption that the outer and inner aortic arch walls are exposed to high and low WSS respectively. The two Dean-type vortices formed in the aortic arch (along with an associated skewed axial velocity) were found to propagate along the descending thoracic aorta. The skewness of the axial velocity resulted in streaks of WSS. Since the distribution of atherosclerotic lesions in the rabbit descending aorta has also been reported to be streaked in nature, the results of this study provide further support for the hypothesis that flow mediates atherogenesis. Further, it was found that the local WSS patterns in the vicinity of the intercostal arteries (produced by the blood flow entering the vessels) are superimposed on the streaked macroscale WSS distribution. Such a diverse range of WSS environments in which branch pairs reside may explain variation in disease between branch pairs.

Lastly, NO production and transport was investigated within the same representation of the rabbit aorta and its branches. Vascular NO distribution was computed using the mathematical model of endothelial NO production proposed (Chapter 3), along with the blood flow field previously computed (Chapter 4). Endothelial NO distribution was found to exhibit significant spatial heterogeneity. Such heterogeneity reflected spatial variation in WSS (and hence NO production). However, it was found that certain geometrical features, such as arterial curvature and branching, also induced variations in NO concentration, independently of their effect on blood flow. Such a result is relevant, as the influence of the arterial geometry *per se* on NO transport was not considered in previous computational studies. Furthermore,

the effect of NO reaction within the vessel lumen was analysed in detail. It was concluded that mechanisms preventing NO consumption by haemoglobin must exist in order for NO to exert its vasodilation action. Two potential mechanisms were investigated: the existence of diffusional barriers and the formation of a RBC-free layer adjacent to the endothelium. It was estimated that diffusional barriers (if acting on their own) should act to reduce NO consumption rate by at least four orders of magnitude in order to allow physiologically realistic NO concentration levels. On the other hand, when a RBC-free layer is modelled, endothelial NO concentration is found to increase substantially regardless of the NO consumption rate outside the RBC-free layer (and hence regardless of the effect of the diffusional barriers).

This thesis showed correlations between blood flow metrics, vascular NO distribution and disease patterns. It is hoped that this study contributes to an enhanced understanding of the flow-dependent mechanisms that mediate atherogenesis. Further, this thesis highlights the significant effect of vascular geometry on blood flow and vascular transport, and hence further emphasises the need to generate detailed and faithful computational representations of the arterial system.

6.2 Future work

The possible extensions to this work are broad and numerous. This section outlines several suggestions for future studies.

6.2.1 Modelling nitric oxide transport within flow chambers

This thesis investigated NO production and transport within a parallel-plate flow chamber. The relationship between endothelial NO concentration and WSS within flow chambers was found to significantly depend on the form of the endothelial response to WSS. However, such a response remains quantitatively uncharacterised. Therefore, additional experimental work (considering the recommendations in this

thesis) is encouraged.

Further, the proposed model of endothelial NO production fails to take into account transient endothelial responses, such as a burst in NO production due to the onset of flow in the experiments. Future computational studies overcoming such a limitation would allow to predict NO distribution at the initial stage of the experiments (before the steady-state is reached).

Finally, the model proposed could be used to investigate NO distribution within different flow chambers and under different flow regimes. Such studies may potentially help identifying *a priori* suitable configurations (such as the chamber geometry and the flow regime) to achieve specific experimental goals.

6.2.2 Modelling blood flow within the arterial system

This thesis investigated blood flow dynamics within the rabbit aorta and its branches. Several aspects of the rabbit haemodynamics were simplified. In particular blood was assumed to be a Newtonian fluid, blood flow dynamics were assumed to be quasi-steady, and the arterial wall was assumed to be rigid and stationary. Future studies should aim to overcome the present limitations and thus investigate the effect of non-Newtonian blood, pulsatile flow and compliant walls. Further, the effect of varying flow splits (between aortic branches) and the inflow velocity profile at the aortic root needs further research.

Finally, future studies should investigate blood flow in multiple definitions of the rabbit aorta (obtained from different rabbits) in order to assess the effect of vascular geometry on flow metrics. In particular the effect of aortic torsion and tapering on the secondary motion should be further studied.

6.2.3 Modelling nitric oxide transport within the arterial system

This thesis investigated NO production and transport within the rabbit aorta and its branches numerically. To the author's knowledge, this is the first study investigating vascular NO dynamics within a realistic representation of a major artery. Therefore, the work presented should be understood as a first step towards more sophisticated multiscale model that should eventually overcome the present limitations.

In particular, future computational work should address NO convective transport (which was overlooked in this study), and investigate the effect of blood flow pulsatility and arterial compliance on vascular NO transport. Further, NO diffusion into the arterial wall should be considered, and a model of NO vasodilator action (considering NO signalling pathway in the arterial wall) should be proposed. Ultimately, NO-induced vasodilation should be coupled to the model of arterial wall distensibility by for example considering NO-dependent wall elastic properties.

Another possible extension of this work is to investigate NO transport in conjunction with other vascular species. NO interaction with oxygen is of particular interest, as red blood cells and other plasma constituents are postulated to release bound NO under hypoxic conditions.

Finally, the present study identified different aspects of NO production that require further experimental characterisation. In particular, the relationship between endothelial NO production and WSS and the endothelial response to dynamics changes in WSS remain unclear. Further, the existence of NO diffusional barriers *in vivo* and the formation of a RBC-free layer in the major arteries remain contentious. This thesis provides renewed motivation for further experimental work.

Bibliography

[1] *Cardiovascular diseases*. World Health Organization Fact sheet 317, 2007.

[2] H. Abu-Soud, K. Ichimori, A. Presta, and D.J. Stuehr. Electron transfer, oxygen binding, and nitric oxide feedback inhibition in endothelial nitric oxide synthase. *J. Biol. Chem*, (275):17349–17357, 200.

[3] R. Ajjan and P. J. Grant. Coagulation and atherothrombotic disease. *Atherosclerosis*, 186(2):240–259, 2006.

[4] B. W. Allen, J. S. Stamler, and C. A. Piantadosi. Hemoglobin, nitric oxide and molecular mechanisms of hypoxic vasodilation. *Trends in molecular medicine*, 15(10):452–460, 10 2009.

[5] N. Anitschkow. Über die veränderungen der kaninchenaorta bei experimenteller cholesterinsteatose. *Beitr Pathol Anat*, 56:379–404, 1913.

[6] G. Assmann and A. M. Gotto. Hdl cholesterol and protective factors in atherosclerosis. *Circulation*, 109:8–14, 2004.

[7] A. P. Avolio, M. F. O'rourke, K. Mang, P. T. Bason, and B. S. Gow. A comparative study of pulsatile arterial hemodynamics in rabbits and guinea pigs. *Am J Physiol*, 230(4):868–875, 4 1976.

[8] I. Azarov, K.T. Huang, S. Basu, M.T. Gladwin, N. Hogg, and D.B. Kim-Shapiro. Nitric oxide scavenging by red blood cells as a function of hematocrit and oxygenation. *J. Biol. Chem.*, 280(47):39024–39032, 2005.

[9] A. I. Barakat, R. P. Marini, and C. K. Colton. Measurement of flow rates through aortic branches in the anesthetized rabbit. *Lab Anim Sci*, 47(2):184–9, 1997.

[10] A. I. Barakat, P. A. Uhthoff, and C. K. Colton. Topographical mapping of sites of enhanced HRP permeability in the normal rabbit aorta. *J Biomech Eng*, 114(3):283–292, 1992.

[11] S. E. Barnes and P. D. Weinberg. Contrasting patterns of spontaneous aortic disease in young and old rabbits. *Arteriosclerosis, Thrombosis, and Vascular Biology*, 18(2):300–308, 1998.

[12] P. Barter. The role of HDL-cholesterol in preventing atherosclerotic disease. *European Heart Journal Supplements*, 7(suppl F):F4–F8, 2005.

[13] V. Berka, P. Chen, and A.L. Tsai. Spatial relationship between L-arginine and heme binding sites of endothelial nitric-oxide synthase. *J. Biol. Chem*, 271(271):33293–33300, 1996.

[14] Y. V. Bobryshev. Monocyte recruitment and foam cell formation in atherosclerosis. *Micron*, 37(3):208–222, 2006.

[15] Y. C. Boo, G. Sorescu, N. Boyd, I. Shiojima, K. Walsh, J. Du, and H. Jo. Shear stress stimulates phosphorylation of endothelial nitric-oxide synthase at Ser1179 by Akt-independent mechanisms. *Journal of Biological Chemistry*, 277(5):3388–3396, 02 2002.

[16] R. Busse and I. Fleming. Endothelial dysfunction in atherosclerosis. *Journal of Vascular Research*, 33(3):181–194, 1996.

[17] A. R. Butler, I. L. Megson, and P. G. Wright. Diffusion of nitric oxide and scavenging by blood in the vasculature. *Biochimica et Biophysica Acta (BBA) - General Subjects*, 1425(1):168–176, 1998.

[18] H. Cai and D. G. Harrison. Endothelial dysfunction in cardiovascular diseases: The role of oxidant stress. *Circulation Research*, 87(10):840–844, 2000.

[19] C. G. Caro, J. M. Fitz-Gerald, and R. C. Schroter. Arterial wall shear and distribution of early atheroma in man. *Nature*, 223(5211):1159–1160, 1969.

[20] C. G. Caro, J. M. Fitz-Gerald, and R. C. Schroter. Atheroma and arterial wall shear observation, correlation and proposal of a shear dependent mass transfer mechanism for atherogenesis. *Proceedings of the Royal Society of London. Series B, Biological Sciences*, 177(1046):109–133, 1971.

[21] C. G. Caro, T. J. Pedley, R. C. Schroter, and W. A. Seed. *The mechanics of circulation*. Oxford University Press, 1978.

[22] K. Chen, R. N. Pittman, and A. S. Popel. Nitric oxide in the vasculature where does it come from and where does it go? a quantitative perspective. *Antioxidants and Redox Signaling*, 10(7):1185–1198, 2008.

[23] K. Chen and A. S. Popel. Theoretical analysis of biochemical pathways of nitric oxide release from vascular endothelial cells. *Free Radical Biology and Medicine*, 41:668–680, 2006.

[24] C. Cheng, D. Tempel, A. Oostlander, F. Helderman, F. Gijsen, J. Wentzel, R. van Haperen, D. B. Haitsma, P. W. Serruys, A. F. W, van der Steen, R. de Crom, and R. Krams. Rapamycin modulates the eNOS vs. shear stress relationship. *Cardiovasc Res*, 78(1):123–129, 2008.

[25] C. Cheng, R. van Haperen, M. de Waard, L. C. A. van Damme, D. Tempel, L. Hanemaaijer, G. W. A. van Cappellen, J. Bos, C. J. Slager, D. J. Duncker, A. F. W. van der Steen, R. Crom, and R. Krams. Shear stress affects the intracellular distribution of enos: direct demonstration by a novel in vivo technique. *Blood*, 106(12):3691–3698, 2005.

[26] R. A. Cohen, K. M. Zitnay, C. C. Haudenschild, and L. D. Cunningham. Loss of selective endothelial cell vasoactive functions caused by hypercholesterolemia in pig coronary arteries. *Circulation Research*, 63(5):903–910, 1988.

[27] J. P. Cooke and V. J. Dzau. Nitric oxide synthase: Role in the genesis of vascular disease. *Annual Review of Medicine*, 48(1):489–509, 1997.

[28] G. Coppola, S. J. Sherwin, and J. Peiro. Nonlinear particle tracking for high-order elements. *Journal of Computational Physics*, 172(1):356–386, 9 2001.

[29] R. Courant, K. Friedrichs, and H. Lewy. On the partial difference equations of mathematical physics. *IBM J. Res. Dev.*, 11:215–234, March 1967.

[30] M. A. Creager, S. J. Gallagher, X. J. Girerd, S. M. Coleman, V. J. Dzau, and J. P. Cooke. L-arginine improves endothelium-dependent vasodilation in hypercholesterolemic humans. *The Journal of Clinical Investigation*, 90(4):1248–1253, 1992.

[31] K. S. Cunningham and A. I. Gotlieb. The role of shear stress in the pathogenesis of atherosclerosis. *Lab Invest*, 85(1):9–23, 2004.

[32] T. David. Wall shear stress modulation of ATP/ADP concentration at the endothelium. *Annals of Biomedical Engineering*, 31(10):1231–1237, 2003.

[33] J. Davigno and P. Ganz. Role of endothelial dysfunction in atherosclerosis. *Circulation*, 109(23):27–32, 2004.

[34] W. R. Dean. Note on the motion of fluid in a curved pipe. *Philosophical Magazine*, 20:208–223, 1927.

[35] P. A. Detmers, M. Hernandez, J. Mudgett, H. Hassing, C. Burton, S. Mundt, S. Chun, D. Fletcher, D. J. Card, J. M. Lisnock, R. Weikel, J. D. Bergstrom, D. E. Shevell, A. Hermanowski-Vosatka, C. P. Sparrow, Y. Chao, D. J. Rader, S. D. Wright, and E. Pure. Deficiency in inducible nitric oxide synthase results in reduced atherosclerosis in apolipoprotein E-deficient mice. *The Journal of Immunology*, 165(6):3430–3435, 2000.

[36] H. Drexler, A. M. Zeiher, K. Meinzer, and H. Just. Correction of endothelial dysfunction in coronary microcirculation of hypercholesterolaemic patients by L-arginine. *The Lancet*, 338(8782-8783):1546–1550, 1991.

[37] D. M. Dudzinski and T. Michel. Life history of eNOS: Partners and pathways. *Cardiovascular Research*, 75(2):247–260, 2007.

[38] K. Diem (editor). *Documenta Geigy, Scientzjic Tables*. Geigy Pharmaceuticals, Div. of Geigy Chemicals Corp, 1962.

[39] L. W. Ehrlich and M. H. Friedman. Steady convective diffusion in a bifurcation. *IEEE Transactions on Biomedical Engineering*, BME-24(1):12–18, 1977.

[40] A. Fadel, K. Barbee, and D. Jaron. A computational model of nitric oxide production and transport in a parallel plate flow chamber. *Ann Biomed Eng*, 37(5):943–954, 2009.

[41] S. Farthing. Flow in the thoracic aorta and its relation to atherogenesis. *PhD Thesis. University of Cambridge*, 1978.

[42] A. Feintuch, P. Ruengsakulrach, A. Lin, J. Zhang, Y. Zhou, J. Bishop, L. Davidson, D. Courtman, F. S. Foster, D. A. Steinman, R. M. Henkelman, and C. R. Ethier. Hemodynamics in the mouse aortic arch as assessed by mri, ultrasound, and numerical modeling. *AJP - Heart and Circulatory Physiology*, 292(2):H884–892, 2007.

[43] J. H. Ferziger and M. Peric. *Computational methods for fluid dynamics*. Springer-Verlag, 3rd edition, 2002.

[44] J. Fish and P. Marsden. Endothelial nitric oxide synthase: insight into cell-specific gene regulation in the vascular endothelium. *Cellular and Molecular Life Sciences*, 63(2):144–162, 2006.

[45] A. B. Fisher, S. Chien, A. I. Barakat, and R. M. Nerem. Endothelial cellular response to altered shear stress. *AJP - Lung Cellular and Molecular Physiology*, 281(3):L529–533, 2001.

[46] J. A. Frangos, T. Y. Huang, and C. B. Clark. Steady shear and step changes in shear stimulate endothelium via independent mechanism –superposition of transient and sustained nitric oxide production. *Biochemical and Biophysical Research Communications*, 224:660–665, 1996.

[47] D. L. Fry. Acute vascular endothelial changes associated with increased blood velocity gradients. *Circulation Research*, 22(2):165–197, 1968.

[48] R. F. Furchgott. Studies on relaxation of rabbit aorta by sodium nitrite: The basis for the proposal that acid-activable inhibitory factor from bovine retractor penis is organic nitrite and endothelium-derived relaxing factor is nitric oxide. *Vasodilation*, (401–414), 1988.

[49] R. F. Furchgott, F. Robert, and J. V. Zawadzki. The obligatory role of endothelial cells in the relaxation of arterial smooth muscle by acetylcholine. *Nature*, 288(5789):373–376, 1980.

[50] E. P. Garvey, J. V. Tuttle, K. Covington, B. M. Merrill, E. R. Wood, S. A. Baylis, and I. G. Charles. Purification and characterization of the constitutive nitric oxide synthase from human placenta. *Arch. Biochem. Biophys.*, (311):235–241, 1994.

[51] M. T. Gladwin and R. P. Patel. The role of red blood cells and hemoglobin nitric oxide interactions on blood flow. *American Journal of Respiratory Cell and Molecular Biology*, 38(2):125–126, 2008.

[52] W. J. Gordon and C. A. Hall. Transfinite element methods: Blending-function interpolation over arbitrary curved element domains. *Numerische Mathematik*, 21(2):109–129, 1973.

[53] A. C. Gorren and B. Mayer. Tetrahydrobiopterin in nitric oxide synthesis: a novel biological role for pteridines. *Curr. Drug Metab.*, 3(133-157), 2002.

[54] L. Grinberg and G. E. Karniadakis. A new domain decomposition method with overlapping patches for ultrascale simulations: Application to biological flows. *Journal of Computational Physics*, 229(15):5541–5563, 2010.

[55] I. M. Grumbach, C. C. Wei, S. A. Mertens, and D. G. Harrison. A negative feedback mechanism involving nitric oxide and nuclear factor kappa-b modulates endothelial nitric oxide synthase transcription. *Journal of Molecular and Cellular Cardiology*, 39(4):595–603, 2005.

[56] T. S. Hakim, K. Sugimori, E. M. Camporesi, and G. Anderson. Half-life of nitric oxide in aqueous solutions with and without haemoglobin. *Physiol Meas.*, 17(4):267–277, 1996.

[57] H. A. Himburg, D. M. Grzybowski, A. Hazel, J. A. LaMack, X. Li, and M. H. Friedman. Spatial comparison between wall shear stress measures and porcine arterial endothelial permeability. *AJP - Heart and Circulatory Physiology*, 286(5):H1916–1922, 2004.

[58] Y. Huo, X. Guo, and G. Kassab. The flow field along the entire length of mouse aorta and primary branches. *Annals of Biomedical Engineering*, 36(5):685–699, 2008.

[59] L. J. Ignarro, R. E. Byrns, G. M. Buga, and K. S. Wood. Endothelium-derived relaxing factor from pulmonary artery and vein possesses pharmacologic and chemical properties identical to those of nitric oxide radical. *Circulation Research*, 61(6):866–879, 1987.

[60] S. Jalali, Y. Li, M. Sotoudeh, S. Yuan, S. Li, S. Chien, and J. Shyy. Shear stress activates p60src-Ras-MAPK signaling pathways in vascular endothelial cells. *Arteriosclerosis, Thrombosis, and Vascular Biology*, 18(2):227–234, 1998.

[61] J. Jeong and F. Hussain. On the identification of a vortex. *Journal of Fluid Mechanics*, 285(1):69–94, 1995.

[62] H. Jo, K. Sipos, Y. Go, R. Law, J. Rong, and J. M. McDonald. Differential effect of shear stress on extracellular signal-regulated kinase and N-terminal Jun kinase in endothelial cells. *Journal of Biological Chemistry*, 272(2):1395–1401, 1997.

[63] M. A. Gimbrone Jr. Vascular endothelium, hemodynamic forces, and atherogenesis. *American Journal of Pathology*, 155(1):1–5, 1999.

[64] M. R. Kaazempur-Mofrad and C. R. Ethier. Mass transport in an anatomically realistic human right coronary artery. *Annals of Biomedical Engineering*, 29(2):121–127, 2001.

[65] A. J. Kanai, H. C. Strauss, G. A. Truskey, A. L. Crews, S. Grunfeld, and T. Malinski. Shear stress induces ATP-independent transient nitric oxide release from vascular endothelial cells, measured directly with a porphyrinic microsensor. *Circ Res*, 77(2):284–293, 1995.

[66] W. B. Kannel, T. R. Dawber, A. Kagan, N. Revotskie, and J. Stokes. Risk factors in the development of coronary heart disease. six year follow-up experience the framingham study. *Annals of Internal Medicine*, 54(5):1035–1035, 1961.

[67] G. E. Karniadakis, M. Israeli, and S. A. Orszag. High-order splitting methods for the incompressible navier-stokes equations. *Journal of Computational Physics*, 97(2):414–443, 1991.

[68] A. Kazakidi, S. J. Sherwin, and P. D. Weinberg. Effect of reynolds number and flow division on patterns of haemodynamic wall shear stress near branch points in the descending thoracic aorta. *Journal of The Royal Society Interface*, 6(35):539–548, 2009.

[69] J. F. Keaney and J. A. Vita. Atherosclerosis, oxidative stress, and antioxidant protection in endothelium-derived relaxing factor action. *Progress in Cardiovascular Diseases*, 38(2):129–154, 1995.

[70] M. Kelm. Nitric oxide metabolism and breakdown. *Biochim Biophys Acta*, 1999.

[71] T. Kenner, H. Leopold, and H. Hinghofer-Szalkay. The continuous high-precision measurement of the density of flowing blood. *Pflgers Archiv European Journal of Physiology*, 370(1):25–29, 1977.

[72] V. G. Kharitonov, A. R. Sundquist, and V. S. Sharma. Kinetics of nitric oxide autoxidation in aqueous solution. *J Biol Chem*, 8(269):5881–5883, 1994.

[73] S. Kim, P. K. Ong, O. Yalcin, M. Intaglietta, and P. C. Johnson. The cell-free layer in microvascular blood flow. *Biorheology*, 46(3):181–189, 2009.

[74] D. B. Kim-Shapiro, A. N. Schechter, and M. T. Gladwin. Unraveling the reactions of nitric oxide, nitrite, and hemoglobin in physiology and therapeutics. *Arteriosclerosis, Thrombosis, and Vascular Biology*, 26(4):697–705, 2006.

[75] S. Klahr. The role of nitric oxide in hypertension and renal disease progression. *Nephrology Dialysis Transplantation*, 16(suppl 1):60–62, 2001.

[76] D. N. Ku, D. P. Giddens, C. K. Zarins, and S. Glagov. Pulsatile flow and atherosclerosis in the human carotid bifurcation. positive correlation between plaque location and low oscillating shear stress. *Arteriosclerosis, Thrombosis, and Vascular Biology*, 5(3):293–302, 1985.

[77] K. E. Lee, K. H. Parker, C. G. Caro, and S. J. Sherwin. The spectral/hp element modelling of steady flow in non-planar double bends. *International Journal for Numerical Methods in Fluids*, 57(5):519–529, 2008.

[78] R. S. Lewis and W. M. Deen. Kinetics of the reaction of nitric oxide with oxygen in aqueous solutions. *Chemical Research in Toxicology*, 7(4):568–574, 2002.

[79] Peter Libby. Inflammation in atherosclerosis. *Nature*, 420(6917):868–874, 2002.

[80] Peter Libby. What happens inside an atherosclerotic plaque? *International Congress Series*, 1262:253–256, 2004. Atherosclerosis XIII. Proceedings of the 13th International Atherosclerosis Symposium.

[81] J. Liu, G. Garcia-Cardena, and W. C. Sessa. Palmitoylation of endothelial nitric oxide synthase is necessary for optimal stimulated release of nitric oxide: implications for cavaloe localization. *Biochemistry*, (35):13277–13281, 1996.

[82] X. Liu, Y. Fan, and X. Deng. Effect of spiral flow on the transport of oxygen in the aorta: A numerical study. *Annals of Biomedical Engineering*, 38(3):917–926, 2010.

[83] X. Liu, F. Pu, Y. Fan, X. Deng, D. Li, and S. AdakLi. A numerical study on the flow of blood and the transport of LDL in the human aorta: the physiological significance of the helical flow in the aortic arch. *AJP - Heart and Circulatory Physiology*, 297(1):H163–170, 2009.

[84] X. Liu, P. Srinivasan, E. Collard, P. Grajdeanu, J. L. Zweier, and A. Friedman. Nitric oxide diffusion rate is reduced in the aortic wall. *Biophysical journal*, 94(5):1880–1889, 2008.

[85] J. Lobstein. *Traité d'Anatomie Pathologique*, volume 2. Levrault, 1833.

[86] J. Loscalzo. Endothelium, nitric oxide, and atherosclerosis: From basic mechanisms to clinical implications. *Circulation*, 102(8):102:e51, 2000.

[87] B. P. Luchsinger, E. N. Rich, A. J. Gow, E. M. Williams, J. S. Stamler, and D. J. Singel. Routes to S-nitroso-hemoglobin formation with heme redox and preferential reactivity in the subunits. *Proceedings of the National Academy of Sciences of the United States of America*, 100(2):461–466, 2003.

[88] P. Ma, X. Li, and D. N. Ku. Convective mass transfer at the carotid bifurcation. *Journal of Biomechanics*, 30(6):565–571, 1997.

[89] A. M. Malek, S. L. Alper, and S. Izumo. Hemodynamic shear stress and its role in atherosclerosis. *JAMA*, 282(21):2035–2042, 1999.

[90] T. Malinski, Z. Taha, S. Grunfeld, M. Kapturczak S. Patton, and P. Tomboulian. Diffusion of nitric oxide in the aorta wall monitored in situ by porphyrinic microsensors. *Biochem. Biophys. Res. Commun.*, 193(365-375), 1993.

[91] S. Marchal, A. C. Gorren, M. Sorlie, K. K. Andersson, B. Mayer, and R. Lange. Evidence of two distinct oxygen complexes of reduced endothelial nitric oxide synthase. *J. Biol. Chem*, (279):19824–19831, 2004.

[92] S. Moncada and E. A. Higgs. Endogenous nitric oxide: physiology, pathology and clinical relevance. *Eur J Clin Invest*, 21(4):361–374, 1991.

[93] S. Moncada and E. A. Higgs. Nitric oxide and the vascular endothelium. *Handb Exp Pharmacol*, 176:213–254, 2006.

[94] C. D. Murray. The physiological principle of minimum work. i. the vascular system and the cost of blood volume. *Proceedings of the National Academy of Sciences of the United States of America*, 12(3):207–214, 1926.

[95] J. G Myers, J. A. Moore, M. Ojha, K. W. Johnston, and C. R. Ethier. Factors influencing blood flow patterns in the human right coronary artery. *Annals of Biomedical Engineering*, 29(2):109–120, 2001.

[96] P. D. Christofides N. H. El-Farra and J. C. Liao. Computational modeling of nitric oxide transport and consumption in blood vessels. *Proceedings of the 41st IEEE Conference on Decision and Control*, pages 2518–2523, 2002.

[97] T. Nagano. Practical methods for detection of nitric oxide. *Luminescence*, 14(6):283–290, 1999.

[98] N. Nakatsubo, H. Kojima, K. Kikuchi, H. Nagoshi, Y. Hirata, D. Maeda, Y. Imai, T. Irimura, and T. Nagano. Direct evidence of nitric oxide production from bovine aortic endothelial cells using new fluorescence indicators: diaminofluoresceins. *FEBS Letters*, 427(2):263–266, 1998.

[99] C. Napoli and L. J. Ignarro. Nitric oxide and atherosclerosis. *Nitric Oxide*, 5(2):88–97, 2001.

[100] M. Navab, J. A. Berliner, G. Subbanagounder, S. Hama, A. J. Lusis, L. W. Castellani, S. Reddy, D. Shih, W. Shi, A. D. Watson, B. J. Van Lenten, D. Vora, and A. M. Fogelman. Hdl and the inflammatory response induced by ldl-derived oxidized phospholipids. *Arterioscler Thromb Vasc Biol*, 21(4):481–488, 2001.

[101] A. N. Nicolaides. The genesis of atherosclerosis and risk factors: A review. *Angiology*, 52(2):89–98, 2001.

[102] R. L. Ohsfeldt, S. K. Gandhi, K. M. Fox, M. F. Bullano, and M. Davidson. Medical and cost burden of atherosclerosis among patients treated in routine clinical practice. *Journal of Medical Economics*, 13(3):500–507, 2010.

[103] R. M. J. Palmer, A. G. Ferrige, and S. Moncada. Nitric oxide release accounts for the biological activity of endothelium-derived relaxing factor. *Nature*, 327(6122):524–526, 1987.

[104] K. Panda, S. Adak, D. Konas, M. Sharma, and D.J. Stuehr. A conserved aspartate (Asp -1393) regulates NADPH reduction of neuronal nitric-oxide synthase: implications for catalysis. *J. Biol. Chem*, (279):18323–1833, 2004.

[105] R. P. Patel, D. Moellering, J. Murphy-Ullrich, H. Jo, J. S. Beckman, and V. M. Darley-Usmar. Cell signaling by reactive nitrogen and oxygen species in atherosclerosis. *Free Radical Biology and Medicine*, 28(12):1780 – 1794, 2000.

[106] K. Perktold and D. Hilbert. Numerical simulation of pulsatile flow in a carotid bifurcation model. *Journal of Biomedical Engineering*, 8(3):193–199, 1986.

[107] K. Perktold and M. Resch. Numerical flow studies in human carotid artery bifurcations: basic discussion of the geometric factor in atherogenesis. *Journal of Biomedical Engineering*, 12(2):111–123, 1990.

[108] M. J. Plank, D. J. Wall, and T. David. The role of endothelial calcium and nitric oxide in the localisation of atherosclerosis. *Math Biosci*, 207(1):26–39, 2007.

[109] R. F. Probstein. *Physicochemical Hydrodynamics: An Introduction.* John Wiley and Sons Inc., 2003.

[110] W. Qiu, D. A. Kass, Q. Hu, and R. C. Ziegelstein. Determinants of shear stress-stimulated endothelial nitric oxide production assessed in real-time by 4,5-diaminofluorescein fluorescence. *Biochemical and Biophysical Research Communications*, 286(2):328–335, 2001.

[111] E. W. Raines and N. Ferri. Thematic review series: The immune system and atherogenesis. cytokines affecting endothelial and smooth muscle cells in vascular disease. *Journal of Lipid Research*, 46(6):1081–1092, 2005.

[112] G. Rappitsch and K. Perktold. Computer simulation of convective diffusion processes in large arteries. *Journal of Biomechanics*, 29(2):207–215, 1996.

[113] U. Rauch, J. I. Osende, V. Fuster, J. J. Badimon, Z. Fayad, and J. H. Chesebro. Thrombus formation on atherosclerotic plaques: Pathogenesis and clinical consequences. *Annals of Internal Medicine*, 134(3):224–238, 2001.

[114] M. A. Reidy and B. L. Langille. The effect of local blood flow patterns on endothelial cell morphology. *Experimental and Molecular Pathology*, 32(3):276–289, 1980.

[115] A. Rengasamy and R.A. Johns. Determination of Km for oxygen of nitric oxide synthase isoforms. *J. Pharmaco. Exp. Ther.*, (276):30–33, 1996.

[116] E. Rindfleisch. *A Textbook of Pathologic Histology.* Lindsay and Blakiston, 1872.

[117] C. Rokitansky. *A manual of pathological anatomy.* Blanchard and Lea, 1855.

[118] G. Rose. Epidemiology of atherosclerosis. *BMJ: British Medical Journal*, 303(6816):1537–1539, 1991.

[119] R. Ross. The pathogenesis of atherosclerosis: a perspective for the 1990s. *Nature*, 362(6423):801–809, 1993.

[120] R. Ross and J. A. Glomset. Atherosclerosis and the arterial smooth muscle cell. *Science*, 180(4093):1332–1339, 1973.

[121] J. Santolini, S. Adak, and D. J. Stuehr. Differences in three kinetic parameters underpin the unique catalytic profiles of nitric oxide synthases i, ii, and iii. *J. Biol. Chem*, (276):48887–48898, 2001.

[122] H. Scharfstein, W. H. Gutstein, and L. Lewis. Changes of boundary layer flow in model systems: Implications for initiation of endothelial injury. *Circulation Research*, 13(6):580–584, 1963.

[123] A. N. Schechter and M. T. Gladwin. Hemoglobin and the paracrine and endocrine functions of nitric oxide. *New England Journal of Medicine*, 348(15):1483–1485, 2003.

[124] D. M. Schrijvers, G. R. Y. De Meyer, A. G. Herman, and W. Martinet. Phagocytosis in atherosclerosis: Molecular mechanisms and implications for plaque progression and stability. *Cardiovascular Research*, 73(3):470–480, 2007.

[125] C. J. Schwartz, A. J. Valente, and E. A. Sprague. A modern view of atherogenesis. *The American Journal of Cardiology*, 71(6):B9–B14, 1993.

[126] A. K. Shaaban and A. J. Duerinckx. Wall shear stress and early atherosclerosis: A review. *American Journal of Roentgenology*, 174(6):1657–1665, 2000.

[127] N. Shahcheraghi, H. A. Dwyer, A. Y. Cheer, A. I. Barakat, and T. Rutaganira. Unsteady and three-dimensional simulation of blood flow in the human aortic arch. *J Biomech Eng*, 124(4):378–87, 2002.

[128] J. Shen, M. A. Gimbrone Jr, F. W. Luscinskas, and C. F. Dewey Jr. Regulation of adenine nucleotide concentration at endothelium-fluid interface by viscous shear flow. *Biophysical Journal*, 64(4):1323–1330, 1993.

[129] S. J. Sherwin and G. Karniakadis. Spectral/hp element methods for computational fluid dynamics. *Oxford University Press*, 2005.

[130] S. J. Sherwin and J. Peiro. Mesh generation in curvilinear domains using high-order elements. *International Journal for Numerical Methods in Engineering*, 53(1):207–223, 2002.

[131] H. Shimokawa. Primary endothelial dysfunction: Atherosclerosis. *Journal of Molecular and Cellular Cardiology*, 31(1):23–37, 1999.

[132] D. J. Singel and J. S. Stamler. Blood traffic control. *Nature*, 430(6997):297–297, 2004.

[133] C. R. Smith and J. D. A. Walker. Vortex interactions with walls. *Annu. Rev. Fluid Mech.*, (26):573–616, 1994.

[134] K. M. Smith, L. C. Moore, and H. E. Layton. Advective transport of nitric oxide in a mathematical model of the afferent arteriole. *Am J Physiol Renal Physiol*, 284(5):1080–1096, 2003.

[135] P. Sonveaux, I. I. Lobysheva, O. Feron, and T. J. McMahon. Transport and peripheral bioactivities of nitrogen oxides carried by red blood cell hemoglobin: Role in oxygen delivery. *Physiology*, 22(2):97–112, 2007.

[136] J. S. Stamler, O. Jaraki, J. Osborne, D. I. Simon, J. Keaney, J. Vita, D. Singel, C. R. Valeri, and J. Loscalzo. Nitric oxide circulates in mammalian plasma primarily as an S-nitroso adduct of serum albumin. *Proceedings of the National Academy of Sciences of the United States of America*, 89(16):7674–7677, 1992.

[137] G. Stoll and M. Bendszus. Inflammation and atherosclerosis: Novel insights into plaque formation and destabilization. *Stroke*, 37(7):1923–1932, 2006.

[138] J. Suo, D. E. Ferrara, D. Sorescu, R. E. Guldberg, W. R. Taylor, and D. P. Giddens. Hemodynamic shear stresses in mouse aortas: Implications for atherogenesis. *Arteriosclerosis, Thrombosis, and Vascular Biology*, 27(2):346–351, 2007.

[139] P. N. Tandon and U. V. S. Rana. A new model for blood flow through an artery with axisymmetric stenosis. *International Journal of Bio-Medical Computing*, 38(3):257–267, 1995.

[140] C. A. Taylor and C. A. Figueroa. Patient-specific modeling of cardiovascular mechanics. *Annual Review of Biomedical Engineering*, 11(1):109–134, 2009.

[141] A. Tedgui and M. J. Lever. Filtration through damaged and undamaged rabbit thoracic aorta. *AJP - Heart and Circulatory Physiology*, 247(5):784–791, 1984.

[142] O. Traub and B.C. Berk. Laminar shear stress : Mechanisms by which endothelial cells transduce an atheroprotective force. *Arteriosclerosis, Thrombosis, and Vascular Biology*, 18(5):677–685, 1998.

[143] P. Vallance and N. Chan. Endothelial function and nitric oxide: clinical relevance. *Heart*, 85(3):342–350, 2001.

[144] M. W. Vaughn, L. Kuo, and J. C. Liao. Effective diffusion distance of nitric oxide in the microcirculation. *AJP - Heart and Circulatory Physiology*, 274:1705–1714, 1998.

[145] M. W. Vaughn, L. Kuo, and J. C. Liao. Estimation of nitric oxide production and reaction rates in tissue by use of a mathematical model. *AJP - Heart and Circulatory Physiology*, (274):2163–2176, 1998.

[146] R. Virchow. *Cellular pathology as based upon physiological and pathological histology.* JB Pippincott, 1871.

[147] P. Volino and N. M. Thalmann. The SPHERIGON: a simple polygon patch for smoothing quickly your polygonal meshes. *Computer Animation 98. Proceedings*, pages 72–78, 1998.

[148] N. Vukosavljevic, D. Jaron, K. A. Barbee, D. Buerk, and G. Donald. Quantifying the L-arginine paradox in vivo. *Microvasc Res*, 71(1):48–54, 2006.

[149] C. C. Wei, Z.Q. Wang, D. Durra, C. Hemann, R. Hille, E. D. Garcin, E. D. Getzoff, and D. J. Stuehr. The three nitric oxide synthases differ in their kinetics of tetrahydroxylation. *J. Biol. Chem*, (280):8929–8935, 2005.

[150] C. R. White and J. A. Frangos. The shear stress of it all: the cell membrane and mechanochemical transduction. *Phil. Trans. R. Soc. B*, 362:1459–1467, 2007.

[151] T. F. Wiesner, B. C. Berk, and R. M. Nerem. A mathematical model of the cytosolic-free calcium response in endothelial cells to fluid shear stress. *Proc Natl Acad Sci U S A*, 94(8):3726–3731, 1997.

[152] U. Windberger, A. Bartholovitsch, R. Plasenzotti, K. J. Korak, and G. Heinze. Whole blood viscosity, plasma viscosity and erythrocyte aggregation in nine mammalian species: reference values and comparison of data. *Experimental Physiology*, 88(3):431–440, 2003.

[153] D. A. Wink, J. F. Darbyshire, R. W. Nims, J. E. Saavedra, and P. C. Ford. Reactions of the bioregulatory agent nitric oxide in oxygenated aqueous media: Determination of the kinetics for oxidation and nitrosation by intermediates generated in the nitric oxide/oxygen reaction. *Chemical Research in Toxicology*, 6(1):23–27, 2002.

[154] G. Wu and Jr. S. M. Morris. Arginine metabolism: nitric oxide and beyond. *Biochem, J*, (336):1–17, 1998.

[155] www.ibidi.de. Slide vi.

[156] www.nektar.info.

[157] D. G. Xie. Torsion effect on secondary flow in a helical pipe. *International Journal of Heat and Fluid Flow*, 11(2):114–119, 1990.

[158] K. Yamamoto, T. Sokabe, T. Matsumoto, K. Yoshimura, M. Shibata, N. Ohura, T. Fukuda, T. Sato, K. Sekine, S. Kato, M. Isshiki, T. Fujita, M. Kobayashi, K. Kawamura, H. Masuda, A. Kamiya, and J. Ando. Impaired flow-dependent control of vascular tone and remodeling in P2X4-deficient mice. *Nat Med*, 12(1):133–137, 2006.

[159] O. E. Zaikina, V. V. Dolgov, V. N. Ivanov, M. F. Bondarenko, and V. S. Repin. Quantitative SEM analysis of injury to the endothelium of rabbit aorta and carotid artery during experimental atherosclerosis. *Atherosclerosis*, 41(2):141–154, 1982.

Appendix A

Vascular Nitric Oxide Synthesis

This section describes the signalling pathway that leads to endothelial NO production. Two models of endothelial NO synthesis proposed by Chen *et al.* [23] (a kinetic and a simplified model) are analysed in detail. It is concluded that, for the purpose of this thesis, the simplified model is sufficient to accurately model vascular NO production.

A.1 Overview

Nitric oxide (NO) is produced at the endothelium by the oxidation of L-arginine to L-citrulline and NO in the presence of tetrahydrobiopterin (BH_4), reduced nicotinamide adenine dinucleotide phosphate (NADPH) and oxygen. The reaction is catalyzed by the enzymatic action of endothelial NO synthase (eNOS) and can be described by the following chemical equation [27]:

$$\text{L-arginine} + O_2 + 1.5NADPH \xrightarrow{eNOS} \text{L-Citrulline} + NO + 1.5NADP^+ + 2H_2O.$$

Despite the apparent simplicity of this equation, the kinetic pathway that leads to NO synthesis consists of a complex metabolic network. In fact, endothelial NO

production rate depends on a great number of parameters, specifically on the concentration of several co-enzymes and on substrate availability within the endothelial cell. In order to gain understanding of endothelial NO production, several computational studies have modelled the NO synthesis pathway. In this appendix, the kinetic model proposed by Chen *et al.* [27] is analyzed.

A.2 Kinetic model of endothelial NO synthesis

The model proposed in [23] improved previous efforts by incorporating the effect of L-arginine and oxygen concentration on NO production rate. The model was constructed under the following hypotheses:

- NO production rates are calculated under two different assumptions: 1)NO production occurs in the compartment adjacent to the endothelial cell surface. This assumption relies on the fact that approximately 70% of eNOS is confined in this compartment, and 2)NO is produced throughout the cell. It is shown that the computed NO production rates for both cases are almost equal. Therefore, eNOS is assumed to reside mainly in the membrane compartments.

- All the co-enzymes involved in NO synthesis are present in excess. This hypothesis is true for BH_4 and calmodulin, as their typical intracellular concentrations are significantly higher than those required by the NO synthesis process. However, Ca^{2+} concentration can be insufficient to catalyze certain chemical reactions, and this effect is not considered in this model.

- L-arginine concentration remains constant within the endothelial cell ($\frac{d[Arg]}{dt} = 0$). This assumption implies that the rate of consumption of L-arginine within the endothelial cell is equal to the rate of L-arginine supply from external sources (represented by the term S in Eq. A-1).

- Reactions involving changes in oxygen and its transport from the blood to the endothelial cell are neglected. This hypothesis is based on the fact that

oxygen concentration is significantly larger than eNOS concentration under physiological conditions. This hypothesis should be revised under pathological conditions, where the supply of oxygen may be limited.

It is important to highlight that this thesis does not aim to study the intracellular reactions that lead to NO synthesis. However, a basic understanding of such process is necessary in order to accurately model NO production in the vasculature.

The kinetic model proposed by Chen *et al.* [23] is shown next. The different states of eNOS are represented by the iron heme group, while Arg and NOHA represents L-arginine and N^{ω}-hydroxyl-L-arginine (an intermediate product) respectively. Bindings between species are represented with a dot (e.g. $Fe \cdot Arg$).

$$\begin{aligned}\frac{d[Arg]}{dt} &= -k_1[Arg][Fe^{3+}] + k_1^{'}[Fe^{3+} \cdot Arg] \\ &\quad -k_4[Arg][Fe^{2+}] + k_4^{'}[Fe^{2+} \cdot Arg] + S \\ &\quad = 0,\end{aligned} \tag{A-1}$$

$$\begin{aligned}\frac{d[Fe^{3+}]}{dt} &= -k_1[Arg][Fe^{3+}] + k_1^{'}[Fe^{3+} \cdot Arg] - k_2[Fe^{3+}] \\ &\quad +k_{14}[Fe^{3+}NO] + k_{13}[Fe^{2+}NO][O_2] \\ &\quad +k_8[Fe^{3+} \cdot NOHA] - k_8^{'}[Fe^{3+}][NOHA],\end{aligned} \tag{A-2}$$

$$\begin{aligned}\frac{d[Fe^{3+} \cdot Arg]}{dt} &= k_1[Fe^{3+}][Arg] - k_1^{'}[Fe^{3+} \cdot Arg] \\ &\quad -k_3[Fe^{3+} \cdot Arg],\end{aligned} \tag{A-3}$$

$$\begin{aligned}\frac{d[Fe^{2+}]}{dt} &= k_2[Fe^{3+}] - k_4^{'}[Fe^{2+} \cdot Arg] + k_4[Fe^{2+}][Arg] \\ &\quad +k_9[Fe^{2+} \cdot NOHA] - k_9^{'}[Fe^{2+}][NOHA],\end{aligned} \tag{A-4}$$

$$\begin{aligned}\frac{d[Fe^{2+}Arg]}{dt} &= k_3[Fe^{3+} \cdot Arg] + k_4[Fe^{2+}][Arg] \\ &\quad -k_4^{'}[Fe^{2+} \cdot Arg] - k_5[Fe^{2+} \cdot Arg][O_2] \\ &\quad +k_5^{'}[Fe^{3+}O_2^{-} \cdot Arg],\end{aligned} \tag{A-5}$$

$$\frac{d[Fe^{3+}O_2^- \cdot Arg]}{dt} = k_5[Fe^{2+} \cdot Arg][O_2] - k_6[Fe^{3+}O_2^- \cdot Arg] - k_5^{'}[Fe^{3+}O_2^- \cdot Arg], \quad \text{(A-6)}$$

$$\frac{d[Fe^{3+} \cdot NOHA]}{dt} = k_6[Fe^{3+}O_2^- \cdot Arg] - k_7[Fe^{3+} \cdot NOHA] - k_8^{[}Fe^{3+} \cdot NOHA] + k_8^{'}[Fe^{3+}][NOHA], \quad \text{(A-7)}$$

$$\frac{d[Fe^{2+} \cdot NOHA]}{dt} = +k_7[Fe^{3+}NOHA] - k_{10}[Fe^{2+} \cdot NOHA][O_2] - k_10^{[}Fe^{3+}O_2^- \cdot NOHA] - k_9^{[}Fe^{2+} \cdot NOHA] + k_9^{'}[Fe^{2+}][NOHA], \quad \text{(A-8)}$$

$$\frac{d[Fe^{3+}O_2^- \cdot NOHA]}{dt} = +k_{10}[Fe^{2+} \cdot NOHA][O_2] - k_{11}[Fe^{3+}O_2^- \cdot NOHA] - k_{10}^{'}[Fe^{3+}O_2^- \cdot NOHA], \quad \text{(A-9)}$$

$$\frac{d[Fe^{3+}NO]}{dt} = +k_{11}[Fe^{3+}O_2^- \cdot NOHA] - k_{14}[Fe^{3+}NO] - k_{12}[Fe^{3+}NO], \quad \text{(A-10)}$$

$$\frac{d[Fe^{2+}NO]}{dt} = +k_{12}[Fe^{3+}NO] - k_{13}[Fe^{2+}NO][O_2], \quad \text{(A-11)}$$

$$\frac{d[NO]}{dt} = k_{14}[Fe^{3+}NO], \quad \text{(A-12)}$$

$$\frac{d[Citrulline]}{dt} = k_{11}[Fe^{3+}O_2^- \cdot NOHA], \quad \text{(A-13)}$$

$$\frac{d[NO_3^-]}{dt} = +k_{13}[Fe^{2+}NO][O_2], \quad \text{(A-14)}$$

$$\frac{[NOHA]}{dt} = +k_8[Fe^{3+} \cdot NOHA] - k_8[Fe^{3+}][NOHA] - k_9[Fe^{2+} \cdot NOHA] - k_9^{'}[Fe^{2+}][NOHA]. \quad \text{(A-15)}$$

A thorough literature search to obtain values for the kinetic parameters was undertaken by Chen *et al.* [23]. Table A.1 shows the values proposed in [23] for the

kinetic rate constants involved in Eqs. A-1 - A-15. The scaled coefficients at 37°C were obtained applying the Arrhenius equation.

Coefficient	Literature	Values (37°C)	Unit	References
k_1	0-0.2 (4°C) 0-0.8 (23 °C)	0.1	$\mu M^{-1}s^{-1}$	[13]
$k_1{}'$	0-0.08 (4°C) 0-1.6 (23 °C)	0.1	s^{-1}	[13]
k_2	0.11 (10°C)	0.91	s^{-1}	[121]
k_3	0.11 (10°C)	0.91	s^{-1}	[121]
k_4	0-0.2 (4°C) 0-0.8 (23 °C)	1.89	$\mu M^{-1}s^{-1}$	[13]
$k_4^{'}$	0-0.08 (4°C) 0-1.6 (23 °C)	11.4	s^{-1}	[13]
k_5	0.265 (7°C) 0.34 (10 °C)	2.58	$\mu M^{-1}s^{-1}$	[2, 91]
$k_5^{'}$	24 (7°C) 28 (10 °C)	98	s^{-1}	[2, 91]
k_6	6.2 (7°C) 6.7 (10 °C)	12.6	s^{-1}	[149, 91]
k_7	0.11 (10 °C)	0.91	s^{-1}	[121]
k_8	0-0.2 (4°C) 0-0.8 (23 °C)	0.1	s^{-1}	[53, 104]
$k_8^{'}$	0-0.08 (4°C) 0-1.6 (23 °C)	0.1	$\mu M^{-1}s^{-1}$	[53, 104]
k_9	0-0.2 (4°C) 0-0.8 (23 °C)	11.4	s^{-1}	[53, 104]
$k_9^{'}$	0-0.08 (4°C) 0-1.6 (23 °C)	1.89	$\mu M^{-1}s^{-1}$	[53, 104]
k_{10}	0.342 (7°C) 0.26 (10 °C)	3.33	$\mu M^{-1}s^{-1}$	[2, 91]
$k_{10}^{'}$	22 (7°C) 18 (10 °C)	89.9	s^{-1}	[121, 91]
k_{11}	14.5 (7°C)	29.4	s^{-1}	[91]
k_{12}	0.11 (10°C)	0.91	s^{-1}	[121]
k_{13}	0.00429 (10°C)	0.033	$\mu M^{-1}s^{-1}$	[121]
k_{14}	2.5 (7°C) 3.5 (10 °C)	53.9	s^{-1}	[121, 91]

Table A.1: Kinetic constants that regulate endothelial nitric oxide synthesis

A.2.1 Conclusions of the model

The previous system of ordinary differential Eqs. A-1 - A-15 can be solved numerically. The results and conclusions obtained by Chen *et al.* are detailed in this

section.

A.2.2 Transient NO production

The system given by Eqs. A-1 - A-15 evolves into a quasi-steady state –where NO production rate is effectively constant– within seconds. Given the short duration of the transient, it can be assumed that eNOS activation leads instantaneously to a sustained production of NO.

A.2.3 Dependence on eNOS

The system was solved for different levels of eNOS concentration within the cell. The results show that there is a linear relationship between eNOS concentration and NO production rate under physiological conditions (all the substrates and co-enzymes are present in excess). Enzymology predicts the same result, as the product formation is linearly dependent on the enzyme concentration.

A.2.4 Dependence on L-arginine

Intracellular concentration of L-arginine has been shown experimentally to be significantly higher ($\sim 100\mu M$) than that required by eNOS to reach 50% maximal activity ($\sim 3\mu M$). Accordingly, further availability of L-arginine should not enhance NO production. However, several *in vitro* studies [148] have reported increased NO production due to increased L-arginine uptake by endothelial cells. One plausible explanation for this paradox (commonly referred to as the "*L-arginine paradox*") is that L-arginine may be distributed in *"pools"* or compartments, and despite an overall high concentration within the cell, eNOS can only access the L-arginine contained within compartments associated with the cell membrane.

The theoretical model by Chen *et al.* [23] shows that NO production is only affected

in cases where L-arginine concentration is $\sim 5\mu$M. As stated before, intracellular L-arginine concentration is on the order of $100\mu M$. Therefore, only if the percentage of L-arginine accessible to eNOS was very low ($< 5\%$), would supplemental intake of L-arginine enhance NO production.

A.2.5 Dependence on oxygen

In large arterial vessels under physiological conditions, oxygen concentration in plasma is sufficient to activate eNOS action. However, the theoretical model shows that a significant reduction in oxygen availability (hypoxia) causes the NO production rate to fall. This result is consistent with various *in vivo* experiments, which have reported a correlation between chronic intermittent hypoxia and atherogenesis.

A.3 Simplified model of endothelial NO synthesis

The kinetic model presented in the previous section is significantly complex and requires a considerable computational effort in order to be solved. A simplified model based on the Michaelis-Menten equation can be implemented instead. For the latter case, only the apparent activities of eNOS (instead of NO synthesis pathway) are modelled.

In cases where eNOS is fully active and the concentrations of substrates and co-enzymes are higher than those required, NO production can be expressed by the following equation:

$$R_{NO_{\mathrm{MAX}}} = \frac{d[NO]}{dt} = C_{eNOS} \cdot V_{c_{max}}, \tag{A-16}$$

where $R_{NO_{\mathrm{MAX}}}$ represents the maximum NO production rate, C_{eNOS} represents eNOS concentration and V_{cmax} represents the maximum catalytic rate, whose maximum reported value is 0.585 $\mu mol \cdot min^{-1} \cdot (mg\ of\ protein)^{-1}$ [81].

For a given eNOS concentration, NO production is regulated by the availability of

the substrates. Given that intracellular eNOS concentration under physiological conditions is significantly lower than the concentration of the substrates, the Michaelis-Menten equation can be used to model NO production rate. Thus

$$R_{NO} = \frac{C_{eNOS} \cdot V_{c_{max}} C_{substrate}}{K_m + C_{substrate}}, \tag{A-17}$$

where R_{NO} denotes NO production rate, $C_{substrate}$ represents the concentration of the substrate considered and K_m is the Michaelis constant for the such a substrate. Table A.2 shows experimental and theoretical values of K_m for each substrate (oxygen and L-arginine).

The NO production rate calculated using this simplified model is consistent with the results obtained using the kinetic model, as shown in [23]. Therefore, NO production rate in this thesis is modelled using the Michaelis-Menten approximation.

$K_m(\mu M)$	**Substrate**	**Reference**
11.0-11.5	Oxygen	Theoretical [23]
7.7	Oxygen	Experimental [115]
0.5	L-arginine	Theoretical [23]
0.9-2.9	L-arginine	Experimental [50, 154]

Table A.2: Michealis constants K_m involved in endothelial nitric oxide synthesis

Appendix B

Convective Transport of Vascular Nitric Oxide

The effect of convection on vascular transport of NO remains unclear. This appendix analyses NO convective transport within the rabbit aorta using the blood flow field computed in Chapter 4 for the case Re = 300 (corresponding to the average aortic root velocity within the cardiac cycle). It is found that the effect of convection on NO concentration depends significantly on the NO consumption rate by haemoglobin (k_{Hb}). Further, for the particular case considered, it is concluded that NO convective transport is negligible provided that $k_{Hb} >> 10s^{-1}$.

B.1 NO convective transport

B.1.1 Overview

Vascular NO is produced by endothelial cells in a WSS-dependent fashion. NO produced in the endothelium rapidly diffuses into both the lumen of the vessel and the subjacent arterial wall. In the arterial wall, NO activates a complex signalling

pathway that leads to vasodilation. In the lumen, NO is avidly scavenged by the haemoglobin contained in the red blood cells.

B.1.2 NO convective field

Vascular NO diffusing into the lumen is convected downstream by the flow of blood. The convective field is modelled under the following assumptions:

- **The radial convective transport due to the water transmural flux into the arterial wall is neglected**. A Peclet number in the radial direction Pe_r can be defined as

$$\mathrm{Pe}_r = \frac{V_r H}{D_{NO}},$$

where V_r is the radial water transmural velocity into the arterial wall, H is the height of the NO concentration boundary layer and (as in Chapter 3) D_{NO} is the NO diffusion coefficient. Lever *et al.* [141] measured V_r to be of the order of $\sim 10^{-6} cm s^{-1}$; D has been estimated to be of the order of $\sim 10^{-5} cm^2 s^{-1}$ [90], and H is shown in Chapter 5 to be of the order of $\sim 10^{-4} cm$. Thus,

$$\mathrm{Pe}_r \sim 10^{-5} << 1;$$

and hence NO diffusive transport outweighs NO convection in the radial direction.

- **Coutte flow is assumed within the NO concentration boundary layer.** This assumption is valid as long as the NO concentration boundary layer is contained well within the momentum boundary layer. The relative height of the momentum boundary layer H_M to the height of the NO concentration boundary layer H is given by the Schmidt number, defined as

$$Sc = \frac{\nu}{D_{NO}},$$

where ν is the dynamic blood flow viscosity. Considering a value of $\nu = 3.872$ x 10^{-2} $\mathrm{cm}^2\mathrm{s}^{-1}$ (based on the values for blood kinematic viscosity and density

used in Chapter 4), and the standard value for D_{NO} (D_{NO}=3.3 x 10^{-5} cm^2s^{-1} [90]) one obtains

$$Sc \sim 10^3 >> 1.$$

Therefore $H_M >>$ H, and hence Coutte flow can be assumed within the NO concentration boundary layer.

In line with the previous assumptions, the blood velocity **v** within the NO concentration boundary layer can be expressed as:

$$\mathbf{v} = \mathbf{v_s} = \gamma_L \, \eta \, \mathbf{s},$$

where γ_L is the wall shear rate, η is a coordinate in the direction normal to the arterial wall and **s** is a unit vector tangent to the velocity direction parallel to the arterial wall. Figure B.1 illustrates how the NO convective field is modelled within the NO concentration boundary layer.

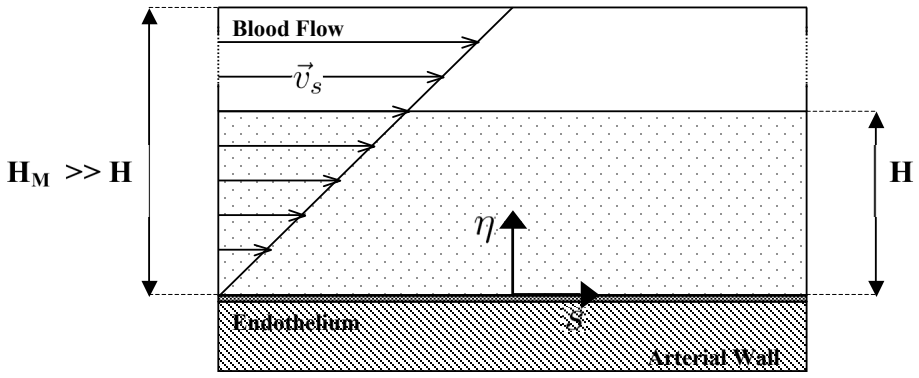


Figure B.1: Diagram illustrating how the NO convective field is modelled within the NO concentration boundary layer. The NO concentration boundary layer (characterised by its height H) is contained well within the momentum boundary layer (characterised by its height H_M). Thus, Couette flow can be assumed within the NO concentration boundary layer.

B.2 Vascular NO transport

Vascular transport of NO in the vessel lumen can be modelled using the steady Advection-Diffusion-Reaction equation

$$\mathbf{v} \cdot \vec{\nabla} C_{NO} - D_{NO} \nabla^2 C_{NO} + k_{Hb} C_{NO} = 0; \tag{B-1}$$

where (following the nomenclature of Chapter 3) C_{NO} represents NO concentration and k_{Hb} denotes the NO reaction rate with haemoglobin contained in blood. The order of magnitude of the different terms of Eq. B-1 is estimated next, along with values of the non-dimensional numbers that characterise NO transport.

Convective transport

Since the convective field is modelled as $\mathbf{v} = \mathbf{v_s} = \gamma_L \, \eta \, \mathbf{s}$, the convective term can be expressed as

$$\mathbf{v} \cdot \vec{\nabla} C_{NO} = v_s \frac{\partial C_{NO}}{\partial s} = \gamma_L \, \eta \, \frac{\partial C_{NO}}{\partial s},$$

where s is a coordinate in the **s** direction. Thus

$$\mathbf{v} \cdot \vec{\nabla} C_{NO} \sim \gamma_L H \frac{C_n}{L_s},$$

where L_s is a characteristic length in the **s** direction, and C_n is a characteristic NO concentration.

Diffusive transport

An NO concentration boundary layer is known to develop attached to the luminal side of the endothelium. Therefore, variations in NO concentration in the radial direction η are significantly greater than variations in the axial direction **s** ($i.e. \frac{\partial^2 C_{NO}}{\partial \eta^2} >> \frac{\partial^2 C_{NO}}{\partial s^2}$). Thus, the order of magnitude of the diffusive term in Eq. B-1 can be estimated as

$$D_{NO} \nabla^2 C_{NO} \sim D_{NO} \frac{\partial^2 C_{NO}}{\partial \eta^2} \sim D_{NO} \frac{C_n}{H^2}.$$

Reaction

The order of magnitude of the reactive term in Eq. B-1 can be directly estimated as

$$k_{Hb} C_{NO} \sim k_{Hb} C_n;$$

Non-dimensional numbers

Vascular NO transport is characterised by two non-dimensional numbers: a Peclet number defined as

$$Pe = \frac{\gamma_L H^3}{D_{NO} L_s}, \tag{B-2}$$

which represents the ratio between convective and diffusive transport, and a Damköhler number Da defined as

$$Da = \frac{k_{Hb} H^2}{D_{NO}}.$$

which gives the ratio between reactive and diffusive transport.

B.3 Effect of convective transport on vascular NO concentration

This appendix analyses the relative effect of convection (compared with NO diffusion and NO consumption) on vascular NO distribution. It is assumed *a priori* that NO convective transport is negligible and hence that NO reaction limits the height of the NO concentration boundary layer, that is

$$Da \sim 1,$$

and

$$Pe << 1.$$

This section investigates for which values of the parameter k_{Hb} the previous hypothesis is true. It has been assumed that

$$Da = \frac{k_{Hb} H^2}{D_{NO}} \sim 1.$$

Therefore the height of the NO concentration boundary layer H can be estimated as

$$H \sim \sqrt{\frac{D_{NO}}{k_{Hb}}}. \tag{B-3}$$

By substituting Eq. B-3 in Eq. B-2 one obtains

$$Pe = \frac{\gamma_L}{L_s}\sqrt{\frac{D_{NO}}{k_{Hb}^3}}.$$

In order for convective transport to be negligible, Pe needs to satisfy $Pe << 1$. Therefore

$$\frac{\gamma_L}{L_s}\sqrt{\frac{D_{NO}}{k_{Hb}^3}} << 1. \tag{B-4}$$

Eq. B-4 puts a restriction on the parameter k_{Hb}^3 such that

$$k_{Hb} >> \sqrt[3]{\frac{\gamma_L^2 D_{NO}}{L_s^2}}. \tag{B-5}$$

The order of magnitude of the right term (that depends on the wall shear rate γ_L, the NO diffusion coefficient D_{NO}, and the characteristic length L_s) is estimated next.

- **Wall shear rate γ_L**

  The wall shear rate can be calculated from the blood flow field computed in Chapter 4. Fig. B.2 show the computed shear rate for Re = 300 (see section 4.3 for further details).

  It is found that over 98% of the endothelium surface is exposed to a wall shear rate γ_L over the range [0 - 700] s^{-1}. Note that γ_L in certain regions of the vasculature (e.g. flow dividers) exceeds the upper bound of this range, and hence the following discussion may not be applicable. We will assume that the wall shear rate γ_L is characterised by the maximum wall shear rate $\gamma_{L_{max}}$ within the former range (i.e. $\gamma_{L_{max}} = 700\ s^{-1}$). Thus

  $$\gamma_L \leq \gamma_{L_{max}} \sim 700 s^{-1}. \tag{B-6}$$

- **NO diffusion coefficient D_{NO}**

  A fixed value of D_{NO} = 3.3 x 10^{-5} $cm^2 s^{-1}$ [90] is considered.

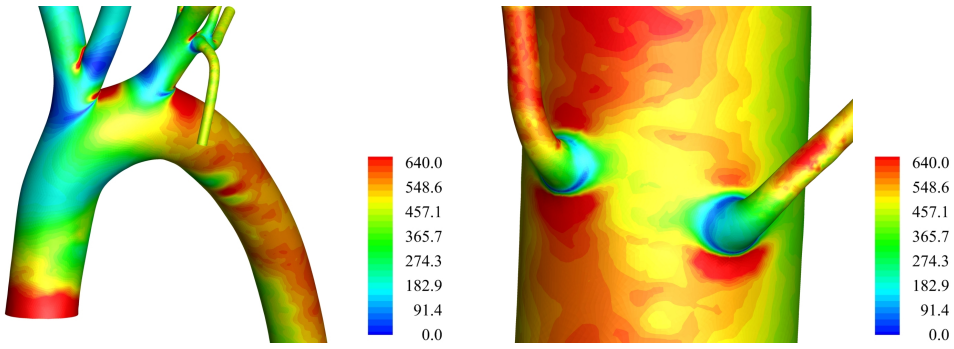
- **Axial characteristic length L_s**

  We will assume that L_s (which is a characteristic length scale of variation

in the concentration field) is of the same order of magnitude as the length scale of spatial variation in the WSS pattern. This is reasonable since the NO production rate depends on WSS.

Figure B.2 shows the wall shear rate distribution for the case studied. It is found that for most of the computational domain L_s is of the order of magnitude of the aortic root diameter. However, within certain vascular regions (such as the aortic arch and the vicinity of the intercostal arteries), significant variations in WSS distribution occur over shorter distances. Based on Fig. B.2 the minimum characteristic length $L_{s_{min}}$ is estimated to be $L_{s_{min}} = 2\mathrm{D}_{int}$ where D_{int} is the intercostal arteries diameter ($\mathrm{D}_{int} = 0.06cm$). Therefore

$$L_s \geq L_{s_{min}} \sim 2D_{int} \sim 10^{-1}cm. \tag{B-7}$$



(a) (b)

Figure B.2: Colour maps of wall shear rate(s^{-1}) at the aortic arch viewed ventral-dorsal (a) and the third pair of intercostal arteries viewed dorsal-ventral (b), for a inlet velocity corresponding to Re=300.

By substituting the parameter values discussed above (Eqs. B-7 - B-6) into Eq. B-8 one obtains

$$k_{Hb} >> \sqrt[3]{\frac{\gamma_{L_{max}}^2 D_{NO}}{L_{s_{min}}^2}} >> 10s^{-1}. \tag{B-8}$$

Therefore it is concluded that the effect of convection on vascular NO concentration is negligible provided that the NO reaction rate with haemoglobin k_{Hb} is much

greater than 10 s^{-1}.

B.3.1 NO convective transport when a constant NO production rate is considered

This section investigates the effect of convection on vascular NO transport for cases where the endothelial NO production rate is assumed to be constant. Although such cases are not physiologically realistic, they are shown in Chapter 5 (section 5.3.1.1) to be conceptually relevant.

The distribution of endothelial NO concentration reflects spatial variations in NO production rate. Therefore when a constant NO production rate is considered, there are not significant variations in NO concentration within the computational domain. Therefore, L_s (the characteristic length scale of variation in the concentration field) is such that $L_s \rightarrow \infty$. Thus Eq. B-4 is satisfied for any finite value of γ_L and D_{NO} provided that $k_{Hb} \neq 0$. Hence it is concluded that NO convective transport can be neglected for cases where a constant NO production rate is considered.

Publications

The work in this thesis has been published in a number of journal articles and conference proceedings and presented in several seminars, as detailed next.

Journal Articles

Endothelial Nitric Oxide Production and Transport in Flow Chambers: the Importance of Convection.
A. M. Plata, S. J. Sherwin, R. Krams.
Ann Biomed Eng, 38(9):2805-2816, 2010.

Blood Flow in the Rabbit Aortic Arch and Descending Thoracic Aorta.
P. E. Vincent, A. M. Plata, A. A. E. Hunt, P. D. Weinberg, S. J. Sherwin
Journal of the Royal Society Interface, Submitted for publication

Effect of reverse flow on the pattern of wall shear stress near arterial branches.
A. Kazakidi, A.M. Plata, S.J. Sherwin, P.D. Weinberg
Journal of the Royal Society Interface, Submitted for publication

Conference Contributions

The presenting author is denoted by an asterisk.

Computational Modelling of Blood Flow in a Realistic Representation of the Rabbit Aorta

A. Plata García*, P. Vincent, A. Hunt, S. Sherwin, P. Weinberg.

Oral presentation. 6th World Congress on Biomechanics, 1-6 August 2010, Singapore, Singapore.

Why You Should Care About The Reynolds Number

A. Plata García*, P. Vincent, A. Hunt, S. Sherwin, P. Weinberg.

Poster presentation. Imperial College Graduate School of Engineering and Physical Sciences (GSEPS) Research Symposium, 13th July, London, UK.

Blood Flow Features In A Realistic Representation Of The Rabbit Aorta

A. Plata García*, P. Vincent, A. Hunt, S. Sherwin, P. Weinberg.

Poster presentation. Cardiovascular Technology Symposium, 8 July 2010, London, UK.

Blood Flow and Vascular Nitric Oxide Transport in the Rabbit Aorta

A. Plata García*, P. Vincent, A. Hunt, S. Sherwin, P. Weinberg.

Oral presentation. Europa High Performance Computing Transnational Access Meeting, 15-17 June 2010, Helsinki, Finland.

A Computational Study of Blood Flow In a Realistic Representation of the Rabbit Aorta

A. Plata García*, P. Vincent, A. Hunt, S. Sherwin, P. Weinberg.

Oral presentation. Bioengineering 2009, 24-25 September 2009. Oxford, UK.

Shear Stress-dependent Nitric Oxide Production and Transport in Flow Chambers

A. Plata García*, N. Foin, S. Sherwin, R. Krams.

Oral presentation. Bioengineering 2009, 24-25 September 2009. Oxford, UK.

Shear stress and nitric oxide transport affect nuclear factor kB dynamics in endothelial cells

N. Foin*, Q. Qi, A. Plata García, S. Cuhlmann, P. C. Evans, C. G. Caro and R. Krams.

Oral presentation. European Meeting on Vascular Biology in Medicine, September 2009, Marseille, France.

Endothelial Nitric Oxide Production and Transport in Flow Chambers

A. Plata García*, S. Sherwin, R. Krams.

Oral Presentation. XXII Congress of the International Society of Biomechanics, 5-9 July 2009. Cape Town, South Africa.

Flow Features In a Realistic Representation of the Rabbit Aorta

A. Plata García*, P. Vincent, A. Hunt, S. Sherwin, P. Weinberg.

Oral presentation. XII International Symposium on Computer Simulation in Biomechanics, 2-4 July 2009. Cape Town, South Africa.

Shear stress and nitric oxide transport affect nuclear factor kB dynamics in endothelial cells

N. Foin*, A. Plata García, S. Cuhlmann, P. C. Evans, C. G. Caro and R. Krams.

Poster presentation. Arteriosclerosis, Thrombosis, and Vascular Biology Meeting 2009. Washington DC, USA.

Computational Model of Nitric Oxide Transport in Flow Chambers

A. Plata García*, N. Foin, S. Sherwin, R. Krams.

Poster Presentation, 4th International symposium on Biomechanics in Cardiovascular Disease, 16-17 April 2009. Rotterdam, The Netherlands.

Shear stress and nitric oxide transport affect nuclear factor kB dynamics in endothelial cells

N. Foin*, Q. Qi, A. Plata García, S. Cuhlmann, P. C. Evans, C. G. Caro and R. Krams.

Oral presentation. 4th International symposium on Biomechanics in Cardiovascular Disease, 16-17 April 2009. Rotterdam, The Netherlands.

Shear stress and nitric oxide transport affect NF-kB dynamics in endothelial cells

N. Foin*, A. Plata García, S. Cuhlmann, P. C. Evans, C. G. Caro and R. Krams.

Poster presentation. Cardiovascular Technology Network $3^r d$ symposium, 12 December 2008, Imperial College London. London, UK.

Endothelial Nitric Oxide Production and Transport in Flow Chambers

A. Plata García*, S. Sherwin, R. Krams.

Poster Presentation, Bioengineering 2008, 18-19 September 2008. London, UK.

Computational Model of Nitric Oxide Transport and Production in Flow Chambers

A. Plata García*, S. Sherwin, R. Krams.

Oral Presentation, UK Focus for Biomedical Engineering Futures Meeting Study and Treatment of Cardiovascular Disease: Devices and Fluidics, 15-17 September 2008. London, UK.

Seminars

Computational Study of Vascular Nitric Oxide Production and Transport

May 2010. Department of Bioengineering. Imperial College London, London, UK.

Shear Stress in a Realistic Representation of the Rabbit aorta

March 2010. Vall d'Hebron Hospital, Barcelona, Spain.

Flow Features in a Highly Realistic Representation of the Rabbit Aorta and its Branches

October 2009. Department of Maths. Imperial College London, London, UK.

Blood Flow Features in a Realistic Representation of the Rabbit Aorta

October 2009. Department of Aeronautics. Polytechnic University of Madrid (UPM). Madrid, Spain.

Estudio Computacional del Flujo Sanguneo en la Aorta del Conejo

October 2009. Laboratory of Computational Methods and Numerical Analysis. Polytechnic University of Catalunya (UPC). Barcelona, Spain.

Computational Study of Blood Flow in a Realistic Representation of the Rabbit Aorta

October 2009. Department of Mechanical Engineering. Polytechnic University of Catalunya (UPC). Barcelona, Spain.

Blood Flow in the Rabbit Aorta and Implications for Atherogenesis

September 2009. Department of Mechanical Engineering. University of Extremadura (UEx). Badajoz, Spain.

Nitric Oxide Production and Tranport in Flow Chambers

February 2009. Department of Bioengineering. Imperial College London. London, UK.

Computational Model of Nitric Oxide Transport and Production in Flow Chambers

November 2008. Department of Aeronautics. Imperial College London. London, UK.

Simulation of Nitric Oxide transport within the vascular system

February 2008. Department of Bioengineering. Imperial College London. London, UK.